# Breach growth in cohesive embankments due to overtopping

Zhao, Gensheng

**DOI**
10.4233/uuid:ee435ef7-f71c-493c-812b-68cf1e39aa33

**Publication date**
2016

**Document Version**
Final published version

**Citation (APA)**
Zhao, G. (2016). *Breach growth in cohesive embankments due to overtopping*. [Dissertation (TU Delft), Delft University of Technology]. https://doi.org/10.4233/uuid:ee435ef7-f71c-493c-812b-68cf1e39aa33

# Breach Growth in Cohesive Embankments due to Overtopping

# Breach Growth in Cohesive Embankments due to Overtopping

**Proefschrift**

ter verkrijging van de graad van doctor
aan de Technische Universiteit Delft,
op gezag van de Rector Magnificus prof.ir. K.C.A.M. Luyben;
voorzitter van het College voor Promoties,
in het openbaar te verdedigen

door

Gensheng ZHAO
Master of Science in Hydraulic Engineering, Changjiang River Scientific Research Institute, China
geboren te Shandong, China

Dit proefschrift is goedgekeurd door de promotor:
Prof. drs. ir. J.K. Vrijling

Copromotor:
Dr. ir. P.J. Visser

Samenstelling promotiecommissie:

| | |
|---|---|
| Rector Magnificus | Voorzitter |
| Prof. drs. ir. J.K. Vrijling | Technische Universiteit Delft, promotor |
| Dr. ir. P.J. Visser | Technische Universiteit Delft, copromotor |

Onafhankelijke leden:

| | |
|---|---|
| Prof. dr. Y. Li | Nanjing Hydraulics Research Institute, China |
| Prof. dr. F. Mostaert | Flanders Hydraulics Research, Belgium |
| Prof. dr. ir. S. N. Jonkman | Technische Universiteit Delft |
| Prof. dr. ir. W. S. J. Uijttewaal | Technische Universiteit Delft |
| Dr. ir. M van Damme | Technische Universiteit Delft |
| Prof. dr. ir. M. Kok | Technische Universiteit Delft, reservelid |

Front cover: Photo of Breaching Experiment in the present study
Back cover: Innovation Painting by C. (Jan) Zhao

ISBN: 97890-6562-3935 (print)
ISBN: 97890-6562-3942 (online)



Author email: genshengzhao@hotmail.com

Printed by Delft Academic Press / VSSD uitgeverij, the Netherlands

# Summary

Breaching is the most frequent form of embankment failure in the world. Due to overtopping, an embankment starts to breach when part of the embankment actually breaks away, leaving an opening for water to flood the land protected by the embankment. A breach can be a sudden or gradual failure that is caused by surface erosion and/or headcut erosion in the embankment. The magnitude and extent of the losses depend highly on the rate of breaching of the embankment, which determines the discharge through the breach and the speed and rate of inundation of the valley or polder. Therefore, modelling of the breach evolution in embankments is of significant interest for damage assessment and risk analysis. It is also important for the development of early warning systems for dike and dam failures and of evacuation plans for people at risk.

Mathematical breach models have been developed mainly based on empirical methods, physically-based methods and semi-physically-based methods. Empirical models have been developed with probabilistic methods and/or based on case studies. These models can only be applied to similar cases. Semi-physically-based models involve not only empirical data but also include physical processes of breaching. Physically-based models are entirely developed according to the real physical processes of breaching. Generally, empirical models are simple but have a low reliability. Physically-based models are very complex, but predictions are more reliable. In order to develop a physically-based model, the physical processes of breaching require to be exposed. Therefore large-scale experiments are urgently needed to improve and push the breach model development further. Large-scale physical model tests were undertaken in the present study, aimed to increase the understanding of the physical processes, and to provide reliable data for the calibration and validation of breach models.

The breach flow plays an important role in the embankment breaching process, coupling the hydraulic process and the sediment transport process. During the breaching process,

the flow overtops the entire embankment crest and generates the breach channel in the initial phase of the breach development. As the breach further develops, the breach flow goes only through the breach channel due to the decrease of the upstream water level. The breach flow can thus be classified as compound weir flow and weir flow, each having own special characteristics. In a breach, the helicoidal flow accelerates the sediment undermining at the toe of the breach slopes and widens the breach in the lateral direction of the embankment. A triangular hydraulic jump happens when the breach flow changes from supercritical flow into subcritical flow, with a triangular critical area at the toe of the breach. The triangular hydraulic jump works as a driving force to the headcut erosion in the breaching process and the scour hole development at the toe of embankment. According to the hydraulic energy loss in the breach, the discharge coefficients are deducted for both weir flow condition and compound weir flow condition. The resulting discharge coefficients can be used in the calculation of the breach discharge in a breach model.

Erosion is the result of the interaction between breach flow and embankment material. Surface erosion starts in the initial phase of the breaching process and triggers the initial damage of the embankment. As the surface erosion develops completely, the headcut erosion leads the breaching process by cutting the embankment slope and finally deepening the crest level. The breach side slopes are undermined by lateral erosion and the breach widens in lateral direction due to lateral collapses.

In the present study, five runs of breach experiments were conducted in a relative large laboratory flume. The experimental results clearly expose the hydrodynamic process and the erosion process in the breaching of the cohesive embankment. The breaching starts with the initial erosion of the embankment surface washing away the embankment surface. Due to the surface erosion at the toe of the embankment, the headcut erosion is stimulated on the embankment slope. While headcut migration stimulates the breach to develop in longitudinal direction, the lateral erosion triggers the breach to widen in lateral direction. Three types of erosion (surface erosion, headcut erosion and lateral erosion) contribute to the breach erosion process in the embankment, however, the breach flow is

the driving force for the erosion. Sediment deposition in the breaching process, generally ignored in the embankment breaching studies, is also of importance.

A mathematical model has been developed that couples weir flow and erosion (surface erosion, headcut erosion and lateral erosion). The breaching process is simplified into initial development, deepening development and widening development, corresponding with surface erosion, headcut erosion and lateral erosion, respectively. As the link between flow and embankment material, erosion plays a key role in the embankment breach model. Mathematical descriptions of the headcut migration and the lateral migration rate have been developed to simulate the breaching process in cohesive embankments. The headcut erosion and the lateral erosion are considered to occur in the form of clay blocks instead of in the form of individual clay particles.

The data of the large-scale breach experiments have been used to calibrate and validate the proposed breach model (headcut migration and lateral migration). The model has also been applied to simulate a laboratory test done in 2005 in the Laboratory for Fluid Mechanics of Delft University of Technology and to the breaching of the Tangjiashan Landslide Barrier (Wenchuan, China, 2008), a breaching event in prototype. It can be concluded that the agreements between the results calculated with the proposed breach model and the measured data are relatively good.

# Samenvatting

Titel: Bresgroei in dijken en dammen gemaakt van cohesieve grond door overstromend water

Bresvorming is de meest voorkomende vorm van het falen van dijken en dammen in de wereld. Door overstromend water, begint een dijk te bressen wanneer een deel van de dijk daadwerkelijk wegspoelt of afschuift, als gevolg waarvan een opening ontstaat waardoorheen water stroomt en het land achter de dijk overstroomt. Een bres in de dijk kan plotseling ontstaan of ook geleidelijk door oppervlakte-erosie en/of zogenaamde headcut-erosie van het dijklichaam. De omvang en de grootte van de teweeggebrachte verliezen zijn sterk afhankelijk van de mate van bresvorming, welke bepalend is voor het debiet door de bres en dus voor de snelheid waarmee en de mate waarin de polder of de vallei overstroomt. Het modelleren van de bresontwikkeling is daarom van groot belang voor de beoordeling van de mogelijke schade en de analyse van de risico's. Het is ook belangrijk voor de ontwikkeling van waarschuwingssystemen en evacuatieplannen voor de bewoners van het betreffende gebied.

Mathematische bresmodellen zijn vooral ontwikkeld met empirische methoden, fysische methoden en semi-fysische methoden. Empirische modellen zijn ontwikkeld met probabilistische methoden en/of op basis van 'case studies'. Deze modellen kunnen alleen worden gebruikt in vergelijkbare situaties. Semi-fysische modellen omvatten niet alleen empirische gegevens, maar ook fysische processen. Fysische modellen zijn ontwikkeld overeenkomstig de werkelijk in een bres optredende fysische processen. Empirische modellen zijn eenvoudig, maar over het algemeen hebben deze modellen een lage betrouwbaarheid. Fysische modellen zijn zeer complex, maar de voorspellingen zijn betrouwbaarder. Teneinde een fysisch model te kunnen ontwikkelen, moeten de fysische processen die bij bresgroei optreden, aan het licht worden gebracht. Grootschalige experimenten zijn derhalve van groot belang om de fysische modellen te kunnen verbeteren. Grootschalige modelproeven zijn in deze studie gedaan, om het inzicht in de

fysische processen te verbeteren, en om betrouwbare gegevens voor de kalibratie en validatie van bresgroeimodellen te verkrijgen.

De stroming door de bres speelt een belangrijke rol in het bresgroeiproces; deze stroming koppelt het hydraulische proces en het proces van sedimenttransport. Gedurende het bresgroeiproces wordt eerst de gehele dijk overstroomt als gevolg waarvan een initiële bres ontstaat in de dijk. Naarmate de bres zich verder ontwikkelt, zal door een daling van de bovenstroomse waterstand de stroming uitsluitend door de bres gaan. Dus de stroming door de bres kan worden aangemerkt als stroming over een samengestelde overlaat en als stroming over een overlaat, met kenmerkende eigenschappen voor beide types overlaat. In de bres doet de spiraalvormige stroming het oppikken van sediment aan de teen van de bres versnellen als gevolg waarvan de bresbreedte toeneemt. Een driehoekvormige watersprong treedt op wanneer de stroming door de bres verandert van superkritische stroming in subkritische stroming, een driehoekig gebied met kritische stroming vormend aan de teen van de bres. De driehoekvormige watersprong werkt als een aandrijvende kracht voor de headcut-erosie in het bresgroeiproces en de ontwikkeling van de ontgrondingskuil aan de teen van de dijk. Uitgaande ven het hydraulische energieverlies in de bres, worden de afvoercoëfficiënten afgeleid, voor zowel de conditie van overlaat als samengestelde overlaat. De resulterende afvoercoëfficiënten zijn zeer bruikbaar voor de berekening van de stroming door de bres.

Erosie is het gevolg van de wisselwerking tussen stroming door de bres en het dijkmateriaal. Oppervlakte-erosie begint in de eerste fase van de bresvorming en leidt tot een initiële bres in de dijk. Naarmate de oppervlakte-erosie zich verder ontwikkelt, neemt de headcut-erosie het bresgroeiproces over met het afsnijden van het binnentalud van de dijk en het uiteindelijke verdiepen van de kruin van de dijk. De zijhellingen van de bres worden door de laterale erosie ondermijnd en de bres verbreedt zich in zijwaartse richting, met name door de laterale instortingen.

In deze studie werden vijf bresgroeiproeven uitgevoerd in een relatief grote stroomgoot. De experimentele resultaten onthullen duidelijk het hydrodynamische proces en het

erosieproces in het proces van bresgroei in dijken opgebouwd van cohesief materiaal. Het bresgroeiproces begint met de initiële erosie van het oppervlakte van de dijk. Als gevolg van de oppervlakte-erosie aan de teen van het binnentalud, wordt de headcut-erosie van het binnentalud gestart. Terwijl de headcut-erosie de bres in de stromingsrichting doet groeien, leidt de laterale erosie tot een verbreding van de bres in zijwaartse richting. Drie types van erosie (oppervlakte-erosie, headcut-erosie en laterale erosie) dragen dus bij aan het proces van bresvorming in de dijk. Echter de stroming door de bres is de drijvende kracht voor het erosieproces. Sedimentatie is ook van belang in het bresgroeiproces; deze wordt over het algemeen genegeerd in bresgroeistudies.

Een mathematisch model is ontwikkeld dat de stroming over de overlaat koppelt aan de erosie (oppervlakte-erosie, headcut-erosie en laterale erosie). Het bresgroeiproces wordt geschematiseerd tot initiële bresgroei, verdieping van de bres en verbreding van de bres, overeenkomend met respectievelijk oppervlakte-erosie, headcut-erosie en laterale erosie. Mathematische beschrijvingen voor de headcut-ontwikkeling en de laterale groei zijn ontwikkeld om het bresgroeiproces in dijken en dammen opgebouwd met cohesief materiaal te simuleren. Hierin wordt de erosie van blokken cohesief materiaal beschouwd in plaats van de erosie van individuele kleideeltjes.

De data van de grootschalige bresgroeiproeven zijn gebruikt om het voorgestelde bresgroeimodel te kalibreren en te valideren. Het model is ook getoetst aan data van een proef in 2005 gedaan in het Laboratorium voor Vloeistofmechanica van de Technische Universiteit Delft en aan data van prototypemetingen van het bresgroeiproces in de Tangjiashan Landslide Barrier (Wenchuan, China, 2008). Er kan geconcludeerd worden dat met het voorgestelde bresgroeimodel een behoorlijk goede overeenkomst wordt gevonden met de gemeten resultaten.

# Contents

# Chapter 1 Introduction

## 1.1 Background

Embankments, including dikes and dams, are beneficial to people all over the world. The history of embankments is the epitome of the rise and fall of human civilization, especially in regard to the protection against floods and the irrigation of farmland. Dikes have been protecting human lives and properties from flood disasters, and dams, keeping large volumes of waters under control, have been used to prevent flooding, and have been useful in navigation, irrigation, water supply, hydro-electric power, recreation and so on. But, natural embankments are also causing risks, due to landslides induced by earthquakes, storms and other natural phenomena, and as a consequence, involve high risks to human lives and properties as a result of their failures due to overtopping, piping and other factors.

The magnitude and extent of the losses greatly depend on the rate of breaching of embankments, which determines the discharge through the breach and the speed and the rate of inundation of the valley or the polder. Therefore, modelling of breach evolution in embankments is of significant interest for damage assessment and risk analysis. It is also important for the development of early warning systems for dike and dam failures and for evacuation plans for people at risk.

## 1.2 The Struggle against Floods

Throughout history floods have been an ever threatening presence in the lives of people. People have been building structures in order to protect and to defend themselves against floods.

China has experienced thousands of flood disasters throughout its history. It has experienced 6 of the world's top 10 deadliest floods and landslides of all times and the

top 5 all occurred in China (Asian Disaster Reduction Canter, 2009). The estimated deaths of the floods in 1931 range from 2 to 4 million, and are listed as the deadliest natural disasters. The 1887 Yellow River flood ranks second in death toll in flood disasters, claiming lives from 0.9 million to 2 million. The 1938 Yellow River (Huang He) flood ranks third, with deaths from 0.5 million to 0.7 million. Overall, flooding is the worst natural disaster in China.

After the 1998 flood in the Yangtze River basin, people rebuilt the dikes along the river. The Three Gorges Dam construction started in 1994 after a period of arguments and discussion of more than half a century and was completed in 2006. Its main function is flood control to protect the people downstream from it against serious floods in the Yangtze River basin.

Like China, the Netherlands, with approximately 60% of the land prone to flooding, is a country whose history is influenced by floods and the fight against floods (Van de Ven, 1993; Visser, 1998). The 1953 flood in the provinces of Zealand and South Holland led to the largest natural disaster in the recent history of the Netherlands. It damaged 800 km of dikes with about 900 dike breaches, and inundating 2,000 $km^2$ of land. 1835 people lost their lives in the 1953 flood. The economic loss accounted for approximately 14% of the GDP of the Netherlands.

To prevent future floods, the Dutch constructed the world famous Delta Works, with the aim of damming off the estuaries and shortening the coastline in the southwest of the Netherlands.

## 1.3 Types of Embankments

Embankments vary in nature and function. A classification of embankments is shown in Table 1.1. Designed to control or prevent flooding, a flood control embankment is one out of several types of embankments on the floodplains. An embankment, built to prevent flooding of low-lying land, is also called a levee or dike constructed along a riverbank

and at some distance from the river to retain floodwater. It may or may not have an impervious core.

Embankment dams come in two types: the earth-fill dams made of compacted earth, and the rock-fill dams. Most embankments have a central section or core composed of impermeable material to stop water from seeping through the dam. The core can be of clay, concrete, or asphalt concrete. This type of dam is a good choice for sites with wide valleys. Since they exert little pressure on their foundations, they can be built on hard rock or on softer soils. For a rock-filled dam, rock-fill is blasted using explosives to break the rock. Additionally, the rock pieces may need to be crushed into smaller chunks to get the right range of size for use in an embankment dam.

The embankments mentioned above are man-made types; but there is also another type, namely a natural embankment, e.g., barriers caused when a valley is closed off by a landslide. High risk usually exists in this kind of embankment for its uncertain stability, due to the content of the landslide barriers, which can contain various unknown materials. Usually a landslide embankment breaches in the end, because the river water accumulates continuously behind it. Therefore this kind of embankment is very dangerous to human lives and properties.

## Table 1.1 Types of embankments

| Items | Valley Dam Embankment | Bundled Reservoir Embankment | Linear Flood Defences (Coastal and Fluvial) | Landslide Barrier |
|---|---|---|---|---|
| **Main types** | Earth-fill dam<br>Rock-fill dam | Earth-non-cohesive<br>Earth-cohesive<br>Earth-composite structures | Earth-non-cohesive<br>Earth-cohesive<br>Earth-composite structures<br>Typically poorly constructed from variety of materials | Rock<br>Earth<br>Composite structures |
| **Primary loads** | Water pressure<br>Self-weight<br>Wave action | Water pressure<br>Self-weight<br>Wave action (limited) | Exposed wave action (coastal)<br>Water pressure<br>Self-weight | Water pressure<br>Self-weight |
| **Water type** | Fresh | Fresh | Fresh/saline | Fresh |
| **Water volume** | Finite reservoir + storm volume | Finite reservoir | Finite storm (fluvial)<br>Infinite and periodic (coastal) | Finite storm (fluvial) |
| **Typical face protection** | Natural and synthetic (extensive) | Natural and synthetic (extensive) | Natural and synthetic (limited) | None |

## 1.4 Breaching in Embankments due to Overtopping

Failures of earthen embankment dams or dikes can generally be classified into three types: hydraulic failures, seepage failures and structural failures. These failures lead directly to breach initiation and may result in breach development. Hydraulic failures following from the uncontrolled flow of water over and adjacent to the embankment are due to the erosive action of water on the embankment slope and crest. Earthen embankments or dikes are not generally designed to be overtopped and therefore are particularly susceptible to erosion.

Seepage failure occurs through the earthen embankment or dike and/or through its foundation. Seepage, if uncontrolled, can erode fine soil material from the downstream slope or from the foundation and continue to move towards the upstream slope to form a pipe or a cavity, which can lead to a complete failure of the embankment. These embankment breaches are often accompanied by embankment boils, or by sand boils. A sand boil occurs when the upward pressure of water flowing through soil pores under the embankment exceeds the downward pressure from the weight of the soil above it. The under-seepage resurfaces, on the landside, in the form of a volcano-like cone of sand. Boils signal a condition of incipient instability which may lead to erosion of the embankment toe or foundation, or result in a sinking of the embankment into the liquefied foundation below. Overtopping and complete breaching of the embankment may quickly follow.

Structural failure of an earthen embankment may take the form of a slide or displacement of material in either the downstream or the upstream face. Sloughs, bulges, cracks or other irregularities in the embankment or dike are generally signs of serious instability and may indicate structural failure as well as overtopping of the embankment.

Earthen embankments can fail when water overtops the crest of the embankment. Embankment overtopping can be caused when flood levels exceed the lowest crest level of the embankment system, or if high winds begin to generate significant waves in the

ocean or river water to bring waves crashing over the embankment. An overtopping embankment breach is when part of the embankment actually breaks away, leaving a large opening for water to flood the land protected by the embankment. A breach can be a sudden or a gradual failure that is caused either by surface erosion or by a subsurface failure of the embankment. Overtopping can lead to significant landside erosion of the embankment or, it can even be the mechanism for complete breaching.

Overtopping of embankment dams can occur due to an inadequate spillway capacity to pass flood. This is one of the most common causes of embankment dam failures and this has nothing to do with the geology of the dam site. Earthen embankment dams will fail if the spillway is too small and flood waters raise high enough to flow over the top of the dam wall. The estimation of the size of a maximum flood and the chance of a dam to endure such an event is a science which has undergone continuing evolution over the last century. As a result many dams that were built decades ago may now be considered as inadequate spillways, even though the spillways were designed to standards of safety, which were considered as adequate at the time of construction of the dam.

In this thesis, the overtopping is supposed to be caused by hydraulic failures, seepage failures, structure failure as well as an inadequate spillway capacity. It is assumed that the overtopping triggers the breaching process in the cohesive embankment.

## 1.5 Objectives and Methodology

A key aspect of flood management is protection against floods. Most important is the aspect to understand how hydraulic structures operate under conditions of normal loads and under conditions of extreme floods. Additionally, the prediction of the failure conditions and the failure process is an important part of flood management.

The embankment breach is studied since the end of 19$^{th}$ century (Wahl, 2007), however, the precise process and mechanism are not yet fully and clearly interpreted, especially regarding breaching in the cohesive and/or composite embankments. Visser (1998) and Zhu (2006) studied the homogenous sandy dike breach growth and the clayey dike breach

growth, respectively; both of them assumed 5 stages in the dike breach growth process. Visser (1998) and Zhu (2006) stated that it is necessary to predict and interpret the breach variables based on physical models, field measurements in situ and case studies of prototype embankment failures.

The main research objective in this thesis is to investigate the mechanism of breach growth in cohesive embankments due to overtopping, and to model the process of breach growth in cohesive embankments following methodologies of hydraulics, soil mechanics, sediment erosion and transportation. The proposed breach growth model can be classified into an initial erosion model, a headcut erosion model and a lateral erosion model as well as a flow model. The erosion models and the flow model are coupled into the breach growth model for cohesive embankments. The model developed in this thesis will be calibrated and validated with laboratory and field data.

## 1.6 Thesis Outline

Chapter 2 discusses the state-of-the-art of embankment breach modelling. Firstly, the causes of embankment breaching are reviewed and analysed with several case studies. Secondly, the breaching process for the cohesive embankment is discussed. Various models, including an empirical model, a mathematical model and a physical model, are reviewed and analysed. In the end, a review is made of the field measurement analyses for the Tangjiashan Landslide in China. In Chapter 3, the research discusses the hydraulic characteristics of breach flow. In order to study the principles of breach flow, a series of experiments were conducted in the Laboratory for Fluid Mechanics in Delft University of Technology. The main aim is to study the breach flow characteristics and the discharge coefficient in the breach channel. Chapter 4 discusses the incipient development of undisturbed clay and proposes a new erosion model for undisturbed clay in a combination of hydraulic and geo-technique approaches. Based on headcut erosion and lateral erosion in the breaching process, two mathematical models (headcut migration and lateral migration) are proposed and validated. In Chapter 5, five large-scale experiments of cohesive embankments are described that were designed to be conducted in a large laboratory flume. Based on Chapter 3, Chapter 4 and Chapter 5, the breaching process in

cohesive embankments is described in Chapter 6, and a mathematical model is developed including headcut erosion and lateral erosion (Fig. 1.1). The breaching process starts at the initial trench erosion, and headcut erosion happens when the initial erosion fully develops. Lateral erosion triggers the breach to become wider and wider. The scour hole develops in the downstream of the embankment. From the upper part to the bottom part in the flowchart (Fig. 1.1), the study of breach growth in cohesive embankments can be explicated. In Chapter 7, the calibration and validation is done with the available data of laboratory experiments. The developed model is applied to laboratory tests and a prototype case, e.g., the Tangjiashan Landslide in China. In the end, the conclusions and recommendations are given in Chapter 8.

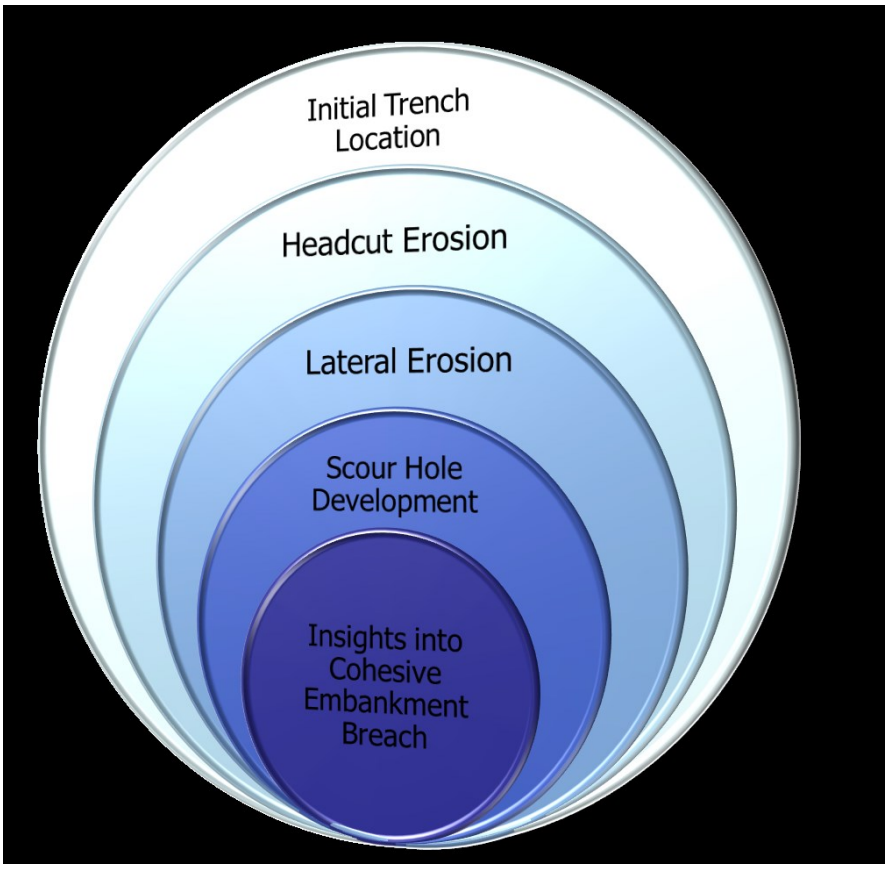


**Figure 1.1 Sketch of breach growth in the thesis**

# Chapter 2 State of the Art of Embankment Breach Modelling

## 2.1 Introduction

Embankment breaches occur all over the world and lead to flooding of inhabited areas, requiring flood risk analysis and flood management. Embankment breaching is a complex process with an uncertain initiation and development process. In the mechanics of the breaching process, theories of hydraulics, soil mechanics, sediment erosion and transportation are combined. In detail, the breaching process study includes breach initiation, breach hydraulics, breach formation, and breach morphology. There are many research methods involved as well, including empirical models (dimensional analytical solution and dimensionless analytical solution), mathematical models, physical models, and field measurement analysis. This chapter gives a state-of-the-art review of the embankment breach research.

An embankment breach can be natural or man-made. Embankments may breach as a result of overtopping, piping, wave action, and extraordinary natural events such as extreme rainfalls and earthquakes, etc. Man-made causes include the removal of embankments, a faulty design, a landslide barrier dredging, or even wilful destruction.

Surface erosion of an embankment is usually caused by the action of wind and water (waves but also normal flow). Erosion can be worsened by pre-existing or new damage to a levee. Areas without surface protection are more prone to erosion. Usually embankments fail when water overtops the crest. Embankment overtopping can be caused when flood waters simply exceed the lowest crest of the levee system or if high winds begin to generate significant waves (a storm surge) in the ocean or river water crashing over the embankment. Overtopping can result in significant landside erosion of the embankment and then triggers embankment breaching.

## 2.2 Mechanics of Breaching Process

### 2.2.1 Breach Variables

In order to physically describe the complex breaching process, the breach variables, breach depth, breach width, and side slopes should be defined (Fig. 2.1), as well as the time variable associated with the time required for breach initiation and development. Fig. 2.1 (b) describes the surface erosion in the initial phase of the embankment breach. Fig. 2.1 (d) indicates the breach developments in longitudinal direction of the embankment. In this study, the longitudinal breach development is defined as the heacut migration, which starts at the landside slope toe and stops at the riverside slope toe (Fig. 2.1 (d)). Fig. 2.1 (e) explicates the lateral migration, which is triggered by the helicoidal flow in the breach channel.

Breach depth is the vertical extent of the breach, measured from the embankment crest down to the invert of the breach. Breach width is the length from one side of the breach to the other side laterally. The breach rate and the ultimate breach width could dramatically affect the peak discharge and the resulting inundation levels downstream from the embankment. The average breach widths at the top and at the bottom of the breach opening are very important to the research of the breaching process. The breach side slopes with the breach width and depth actually specify the shape of the breach opening. It is important to predict the breach width and depth with the side slope angles.

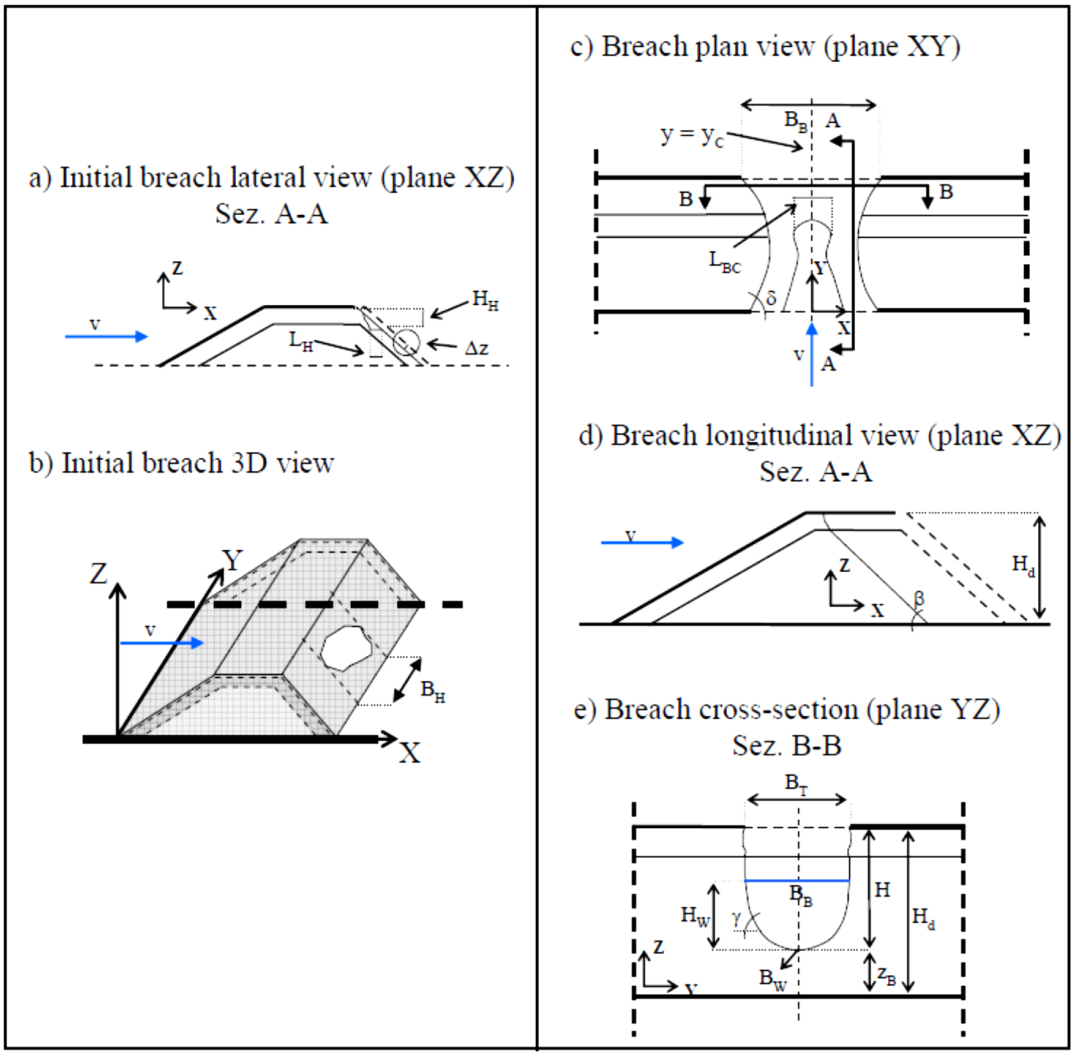


**Figure 2.1 Breach geometrical variables (Morris, 2009)**

### 2.2.2 Breach Initiation Time and Breach Formation Time

The time-related parameters are breach initiation time and breach formation time. Wahl (1998) defined the breach initiation time as the time that spans from the first flow over the embankment initiating warning, evacuation, or heightened awareness of embankment failure to the end, namely the time of the start of the breach formation.

There are many definitions of the breach formation time according to the different investigators. According to the model of DAMBRK (Fread, 1988), the beginning of the breach formation starts after the downstream face of the embankment has eroded away and the resulting crevasse has progressed back across the width of the dam to reach the

upstream face. It is important to recognize and account for the breach initiation time, because it directly affects the amount of advance warning time available for evacuating the populations downstream.

Prior research (case studies, empirical predications, numerical models, etc.) has mainly focused on the breach formation time, although several investigators have acknowledged the existence of the breach initiation time. The breach initiation time has, in most of the case studies, not been accepted as an independent parameter. What's more, breach initiation time is not considered in most of the available models (e.g. DAMBRK, Fread, 1988). However, several physically-based breach models simulated the breach initiation time as the embankment surface erosion time, which is not consistent with the erosion mechanics observed in laboratory tests and documented case studies.

### 2.2.3 Breach Development Process in Cohesive Embankments

Rolston (1987) proposed a good description of the mechanics of embankment erosion. For cohesive embankments, breaching takes place by headcut erosion. At the beginning, the headcut is typically formed at the toe of the embankment and then advances upstream, until the crest of the embankment is breached. In some cases a series of stair-step headcuts forms on the downstream face of the embankment. The action is similar to that described by Dodge (1988) for model testing of embankment overtopping. The relevant processes are headcut initiation and headcut advance triggered by geotechnical mass wasting.

Powledge *et al*. (1989) and Zhu *et al.* (2006) summarized ongoing research efforts of several research projects aimed at developing new methods for the protection of embankments from erosion during overtopping flow, and for the prediction of erosion of protected and unprotected embankments. Research in several small-scale facilities was considered to be qualitative, due to the difficulty of adequately reproducing the complex processes of erosion and sediment transport in steep, shallow flows at small scales; research in large-scale facilities was considered more quantitative. All the studies indicate

that embankment erosion is a multivariable, multidisciplinary problem. Random influences can be substantial, and thus, repetition of model tests is critical.

Fread (1987) developed a breach erosion model (BREACH) for an earthen dam to predict the breach size, shape, time of formation and the breach outflow hydrograph. He assumed that the initial breach has a rectangular shape and then changes to a trapezoidal-shaped channel when the sides of the breach channel collapse, forming an angle with the vertical, until the critical value has been reached (Fig. 2.2). In the model, erosion is assumed to occur equally along the bottom and along the sides of the breach channel, except, when the sides of the breach channel collapse and if the valley floor has been reached, further downwards erosion is not allowed and the peak discharge can be expected.

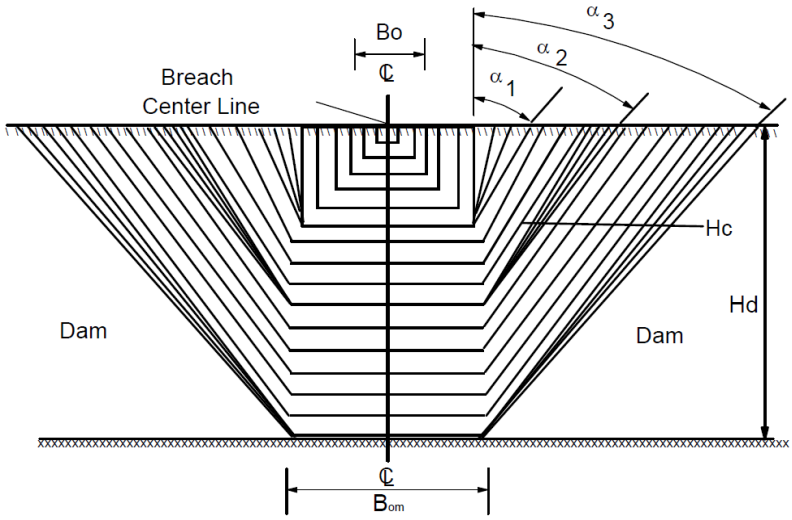


**Figure 2.2 Front view of dam with breach formation sequence (Fread, 1987)**

Singh *et al.* (1989) developed the BEED model for the simulation of gradual erosion of earth-fill dams. The model utilizes the mass conservation equation for the depletion of reservoir water, the broad-crested weir hydraulics for flow over and through the breach, the Einstein-Brown (1950) bed-load formula for breach erosion and the contour method for breach slope stability. The BEED model has been applied to hindcast several earth-fill dam failure events (Singh, 1996). Fig. 2.3 shows the breach evolution predicted for the South Fork Dam in Pennsylvania, United States. The calculated values for the peak

discharge and breach formation time were in good agreement with the observed values. However, notable discrepancies were seen between those of the breach top width (Zhu, 2006).

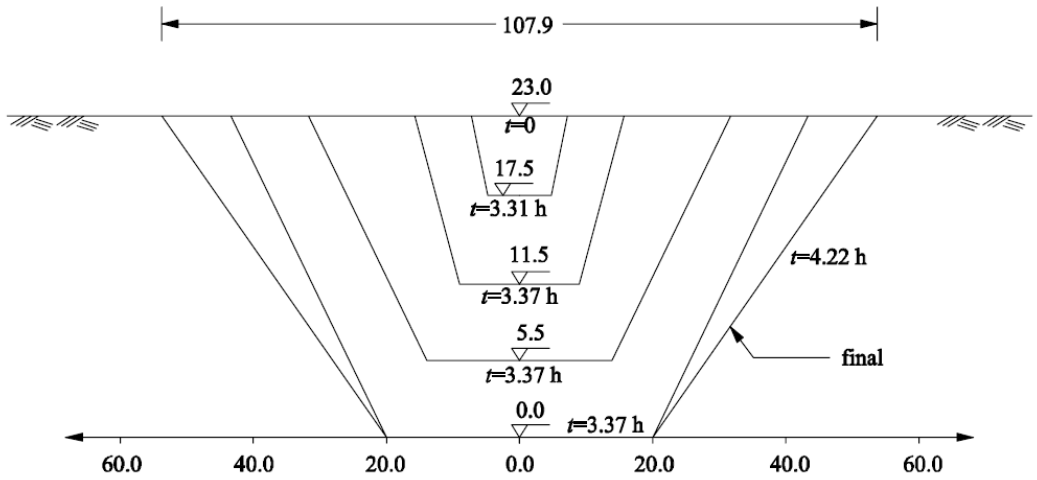


**Figure 2.3 Breaching process for the South Fork Dam simulated by the BEED model (all dimensions are expressed in m, after Singh, 1996)**

In the model of Visser (1998) for sand dikes, a relatively small initial breach is assumed in the top of the dike that is so large that water flowing through it will start the breach erosion process. By assuming a trapezoidal shape of the initial breach with the angle of repose, he distinguished the process of breach erosion for sand dike into five stages (Fig. 2.4):

I. Steepening erosion of the landside slope from the initial value to the critical value.
II. Retrograding erosion of the landside slope, yielding a decrease of the width of the crest of the dike in the breach.
III. Lowering of the top of the dike in the breach, with a constant angle of the critical breach side slopes, resulting in an increase of the width of the breach.
IV. Critical flow stage, in which the flow is virtually critical throughout the breach and the breach continues to grow mainly laterally.
V. Subcritical stage, in which the breach continues to grow, mainly laterally, due to the subcritical flow in the breach.

In the first three stages the initial breach cuts itself into the dike and most discharge through the breach happens in stages IV and V.

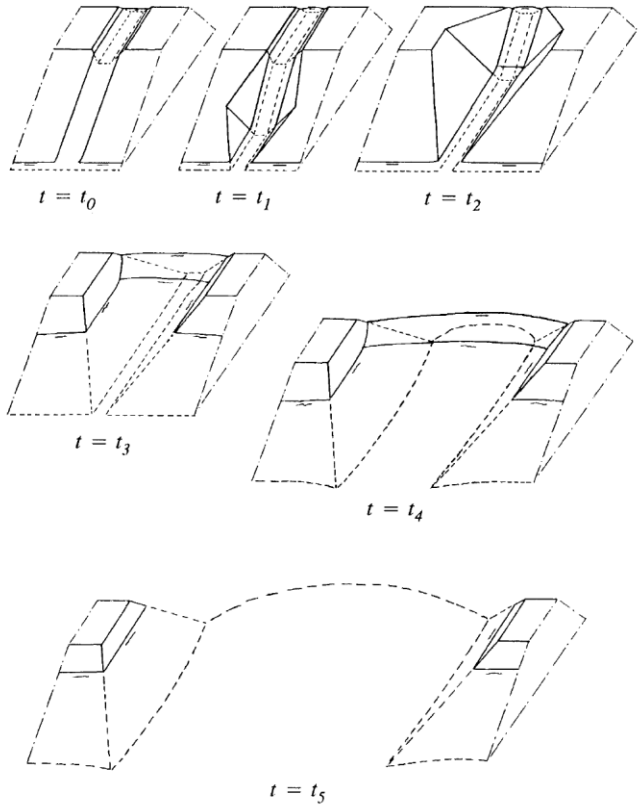


**Figure 2.4 Schematic illustration of breach growth in a sand dike (Visser, 1998)**

Corresponding to the study of sand-dike breaching by Visser, Zhu (2006) investigated the breaching processes of a clay dike. The distinct difference from a sand dike breaching is the large headcut erosion that occurs during the breaching process of clay dikes. Similarly, by assuming that the initial breach is relatively small and trapezoidal-shaped and located in the top of the dike, he classified the breach erosion process in clay dikes into five stages.

I. Stage I ($t_0 < t \le t_1$): Floodwater flows through the initial breach in the dike crest and erodes soil away from the landside slope of the dike. Flow shear erosion, as well as small-scale headcut erosion, can occur along the inner slope (Fig. 2.5(a)(b)).
II. Stage II ($t_1 < t \le t_2$): The steepened landside slope of the dike holds the critical slope

angle $\beta_1$ throughout Stage II and acts like a headcut during the erosion process owing to its large steepness (Fig. 2.5(b)(c)).

III. Stage III ($t_2 < t \le t_3$): The headcut still maintains the critical slope angle $\beta_1$. The breach enlarges rapidly, accordingly also the breach flow rate, which in turn accelerates the breach erosion process in the dike. At the end of the stage, the dike body in the breach has been washed away completely down to the dike foundation or to the toe protection on the waterside dike slope (Fig. 2.5(c)(d)).

IV. Stage IV ($t_3 < t \le t_4$): Breach erosion takes place mainly laterally, with flow shear erosion along the side slopes of the breach and the resulting discrete side slope instability being the main mechanisms for the breach enlargement. Vertical erosion in this stage relies mainly on the geometrical and material features of the dike (Fig. 2.5(d)(e)).

V. Stage V ($t_4 < t \le t_5$): The breach erosion still occurs mainly laterally and, in the end, the velocity of the breach flow is reduced to such an extent that it can no longer erode away soil material from either the dike body or the dike foundation, hence the breach growth process stops (Fig. 2.5(e)(f)).

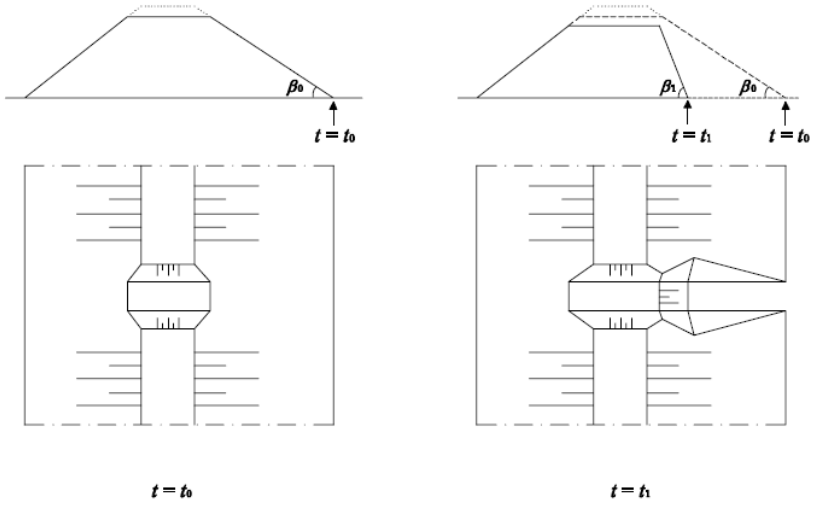


(a) (b)

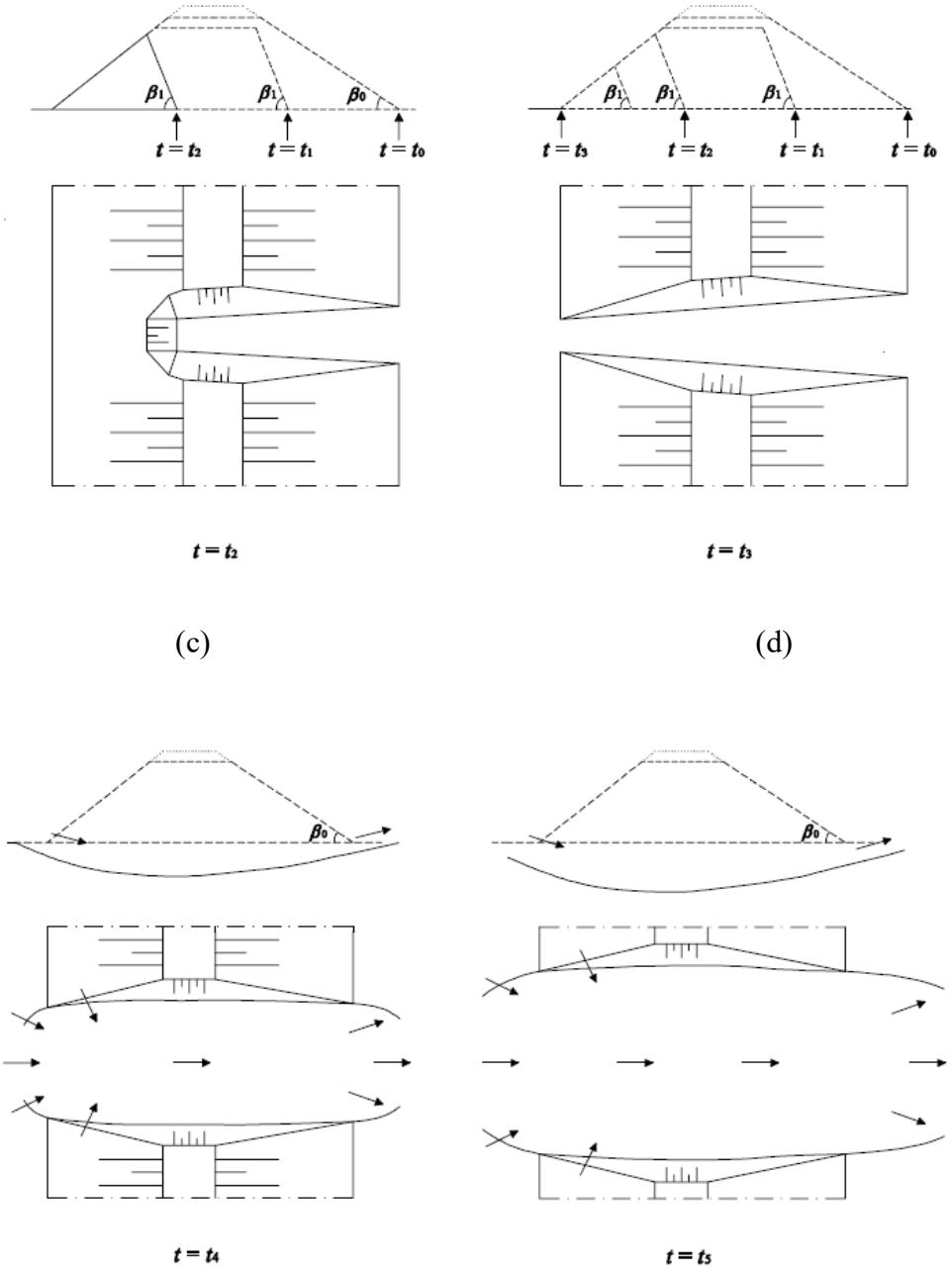


**Figure 2.5 Breach development process in clay dike (Zhu, 2006)**

By considering the variations in soil erodibility along the depth and the steepening of the downstream slope, Chang and Zhang (2010) studied the erosion process of landslide dams and divided the evolution of breach development into three stages:

I. The side slopes below the water level will be eroded and the side slopes above the water level will collapse. The breach channel bed will also be eroded. This process will continue until the side slopes reach a critical value. The top breach width does not change during this stage, whereas both the breach depth and breach bottom width increase gradually (Fig. 2.6(a)).

II. The side slopes continue to be eroded keeping the critical slope. The breach top width, bottom width, and breach erosion depth increase during this stage (Fig. 2.6(b)).

III. The breach slopes will recede laterally keeping the same side slope angle. During this stage, the breach erosion depth remains constant, whereas both the breach top width and bottom width increase. In the vertical direction, the breach cannot develop any further if it encounters a hard layer with an erosion resistance larger than the shear stress induced by the water flow (Fig. 2.6(c)).

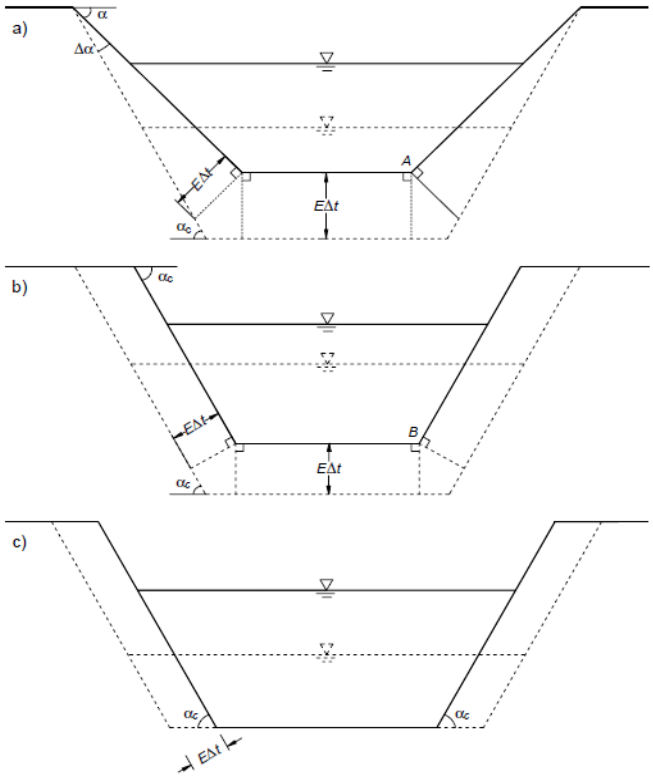


**Figure 2.6 Breach enlargement process, a) Stage I, b) Stage II, c) Stage III (Chang and Zhang, 2010)**

## 2.3 Mathematical Models

### 2.3.1 Non-Physically-Based models (Empirical Models)

Empirical models have been developed by fitting equations to a selection of past embankment failures, or with the use of probabilistic methods. Empirical models can be used to predict the embankment failures when comparing similar case studies. Generally, the breach parameters can be obtained to give good relations with embankment height, volume of water stored, etc.

Johnson and Illes (1976) made the earliest contribution by classifying the failure shapes for earth, gravity, and arch dams. For the earthen dams, with the development of the breach, the breach shape was described as varying from triangular to trapezoidal. Most of the earthen dam breaches are described as trapezoidal shapes.

The advantage of these equations is their simplicity; there is no need to run computer models. However, this simplicity is also one of their main weaknesses, in the considerable uncertainty within the predictions. Users often have little knowledge of the data set upon which the equations were developed and hence any constraints of the application and the suitability of the application to site specific cases are unknown.

An additional limitation of these equations is that only discrete values are predicted by the equations. For example, peak discharge rather than a whole flood hydrograph is predicted, or final breach width rather than the time varying growth. When using peak discharge equations it should be recognized that the worst-case flood conditions do not always relate to peak discharge. For the Tous case study in the IMPACT project, Morris (2005) provided an example where the worst-case flooding from a dam break does not correspond to the peak breach discharge, and where breach flooding is a function of volume and rate of water release, combined with topographic features. An additional source of uncertainty when using peak discharge equations is that users requiring a flood hydrograph, will then typically estimate a hydrograph around the peak value given by the equation. The estimated hydrograph might conserve reservoir volume, but is likely to

increase the error in a flow calculation by introducing further assumptions, such as rate of breaching, of which there is no basis available to make predictions.

Wahl (2004) presented a quantitative analysis of the uncertainty associated with the empirical models (shown in Table 2.1), and concluded that there are wide bands of uncertainty within the processes. His work does demonstrate the basis upon which many of the equations have been developed and offers guidance on the selection of the most appropriate equations. In Table 2.1, the first columns identify the method of analysis, the following two columns show the number of case studies used to test the method, and the next two columns give the prediction error and the width of the uncertainty band. The last column shows the range of the prediction interval around a hypothetical predicted value of 1.0. The values in this column can be used as multipliers to obtain the prediction interval for a specific case.

The four methods (shown in Table 2.2) for predicting breach width all have absolute mean prediction errors in an order of magnitude of less than 1/10, indicating that their predictions are on target. The uncertainty bands are similar (±0.3 to ±0.4 log cycles) for all the equations except the MacDonald and Langridge-Monopolis equation, which has an uncertainty of ±0.82 log cycles.

The five methods (shown in Table 2.3) for predicting failure time all underpredict the average failure time, by amounts ranging from about 1/5 to 2/3. This is consistent with the previous observation, that these equations are designed to conservatively predict fast breaches, causing large peak outflows. The uncertainty bands on all of the failure time equations are very large, ranging in an order of magnitude from ±0.6 to 1, with the Froehlich (1995a) equation having the smallest uncertainty.

Most of the peak flow prediction equations tend to overpredict the observed peak flows, with most of the “envelop” equations overpredicting by an order of magnitude of about 2/3 to 3/4. The uncertainty bands on the peak flow prediction equations are about ±0.5 to 1 order of magnitude, except the Froehlich (1995b) relation, which has an uncertainty of

0.32 order of magnitude (Froehlich, 1995a). In fact, the Froehlich equation has both the lowest prediction error and smallest uncertainty of all peak flow prediction equations.

Predictions of the Teton Dam failure breach width with different empirical equations are summarized in Table 2.2. In the table the predictions are given of the volume of eroded embankment material, using the MacDonald and Langridge-Monopolis equation, and the corresponding estimate of average breach width.

**Table 2.1 Uncertainty estimates for breach parameter and peak flow prediction equation (Wahl, 2004)**

| Reference | Equation | Number of case studies: Before outlier exclusion | Number of case studies: After outlier exclusion | Mean prediction error (log cycles) | Width of uncertainty band, $\pm 2S_e$ (log cycles) | Prediction interval around hypothetical predicted value of 1.0 |
|---|---|---|---|---|---|---|
| Breach width equations | | | | | | |
| Bureau of Reclamation (1988) | $B_{avg} = 3h_w$ | 80 | 70 | −0.09 | ±0.43 | 0.45–3.3 |
| MacDonald and Langridge-Monopolis (1984) | $V_{er} = 0.0261(V_w h_w)^{0.769}$ earthfill<br>$V_{er} = 0.00348(V_w h_w)^{0.852}$ nonearthfills (e.g., rockfills) | 60 | 58 | −0.01 | ±0.82 | 0.15–6.8 |
| Von Thun and Gillette (1990) | $B_{avg} = 2.5h_w + C_b$ | 78 | 70 | +0.09 | ±0.35 | 0.37–1.8 |
| Froehlich (1995a) | $B_{avg} = 0.1803K_o V_w^{0.32} h_b^{0.19}$ | 77 | 75 | +0.01 | ±0.39 | 0.40–2.4 |
| Failure time equations | | | | | | |
| MacDonald and Langridge-Monopolis (1984) | $t_f = 0.0179V_{er}^{0.364}$ | 37 | 35 | −0.21 | ±0.83 | 0.24–11 |
| Von Thun and Gillette (1990) | $t_f = 0.015h_w$ highly erodible<br>$t_f = 0.020h_w + 0.25$ erosion resistant | 36 | 34 | −0.64 | ±0.95 | 0.49–40 |
| Von Thun and Gillette (1990) | $t_f = B_{avg}/(4h_w)$ erosion resistant<br>$t_f = B_{avg}/(4h_w + 61)$ highly erodible | 36 | 35 | −0.38 | ±0.84 | 0.35–17 |
| Froehlich (1995a) | $t_f = 0.00254(V_w)^{0.53} h_b^{-0.9}$ | 34 | 33 | −0.22 | ±0.64 | 0.38–7.3 |
| Bureau of Reclamation (1988) | $t_f = 0.011(B_{avg})$ | 40 | 39 | −0.40 | ±1.02 | 0.24–27 |
| Peak flow equations | | | | | | |
| Kirkpatrick (1977) | $Q_p = 1.268(h_w + 0.3)^{2.5}$ | 38 | 34 | −0.14 | ±0.69 | 0.28–6.8 |
| SCS (1981) | $Q_p = 16.6(h_w)^{1.85}$ | 38 | 32 | +0.13 | ±0.50 | 0.23–2.4 |
| Hagen (1982) | $Q_p = 0.54(S \cdot h_d)^{0.5}$ | 31 | 30 | +0.43 | ±0.75 | 0.07–2.1 |
| Bureau of Reclamation (1982) | $Q_p = 19.1(h_w)^{1.85}$ envelope eq. | 38 | 32 | +0.19 | ±0.50 | 0.20–2.1 |
| Singh and Snorrason (1984) | $Q_p = 13.4(h_d)^{1.89}$ | 38 | 28 | +0.19 | ±0.46 | 0.23–1.9 |
| Singh and Snorrason (1984) | $Q_p = 1.776(S)^{0.47}$ | 35 | 34 | +0.17 | ±0.90 | 0.08–5.4 |
| MacDonald and Langridge-Monopolis (1984) | $Q_p = 1.154(V_w h_w)^{0.412}$ | 37 | 36 | +0.13 | ±0.70 | 0.15–3.7 |
| MacDonald and Langridge-Monopolis (1984) | $Q_p = 3.85(V_w h_w)^{0.411}$ envelope eq. | 37 | 36 | +0.64 | ±0.70 | 0.05–1.1 |
| Costa (1985) | $Q_p = 1.122(S)^{0.57}$ | 35 | 35 | +0.69 | ±1.02 | 0.02–2.1 |
| Costa (1985) | $Q_p = 0.981(S \cdot h_d)^{0.42}$ | 31 | 30 | +0.05 | ±0.72 | 0.17–4.7 |
| Costa (1985) | $Q_p = 2.634(S \cdot h_d)^{0.44}$ | 31 | 30 | +0.64 | ±0.72 | 0.04–1.22 |
| Evans (1986) | $Q_p = 0.72(V_w)^{0.53}$ | 39 | 39 | +0.29 | ±0.93 | 0.06–4.4 |
| Froehlich (1995b) | $Q_p = 0.607(V_w^{0.295} h_w^{1.24})$ | 32 | 31 | −0.04 | ±0.32 | 0.53–2.3 |
| Walder and O'Connor (1997) | $Q_p$ estimated by computational and graphical method using relative erodibility of dam and volume of reservoir | 22 | 21 | +0.13 | ±0.68 | 0.16–3.6 |

Note: All equations use metric units (m, $m^3$, $m^3/s$). Failure times are computed in hours. Where multiple equations are shown for application to different types of dams (e.g., earthfill versus rockfill), a single prediction uncertainty was determined, with the *set* of equations considered as a single algorithm.

**Table 2.2 Prediction of average breach width in Teton Dam failure (Wahl, 2004)**

| Equation | Top of joint use, elevation of 436.68 m | | Top of flood space, elevation of 443.18 m | |
|---|---|---|---|---|
| | Predicted breach width (m) | 95% prediction interval | Predicted breach width (m) | 95% prediction interval |
| Bureau of Reclamation (1988) | 39.0 | 17.7–129 | 58.5 | 26.2–193 |
| Von Thun and Gillette (1990) | 87.5 | 32.3–157 | 104 | 38.4–187 |
| Froehlich (1995a) | 93.6 | 37.5–225 | 166 | 66.4–398 |
| MacDonald and Langridge-Monopolis (1984) | *146,000* | *22,200–991,000* | *787,000* | *118,000–5,350,000* |
| Volume of erosion ($m^3$) | | | | |
| Equivalent breach width (m) | 85.6 | 12.8–582[a] | 462[a] | 69.2–3140[a] |
| Recommended values (m) | 90 | 35–180 | 165 | 60–400 |

[a]Exceeds actual embankment length.

Failure time predictions of Teton Dam failure are summarized in Table 2.3. All of the equations indicate increasing failure times as the reservoir storage increases, except the second Von Thun and Gillette relation, which predicts a slight decrease in failure time for the top-of-flood-space scenario. For both Von Thun and Gillette relations, the dam was assumed to be in the erosion resistant category.

**Table 2.3 Failure time prediction in Teton Dam failure (Wahl, 2004)**

| Equation | Top of joint use, elevation of 436.68 m | | Top of flood space, elevation of 443.18 m | |
|---|---|---|---|---|
| | Predicted failure time (h) | 95% prediction interval | Predicted failure time (h) | 95% prediction interval |
| MacDonald and Langridge-Monopolis (1984) | 1.36 | 0.33–14.9 | 2.45[a] | 0.59–26.9 |
| Von Thun and Gillette (1990), $t_f=f(h_w)$ | 0.51 | 0.25–20.4 | 0.64 | 0.31–25.6 |
| Von Thun and Gillette (1990), $t_f=f(B,h_w)$ | 1.68 | 0.59–28.6 | 1.33 | 0.47–22.6 |
| Froehlich (1995a) | 1.63 | 0.62–11.9 | 4.19 | 1.59–30.6 |
| Bureau of Reclamation (1988) | 0.43 | 0.10–11.6 | 0.64 | 0.15–17.4 |
| Recommended values | 1.5 | 0.25–12 | 3.0 | 0.3–17 |

[a]Predicted erosion volume exceeded total embankment volume; total embankment volume was used in the failure time equation.

Peak outflow estimations of the Teton Dam failure are shown in Table 2.4 in order of increasing peak outflow for the top-of-joint-use scenario. The lowest peak flow predictions come from those equations that are based solely on the dam height or the water depth in the reservoir. The highest peak flows are predicted by those equations that incorporate a significant dependence on reservoir storage. Some of the predicted peak

flows and the upper bounds of the prediction limits would be the largest breach outflow ever recorded, exceeding the 65,000 $m^3/s$ peak outflow from the Teton Dam failure.

**Table 2.4 Prediction of peak breach outflow in Teton Dam failure (Wahl, 2004)**

| | Top of joint use, elevation of 436.68 m | | Top of flood space, elevation of 443.18 m | |
|---|---|---|---|---|
| Equation | Predicted peak outflow ($m^3/s$) | 95% prediction interval | Predicted peak outflow ($m^3/s$) | 95% prediction interval |
| Kirkpatrick (1977) | 818 | 229–5,570 | 2,210 | 620–15,100 |
| SCS (1981) | 1,910 | 439–4,590 | 4,050 | 932–9,710 |
| Bureau of Reclamation (1982) (envelope) | 2,200 | 439–4,620 | 4,660 | 932–9,780 |
| **Froehlich (1995b)** | **2,660** | **1,410–6,110** | **7,440** | **3,940–17,100** |
| MacDonald/Langridge-Monopolis (1984) | 4,750 | 714–17,600 | 11,700 | 1,760–43,400 |
| Singh/Snorrason (1984), $Q_p=f(h_d)$ | 5,740 | 1,320–10,900 | 5,740 | 1,320–10,900 |
| **Walder and O'Connor (1997)** | **6,000** | **960–21,400** | **12,200** | **1,950–43,500** |
| Costa (1985), $Q_p=f(S^*h_d)$ | 6,220 | 1,060–29,200 | 13,200 | 2,240–61,900 |
| Singh/Snorrason (1984), $Q_p=f(S)$ | 7,070 | 570–38,200 | 16,400 | 1,310–88,400 |
| Evans (1986) | 8,260 | 496–36,300 | 21,300 | 1,280–93,700 |
| MacDonald/Langridge-Monopolis (1984) (envelope) | 15,500 | 776–17,100 | 38,300 | 1,910–42,100 |
| Hagen (1982) | 18,100 | 1,270–38,100 | 44,300 | 3,100–93,000 |
| Costa (1985), $Q_p=f(S^*h_d)$ (envelope) | 25,300 | 1,010–30,900 | 55,600 | 2,220–67,800 |
| Costa (1985), $Q_p=f(S)$ | 26,100 | 521–54,700 | 72,200 | 1,440–152,000 |

The equation of Froehlich (Table 2.4) has the best prediction performance in the uncertainty analysis. This equation has the smallest mean prediction error and the narrowest prediction interval by a significant margin. The results for the Walder and O'Connor method (1997) are also good enough. This is the only method that considers the differences between the so-called large-reservoir/fast-erosion and small-reservoir/ slow-erosion. Results from the Froehlich method (1995b) are considered to be the best estimate of peak breach outflow, and the results from the Walder and O'Connor method (1997) provide a higher estimation of the peak discharge.

Basically a model can be developed to estimate the outflow hydrograph from a failed embankment. In spite of the simplicity of these methods, they often require the model user to provide an erosion rate for the breach growth, or the final dimensions of the breach shape and time of failure of the embankment. The model simply predicts a growth pattern to fit these parameters and hence produces a flood hydrograph. However, these parameters cannot be easily identified and they can differ significantly from one case to

another. Hence, whilst these models appear to provide a more accurate prediction of the flood hydrograph as compared to empirical equations, they simply reflect the data provided by the user and hence can also include the large degree of uncertainty within these data.

### 2.3.2 Physically-Based Models

Physically-based numerical models simulate the failure of embankments based on the processes observed during failure, such as flow regimes, erosion and instability processes. In the last four decades many models have been developed to simulate the failure of embankments. These models differ in their complexity, in the assumptions involved and in the techniques used. According to the mechanics of embankment breaching, the physical processes observed are first simulated in the physical model, which is then used to simulate different cases. This type of model is created combining hydraulic theory, sediment transport, and soil mechanics. The model provides an estimation of the breach formation process and subsequently the potential flood hydrograph. The advantage of this approach is that it can be used to estimate the breaching process and, subsequently the potential hydrograph.

Kahawita (2007) subdivided physically-based models into empirical and theoretical models, based upon the degree of use of empirical relationships within the model versus theoretical processes. A recent example of a physically-based empirical model is given as SIMBA (Hanson *et al.,* 2005; Temple *et al*., 2005). SIMBA predicts the growth and progression of headcut advance through cohesive material, thus predicting the stages of breach formation, flood hydrograph and breach dimensions. The model is based around the use of an erodibility coefficient for the embankment soil, the value of which is determined experimentally.

The physically-based theoretical models include BRES (Visser, 1998), BRES-Zhu (Zhu, 2006), FIREBIRD (Wang and Kahawita, 2002; Wang *et al.*, 2006) and HR BREACH (Mohamed, 2002; Morris *et al*., 2009a; Morris *et al*., 2009b). These models attempt to use theoretical relationships to simulate the physical processes. However, invariably there

is always a degree of empirical relationships embedded within the models, since model "factors" are generally included at the detailed level of model simulation (e.g. weir discharge coefficients).

The most famous of all of these models is probably the NWS BREACH model developed by Fread in the 1980's (Fread, 1987). This model was developed and distributed as part of the NWS DAMBRK model, which has been widely used around the world. As with many other models, problems with prediction accuracy have been found with this model (Mohamed, 1998).

Developments in the understanding of breaching processes, soil mechanics and computing power mean that more recent models, such as BRES, BRES-Zhu, SIMBA, FIREBIRD and HR BREACH, now offer more detailed analyses.

The advantages of using physically based-models include:

• Breach growth processes are simulated by modelling observed physical processes, generally incorporating aspects of hydraulics, sediment transport, soil mechanics and structural behaviour;

• A real estimate of the outflow hydrograph and the breach growth process is predicted, without predefining or constraining the predicted growth process;

• Uncertainties within individual processes or parameters may be included within the model.

The disadvantages of using physically-based models typically include:

• Computer programs are required; model runtimes can become quite long as the simulation of processes becomes more complex;

• Current computing power means that 1D/pseudo 2D models incorporating hydraulics, sediments, soil mechanics and structural stability are feasible; 2D/pseudo 3D models incorporating all of these elements are being considered and developed, but are not yet practical in terms of model runtime or validated in terms of improved performance (relative to the faster 1D models).

### 2.3.3 Semi-Physically-Based Models

The large range of uncertainty associated with the non-physically-based methods on one hand and the complexity of the physically-based methods on the other hand, prompted researchers such as Singh (Singh and Scarlatos, 1989) and Walder (Walder and O'Connor, 1997) to develop models based on physical processes, but with simplified assumptions to model the failure of embankment dams.

The purpose of these models is to improve the prediction capability by adding some of the physical process (or processes) involved in the failure without complicating the computation procedure. The following assumptions are usually made in such models:

I) A weir equation can adequately present the flow over the embankment;
II) Critical flow conditions exist on the embankment crest;
III) The breach geometry is time dependent.

## 2.4 Breach Experiments

Breach experiments have played an important role in the process of understanding the embankment breaching processes. Wahl (2007) exposed more than 325 embankment breaching tests dating from the end of the 19$^{th}$ century up to 2007. Most experiments focused on simple homogeneous embankments, although some efforts have been taken to study the composite embankments, e.g. the embankment with a core and other structures.

### 2.4.1 Laboratory Experiment

#### Tests in HR Wallingford

A total of 22 laboratory experiments were undertaken at HR Wallingford in the UK (Morris *et al.*, 2005). The overall objective of these tests was to better understand the breaching processes in embankments failed by overtopping or piping, and to identify the important parameters that influence these processes. These tests were divided into 3 series. Table 2.5 shows the details of each series of tests. Fig. 2.7 shows a photo taken in Test 2.

**Table 2.5 Description of laboratory experiment at HR Wallingford**

| Laboratory Test Description | | Laboratory Test Objective |
|---|---|---|
| Series # 1 (9 tests) [Fig 8] | This series of tests was based around the homogeneous non-cohesive field test at scale of 1:10. Each embankment was built from non-cohesive material, however, more than one grading of sediment were used along with different embankment geometry, breach location and time before failure (seepage effect). | To better understand breach formation processes and to identify the effect of a variety of parameters on these processes in homogeneous non-cohesive embankments failed by overtopping |
| Series # 2 (8 tests) [Fig 13] | This series of tests was based around the homogeneous cohesive field test at scale of 1:10. Each embankment was built from cohesive material, however, two different grading of sediment were used along with different embankment geometry, compaction effort and moisture content. | To better understand breach formation processes and to identify the effect of a variety of parameters on these processes in homogeneous cohesive embankments failed by overtopping |
| Series # 3 (5 tests) | Assess initiation of the piping mechanism and dimensions for the homogeneous field test | Provide information about the pipe formation to assist in development of the field test failure mechanism |
| | Material brought from a UK flood embankment. Samples were 1m (W) x 1m (L) x 0.8m (D) | Monitor piping initiation and development |

**Figure 2.7 Breach of sandy dike in HR Wallingford (Test 2)**

**Tests in Delft University of Technology**

Zhu (2006) conducted 5 series of embankment breaching experiments in the Laboratory for Fluid Mechanics of Delft University of Technology, the Netherlands. The tests confirmed that headcut erosion plays a very important role in the process of breach growth in embankments constructed with cohesive materials. Comparisons of the breaching time between the five tests indicated that the cohesive portion in the sand-silt-clay soil mixtures strongly slowed down the erosion process, i.e., the higher the proportion of clay in the soil mixtures was, the lower the erosion rate.

## 2.4.2 Field Experiment

**Field Test in IMPACT**

A total of 7 field tests (Table 2.6) were performed, with 5 tests being part of the IMPACT project in Norway (Morris *et al.*, 2005). The field tests have provided an overview of the field work undertaken in Norway during the last few years, aimed at collecting reliable information and data sets detailing the failure mechanisms of a range of different embankment dams. Prior to these tests extensive planning and lab-work was undertaken. Reliable data sets now exist for the failure of a range of different large-scale embankment geometries and material types. The data will assist in the development and validation of

predictive models. Prior to this analysis, rather broad observations were made, based upon field observations and data analysis to date. The 5 large-scale IMPACT field tests were carried out at the downstream from the Røssvass Dam in northern Norway (Morris *et al.,* 2005). The variables included embankment heights (4.5 m, 5 m, and 6 m), materials (cohesive, non-cohesive and composite) and failure mechanisms (overtopping and piping). Fig. 2.8 shows photos of two field tests: an overtopping breach and a piping breach in cohesive embankments.

**Figure 2.8 Field tests undertaken in the IMPACT project (Morris *et al.*, 2005)**

**Table 2.6 Lists of the tests in IMPACT (Morris *et al.*, 2005)**

| Test No. | Type of dam | Objective | EC-IMPACT |
|---|---|---|---|
| 1 | Homogeneous rockfill dam<br>a) three different test with specially built drainage toe<br>b) Toe removed and the dam brought to failure | Test of stability with high through flow and breaching mechanism of a rock filling. | |
| 2 (1-2002) | Homogeneous clay fill dam | Breaching mechanism of a homogenous cohesive dam | IMPACT |
| 3 (2-2002) | Homogenous gravel dam<br>a) With a rockfill berm up the downstream slope<br>b) With rockfill berm partly removed<br>c) With rockfill berm removed and dam brought to failure | Test of stability of gravel dam and study of the breaching mechanism of a dam of non-cohesive material | 3C is part of the IMPACT project |
| 4 | Homogeneous rockfill dam, but with a smaller crest width and coarser rockfill than that used in Test # 1. | Test of stability with high through flow and breaching mechanism of a rock filling. | |
| 5 (1-2003) | Rockfill dam with central moraine core. Dam was failed by overtopping | Study of the breaching mechanism | IMPACT |
| 6 (2-2003) | Rockfill dam with central moraine core. Dam was failed by internal erosion | Study of the breaching mechanism | IMPACT |
| 7 (3-2003) | Homogeneous dam made of same moraine as for the core in Tests # 5 and #6. Dam was failed by internal erosion. | Test #7 was run to compare the progression of the breaching process with that observed in test # 6 | IMPACT |

**Field Test in Nanjing Hydraulic Research Institute (NHRI), China**

Zhang *et al.* (2009) conducted a series of the world's largest large-scale dam breach field tests with the widest range of clay content (the largest height of the dam is 9.7 m and the range of the cohesion of filling is from 7.5 kPa to 39.5 kPa). The main parameters for the tests are shown in Table 2.7.

**Table 2.7 Main parameters for the field test in NHRI (Zhang, *et al*., 2009)**

| Test group | F1 | F2 | F3 | F4 |
|---|---|---|---|---|
| Clay content (%) | 11.50 | 11.50 | 17.80 | 33 |
| Compactness (%) | 97 | 96 | 98 | 92 |
| Water content (%) | 19.42 | 15.74 | 17.60 | 28.55 |
| $C$ (kPa) | 9.3 | 7.5 | 13 | 39.5 |
| $\varphi$ | 28.25 | 27.8 | 16 | 14.4 |
| Threshold friction velocity of undisturbed earth $U_{*c}$ (m/s) | 0.06 | 0.06 | 0.17 | 0.35 |

Three breaching mechanisms were considered in these tests: (1) source-tracing erosion of the dam body with the form of "multi-level headcut", (2) "two-helix flow" erosion of the dam crest, and (3) collapse of the breach sidewalls due to instability. Zhang *et al.* (2009) concluded that the cohesive strength of the earth dam filling has a great effect on the breach formation. When the cohesive strength is large, the main character of the breach formation consists of headcutting and dumping collapse (Fig. 2.9); on the other hand, if the cohesive strength is limited, the main character of the breach formation is single level headcutting and shearing collapse.

**Figure 2.9 Earthen dam breach test in Nanjing Hydraulic Research Institute (Zhang, *et al*., 2009)**

In the field tests, the multi-level headcut happened in the breaching process, as shown in Fig. 2.10. A headcut develops due to the material difference among the filling layers in the embankment.

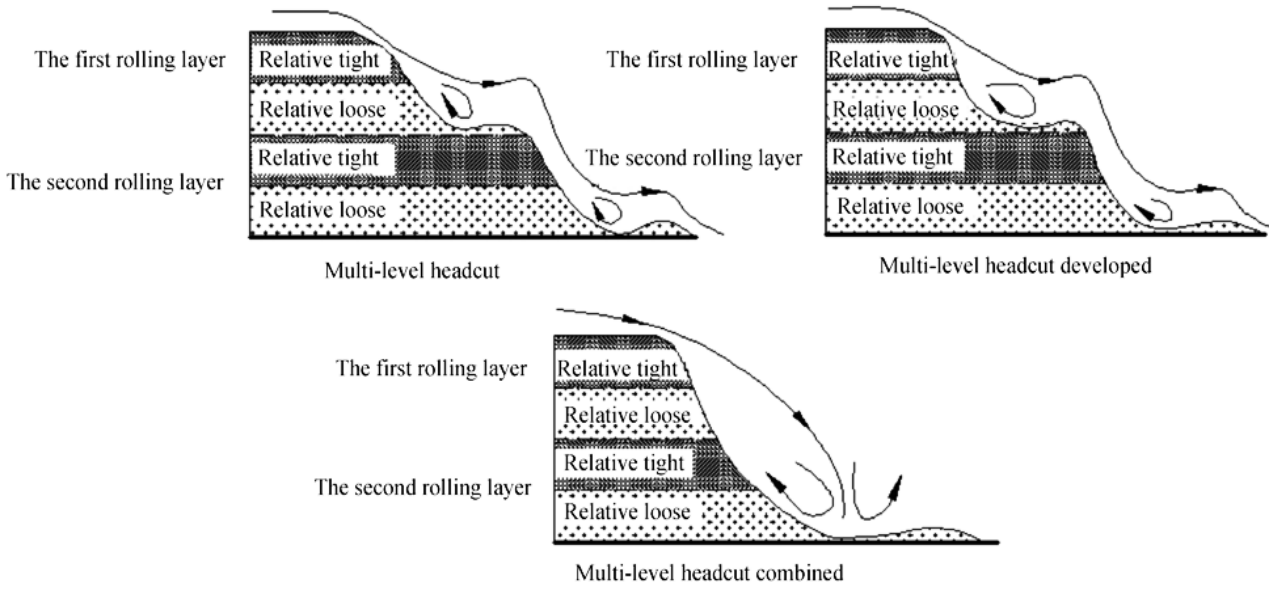


**Figure 2.10 Multi-level headcut erosion developing process (Zhang, *et al*., 2009)**

The breach parameters for an earthen dam of different cohesion levels are listed in Table 2.8. It can be concluded that the final width and depth of the breach and the peak outflow will become smaller, and the speed of the vertical cutting and horizontal expansion will be slower as the cohesion of the dam filling is greater. The main cause is that the anti-scouring ability increases with the increase of the cohesion of the filling.

**Table 2.8 Comparison of important breach parameters for earth dam with different cohesive fillings**

| | *C* (kPa) | Depth of breach (m) | Width of breach on the top (m) | Width of breach on the bottom (m) | Peak outflow (m/s) | Speed of vertical cutting (cm/s) | Speed of horizontal expansion (cm/s) | Shape |
|---|---|---|---|---|---|---|---|---|
| F2 | 7.5 | 4.1 | 17 | 3.7 | 42.25 | 0.44 | 1.49 | inverted trapezoid |
| F3 | 13 | 1.7 | 2.1 | 7.1 | 3.7 | 0.022 | 0.065 | trapezoid |
| F4 | 39.5 | 1.1 | 1.3 | 0.9 | 1.07 | 0.011 | 0.024 | big hole |

## 2.5 Prototype Measurement

Usually it is very hard to measure the breaching process in prototype embankments, because the breaching process is very fast and is dangerous to measure. Up to now, there are few documents for the breaching process in prototypes. However, people recorded the whole breaching process of the Tangjiashan Landslide Barrier in China, 2008 (Liu *et al*., 2009). The Tangjiashan Landslide Barrier, with a height of 82 -124 m, a volume of 24.37 million $m^3$ and a reservoir volume of 326 million $m^3$, is the largest landslide barrier induced by the Ms 8.0 Wenchuan Earthquake on 12 May, 2008. An uncontrolled breaching failure of this landslide barrier would threaten more than 1.3 million people downstream of the Tangjiashan Lake.

A variety of remote sensing techniques were applied to measure the main characteristics of the landslide deposit, which are summarized in Table 2.9. The landslide debris is composed of complex materials, varying from rocks (mainly with its original structures to completely weathered rocks) to soils with tree roots. In order to slowly and effectively reduce the reservoir water level of the Tangjiashan Landslide Barrier, a manmade breach channel was excavated in the crest of the barrier.

**Table 2.9 Main Characteristics of the landslide slope, deposit, and the barrier lake (Liu *et al*., 2010)**

| Item | Parameters | Magnitude |
|---|---|---|
| Landslide slope | Occurrence of the natural slope, dip direction/dip angle | 344°/30° |
| | Occurrence of the bedding planes, dip direction/dip angle | 330°/60° |
| | Height of the failed slope | 542 m |
| | Elevation of the landslide headscarp | 1,205 m |
| | Elevation at the top of the natural slope | 1,580 m |
| Landslide dam | Volume of the landslide deposit | $24.37\times10^6$ $m^3$ |
| | Elevations of crest/toe, measured at the highest crest surface of the left deposit | 793.9/669.6 m |
| | Elevations of crest/toe, measured at the lowest crest surface of the right deposit | 753.0/663.0 m |
| | Length along the river valley (bottom of the deposit) | 803 m |
| | Length across the river valley | 611 m |
| | Ratio of length over thickness near the left abutment | 8.9 |
| | Covered area | $3.07\times10^5$ $m^2$ |
| Reservoir | Potential highest water level without intervention works | 753 m |
| | Potential storage of water without intervention works | $326\times10^6$ $m^3$ |
| | Elevation of the original river bed | 663 m |
| | Area of the reservoir water surface | 3,550 $km^2$ |

On June 7, 2008, the water level reached 740.3 m (above the Huanghai Sea, China) and the man-made (dredged) pilot channel started overflowing. However, no rapid flow developed until about 6:00 am on June 10, when the water level reached 742.1 m. Following the increase in the flow rate, rapid erosion, widening and deepening of the dredged channel caused the pool water level to drop dramatically. The breaching process is shown in Fig. 2.11.

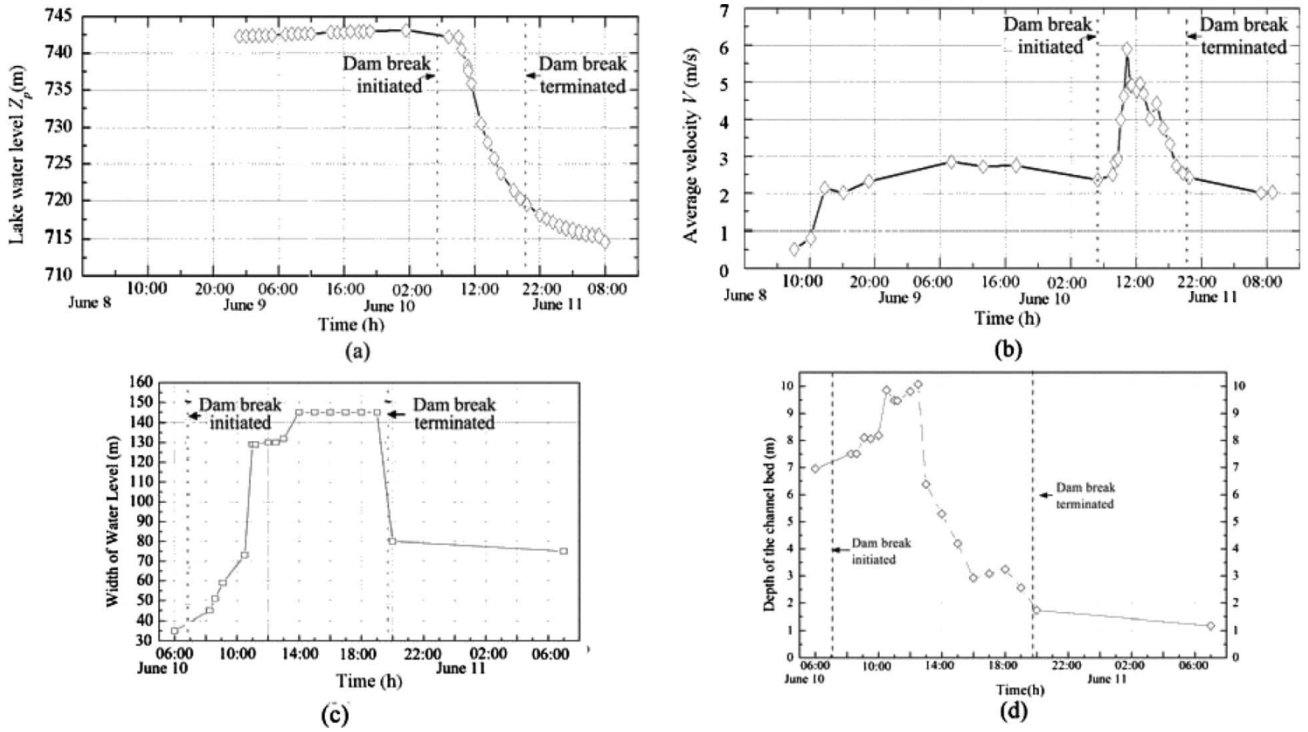


**Figure 2.11 Tangjiashan barrier breaching process versus time: (a) Landslide barrier lake water; (b) Average velocity upstream of breaching channel; (c) Breaching channel width; (d) Breaching channel depth (Liu *et al.*, 2009)**

## 2.6 Discussion

Embankment breaching is a complex process coupling hydraulic and geotechnical processes. The embankment breaching process can be divided into several stages according to the researchers' hypotheses, prototype surveys, and laboratory experiments (Visser, 1998; Zhu, 2006; Chang and Zhang, 2010). Researchers (Fread, 1987; Sigh, 1996) have different methods to classify the breaching processes according to the

different embankment materials. The present study doesn't follow, however, the methods of dividing the breach growth into 5 stages (Visser, 1998; Zhu, 2006). Zhu (2006) proposed that the erosion in a clay dike breach was in the form of single sediment particles, however, the clay is eroded in the form of clay blocks in the prototype dike breach test and clay blocks occur in the headcut and lateral migration of the embankment breach (Zhang, *et al.,* 2009; Peeters, *et al.*, 2014). Thus it is important to develop a clay erosion model to describe the clay blocks erosion phenomenon. Hence in this research it is proposed that the breach growth process consists of initial erosion, headcut erosion and lateral erosion.

Mathematical models have been developed, mainly based on empirical methods, physically-based methods and semi-physically-based methods. Empirical models have been developed with probabilistic methods and/or based on case studies. Empirical models can only be used in similar case studies. Semi-physically-based models involve not only the empirical data, but also the physical processes. A physically-based model is completely developed according to the real physical processes of breaching. On the whole, it can be concluded that empirical models are simple, but have a low reliability, and that physically-based models are complex, but predictions are more reliable. In order to develop a physically-based model, the physical processes of breaching or the breaching mechanics require to be discovered. Therefore, physically-based model studies are urgently needed to improve and push the breach model development further. Large and/or semi-real scale physical model tests were undertaken in this research, which is the valuable and useful tool to solve the breach models' bottleneck (reliable data for calibrations and validations).

# Chapter 3 Hydraulics of Embankment Breaching[1]

## 3.1 Introduction

Embankment breaching is a combined process coupling hydraulic processes and geotechnical processes. Visser (1998) divided the sandy dike breaching process into 5 phases and idealized the flow over the breach as a weir flow. In the different phases of the breaching process, the breach flows have their own characteristics. The characteristics change with the development of the breach, i.e., the breach erosion process affects the hydraulic characteristics and the breach hydraulics give feedback to the breach erosion. This chapter studies the breach flow as a weir flow by using theoretical analyses and flume experiments.

In the beginning of the breaching process induced by overtopping, the flow over the embankment crest starts to erode the downstream slope of the embankment and, possibly, also the embankment crest. This process is called the breach initiation. The breach flow develops in the compound weir condition, when the breach flow overtops the entire embankment crest and breach channel. As the breach channel becomes wider and deeper due to erosion, the upstream water level may decrease and the flow continues only through the breach channel. Generally the breach flow develops from compound weir condition in the initiation phase into a single weir condition when the breach channel is enlarged and deepened due to the erosion. The compound weir condition and the single weir condition can be transferred due to upstream water level changes. The flow could transfer from a single weir condition into the compound weir condition due to a rising upstream water level.

[1] This chapter is based on "Gensheng Zhao, Paul J. Visser, Yankai Ren, Wim S.J. Uijttewaal. Flow Hydrodynamics in Embankment Breach. Journal of Hydrodynamics, 2015, 27(6): 835-844. DOI: 10.1016/S1001-6058(15)60311-9".

In the process of breaching, the discharge through the breach varies with different upstream water levels as well as with different breach shapes. The converged flow goes into the breach channel from the upstream. In the breach channel, there is not only a critical flow, but there are also shock waves that propagate downstream of the breach (Fig. 3.1(a)). Eddy zones are generated due to the non-uniform distribution of the breach flow. The breach flow starts as a subcritical flow in the upstream, then becomes a critical flow, later develops into a supercritical flow, and finally changes back into a subcritical flow downstream of the hydraulic jumps when it passes through the breach (Fig. 3.1(b)).

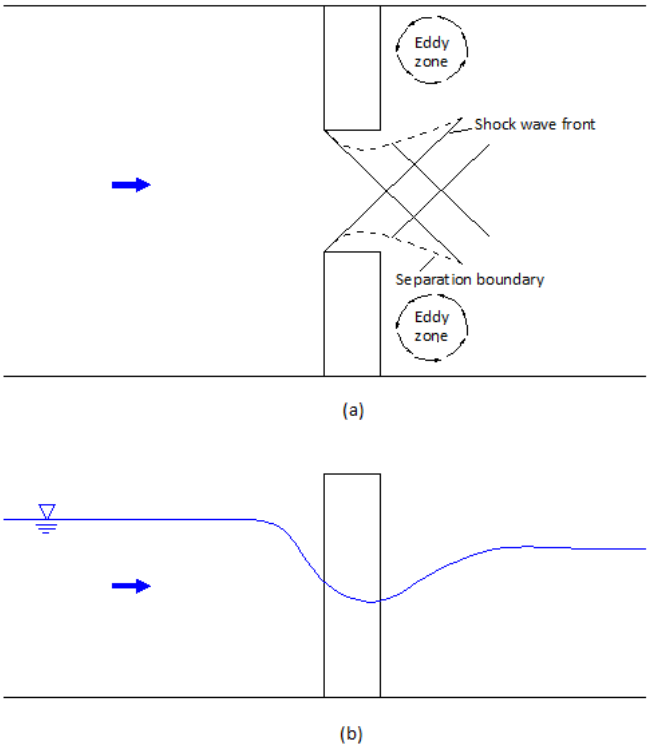


**Figure 3.1 Flow characteristics in the breach: (a) plan view; (b) side view**

Generally, the breach flow is a kind of broad-crested weir flow due to the lateral constraints from the breach channel and the embankment. The breach cross-section shape is usually idealized as being rectangular or trapezoidal, but it depends on the embankment materials as well as the hydraulic conditions during the breaching process, which shape it

will take. According to the shape of the cross-section, the weir can be simplified into a rectangular compound weir and/or a trapezoidal compound weir.

In this chapter, a series of experiments is described, which were conducted in a flume to simulate the hydraulic characteristics of the breach flow. The breaching process was simplified into five phases according to the breaching process observed in laboratory experiments, field measurements and prototype investigations. A discharge formula will be proposed based upon the experimental results.

## 3.2 Hydraulic Model of Breach flow

### 3.2.1 Weir Flow

A weir flow condition refers to the flow passing only through the breach. In order to compensate for actual flow conditions, such as energy losses, non-uniformity of velocity distribution, and streamline curvature in reality, a discharge coefficient, $C_d$ , is introduced to the weir flow formula.

According to the relationships between weir discharge and upstream water depth in the weir flow condition (Fig. 3.2), the discharge through a rectangular breach channel, as a critical discharge, can be expressed as

$$Q = C_d \frac{2}{3} b \left( \frac{2}{3} g \right)^{1/2} H_0^{3/2} \tag{3.1}$$

where $C_d$ is the weir discharge coefficient, $b$ is the width of the lower weir crest, $H_0$ is the upstream energy head above the weir.

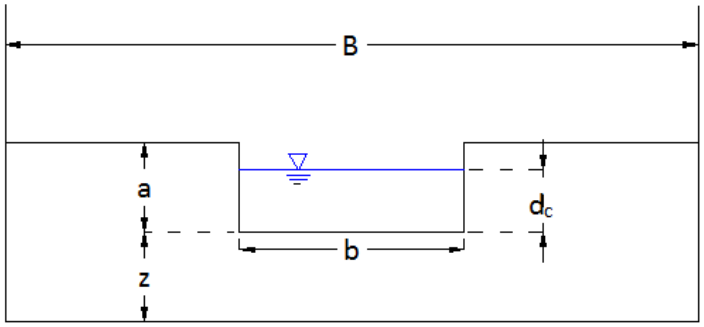


**Figure 3.2 Sketch of broad-crested weir with rectangular compound-section in weir flow condition**

Bos (1985) studied the flow over broad-crested weirs with a trapezoidal control section (Fig. 3.3) and the discharge formula in weir flow condition can be written as

$$Q = C_d \left( bd_c + md_c^2 \right) \left[ 2g \left( H_0 - d_c \right) \right]^{1/2} \tag{3.2}$$

where $m$ is the side slope, $d_c$ is the water depth above the weir that approximately equals $\frac{2}{3} H_0$ in the critical weir flow condition (Visser, 1998).

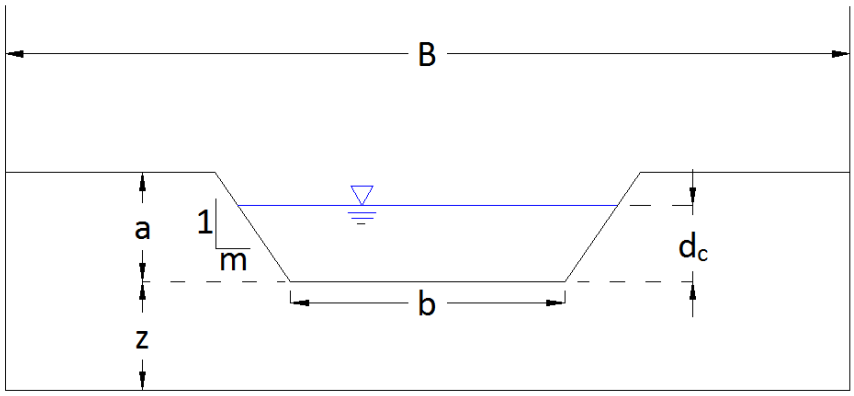


**Figure 3.3 Sketch of broad-crested weir with trapezoidal compound-section in weir flow condition**

### 3.2.2 Compound Weir Flow

In the beginning phase of the breach development process, the overtopping flow generally overtops the whole crest and cuts into a weak section of the embankment to form a trench, the overtopping flow becoming compound weir flow. In the compound weir condition, the breach flow goes through the rectangular compound cross section (Fig. 3.4), and the discharge can be expressed as a function of the upstream water depth (Gögüs *et al*., 2006)

$$Q = C_d \left(\frac{g}{B}\right)^{1/2} \left[ ba + B\left(\frac{2}{3}H_0 - \frac{ba}{3B} - \frac{2a}{3}\right)\right]^{3/2} \tag{3.3}$$

where $C_d$ is the discharge coefficient, $B$ is the width of the weir, $a$ is the breach depth, and $H_0$ is the energy height over the crest. In Eq. (3.3), the control section is considered as a combination of two rectangular sections over the weir crest and the breach part.

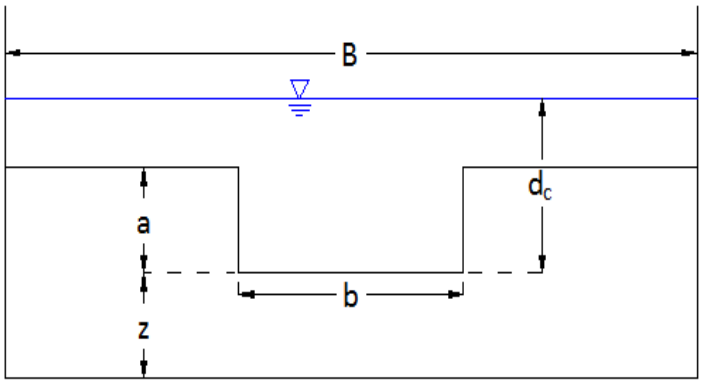


**Figure 3.4 Sketch of broad-crested weir with rectangular compound-section in compound weir condition**

When the breach channel has a trapezoidal shape (Fig. 3.5), the discharge can be calculated as

$$Q = C_d \left(\frac{g}{B}\right)^{1/2} \left[ ba + B\left(\frac{2}{3}H_0 - \frac{ba}{3B} - \frac{2a}{3}\right) + \frac{2}{3}a^2 m\right]^{3/2} \tag{3.4}$$

Eq. (3.4) can be simplified into Eq. (3.3) when the side breach slope *m* equals 0.

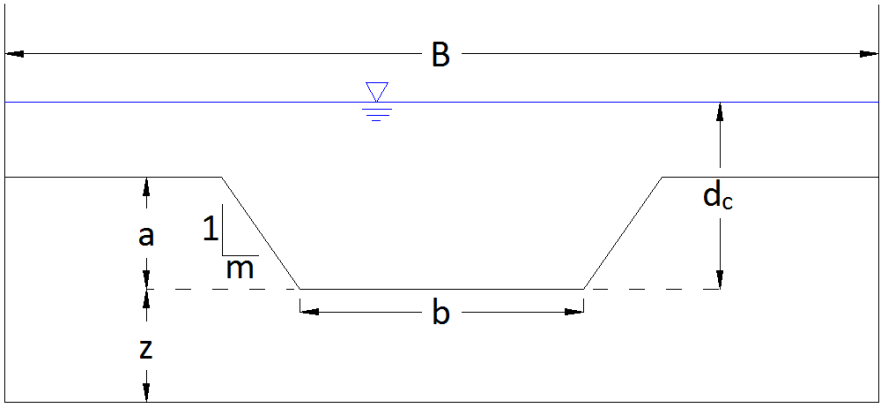


**Figure 3.5 Sketch of broad-crested weir with trapezoidal compound-section in compound weir condition**

### 3.2.3 Subcritical Breach Flow

As the breach develops, the breach flow goes from the critical regime into the subcritical regime. So the subcritical breach flow discharge (Visser, 1998) can be expressed as

$$Q = C_d \sqrt{2g} B (H_0 - H_d)^{1/2} H_d \tag{3.5}$$

where $H_d$ is the water level downstream of the breach above the weir.

## 3.3 Experiments of Breach Flow

### 3.3.1 Experimental setup

A weir with a fixed profile and a lateral contraction modelled the embankment breach in a laboratory flume. The experiment was expected to fulfil the objective of getting insight into the characteristics and behaviours of breach flow over broad-crested weirs with breaches of various geometries. In order to achieve this, several tests were conducted by varying the breach geometry.

The experiment was conducted in a flume with the dimension of 2 m × 20 m and a slope of 0 (see Fig. 3.6). The flume width is large enough to eliminate the effects of the side

walls. The flume bed was roughened by putting 5 to 6 mm of gravel onto the glass flume bottom.

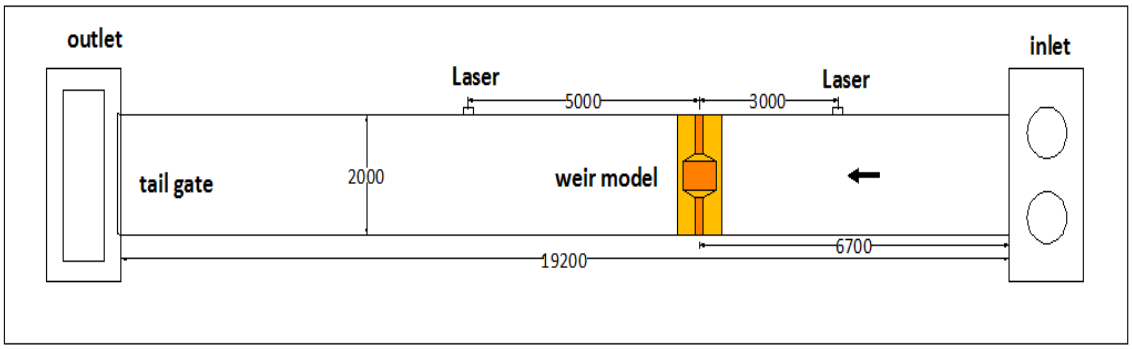


**Figure 3.6 Layout of the flume**

The embankment model was built with a crest length $L_w$ = 180 mm, a height $P$ = 130 mm and a slope of 1V:3H in both upstream and downstream, with the breach located in the middle of the weir crest (see Fig. 3.7).

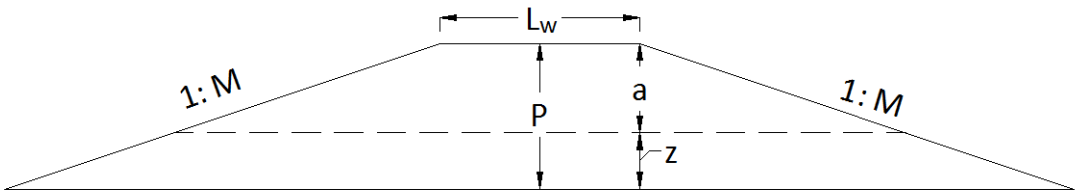


**Figure 3.7 Side view of designed weir**

The breach shape does not have a regular pattern during the embankment breaching process in the prototype, however, it is usually similar to rectangular or trapezoidal shapes. According to Visser's (1998) sandy dike breach growth stages, five cases with different cross sections were designed (Fig. 3.8). In the present study, the breach cross sections were idealized into a rectangular shape in the beginning phase of breach (Stage I), and into trapezoidal shapes in the other phases (Stage II, III, IV, V).

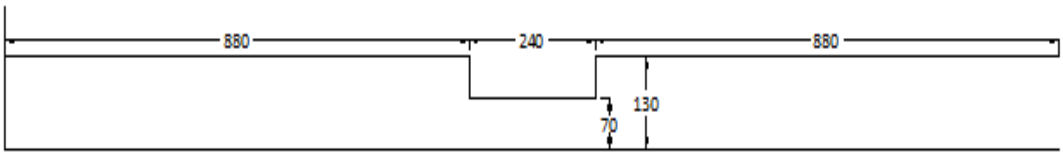


(a). Case 1

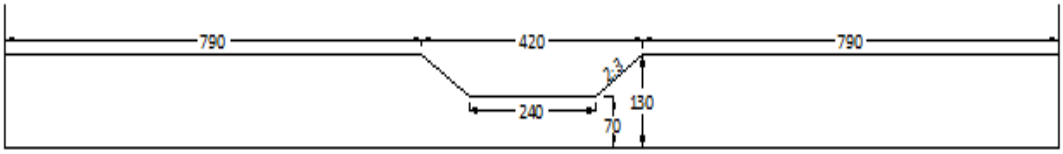


(b). Case 2

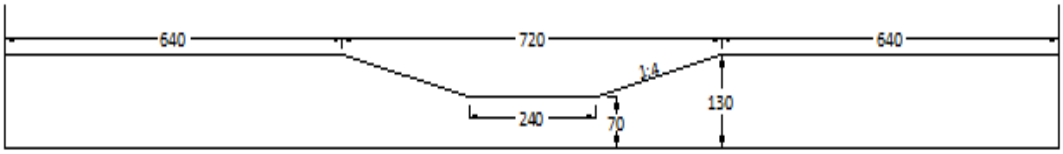


(c). Case 3

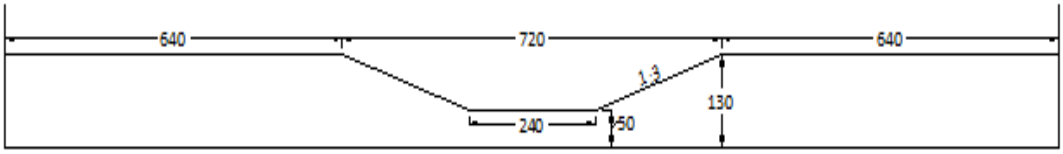


(d). Case 4

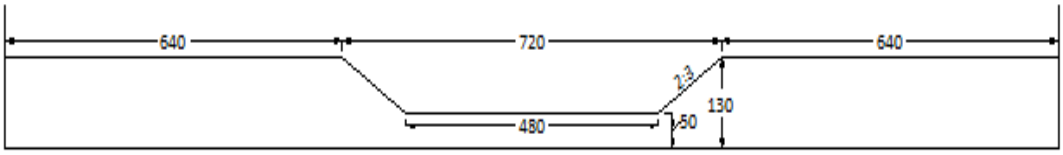


(e). Case 5

**Figure 3.8 Sketches of the breach cross-sections**

In order to simulate the breaching process, the model was designed into 4 stages (Table 3.1) to describe the breach widening and deepening processes in the embankment breaching development (Fig. 3.9).

**Table 3.1 Breaching stages in the test**

| *Stages* | *Constant Parameters* | *Tested Cases* |
|---|---|---|
| Top width widening | Breach height and bottom width | 1, 2, 3 |
| Breach deepening | Top and bottom width | 3, 4 |
| Widening and deepening | Breach slope | 2, 5 |
| Bottom width widening | Breach height, top width | 4, 5 |

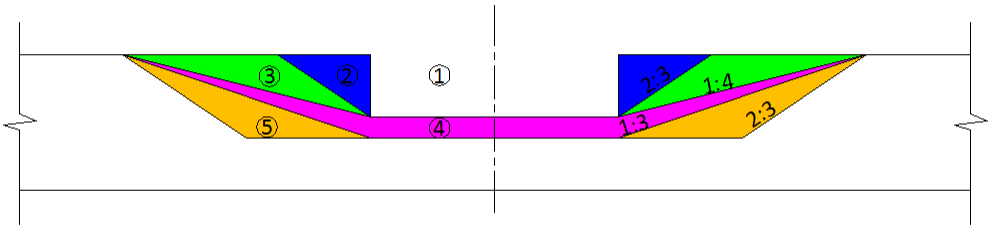


**Figure 3.9 Sketches of the breach test setup**

### 3.3.2 Measuring Procedure

In each run of the experiments, the inlet discharge was controlled by a Prosonic Flow Meter and the water levels upstream and downstream of the model were measured by the laser water level meters (see Fig. 3.6). An acoustic Doppler velocimeter (ADV) and point gauges were used to measure the point velocities and water levels in the breach channel area, respectively.

The upstream water level ($h$) for each case was controlled by the discharge, showing the different upstream water levels in Fig. 3.10. This figure shows that each breach has its own relationship of discharge and water level. As the water level upstream increases, the breach discharge increases. With the development of the breach, the discharge increases step by step at the same upstream water level. The downstream water level was controlled with a water level gauge near the tailgate, where the upstream discharge was kept constant.

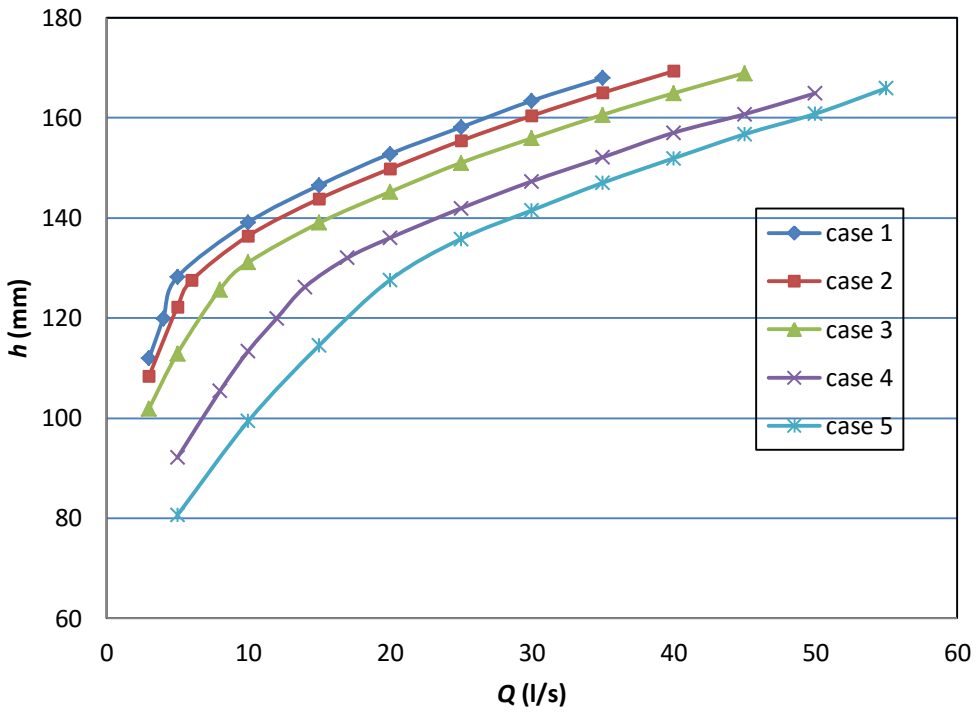


**Figure 3.10 Inlet relationships between discharge and water level for each breach case**

## 3.4 Analysis of Experimental Results

### 3.4.1 Water Level Distribution

In the compound weir flow condition, the water level remains almost constant, but it drops above the breach slopes and increases to a normal level in the middle of the breach (case 2, Fig. 3.11). The water level above the breach slope is lower than the water levels in the breach and on the dam crest, since there is much turbulence along the boundary of the breach. In the same boundary conditions, the total water level increases by 1 cm over the entire cross section if the upstream discharge increases from 30 l/s to 40 l/s.

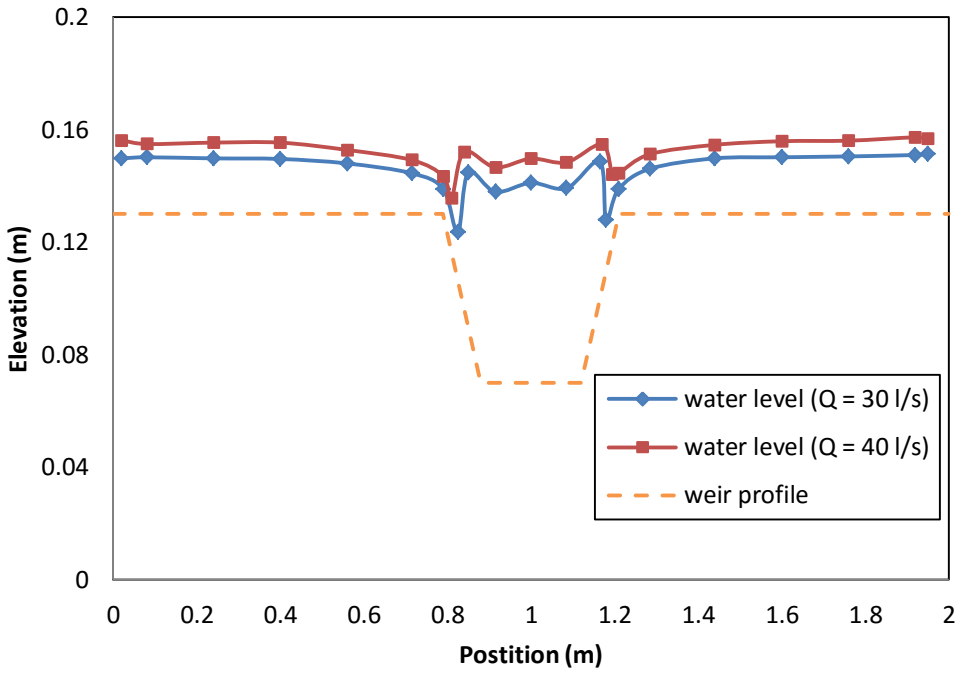


**Figure 3.11 Water levels in compound weir flow condition (case 2)**

As the breach develops, the breach shapes change to adjust to the breach flow. In compound weir flow conditions, two water level valleys move as the breach widens into the breach sides (see Fig. 3.12 and Fig. 3.13). The water level valleys above the breach slopes drop to the breach slopes as they move toward the sides, and the water level in the middle of the breach also drops down as the breach widens towards the two sides. The patterns in which the water level moves are almost the same, even though there are changes from rectangular to trapezoidal and back from trapezoidal to trapezoidal, but the two water level valleys drop more dramatically in the changing condition from trapezoidal to trapezoidal than in the change from rectangular to trapezoidal.

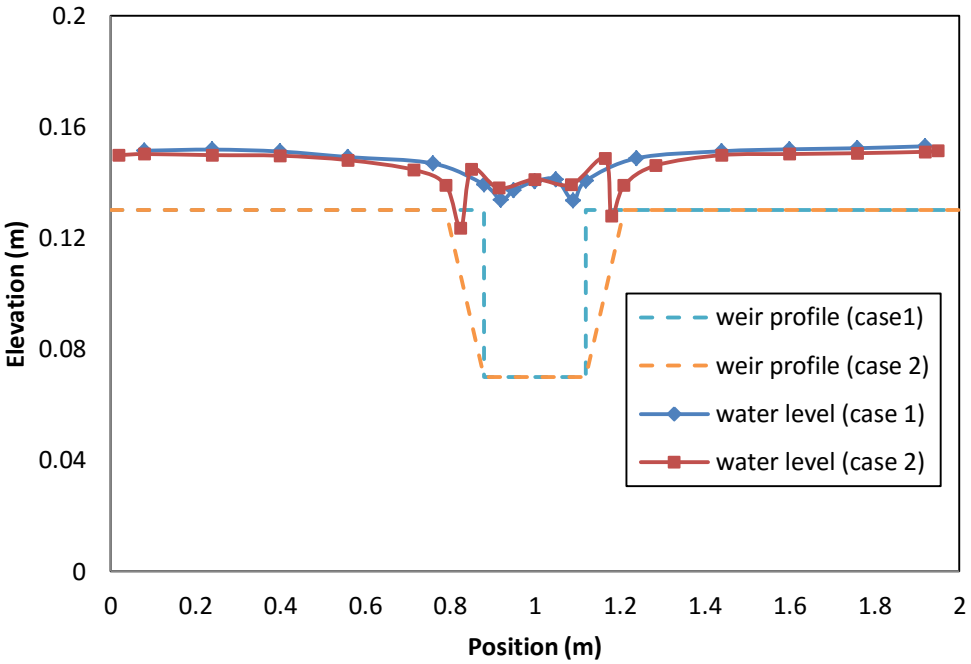


**Figure 3.12 Water levels in compound weir flow condition ($Q$ = 30 l/s)**

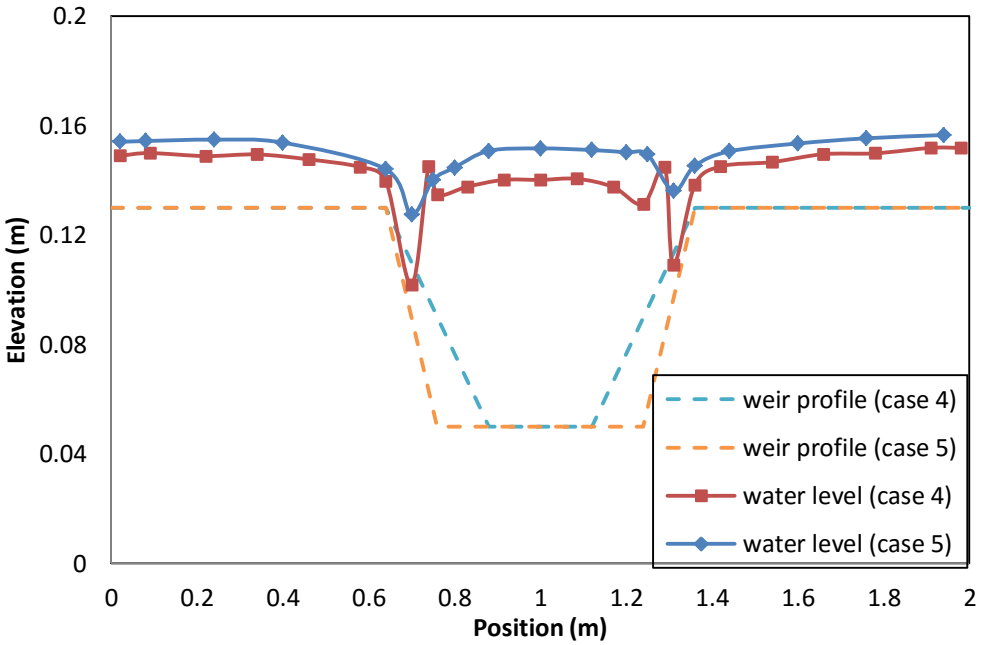


**Figure 3.13 Water level in compound weir flow condition ($Q$ = 50 l/s)**

In the weir flow condition, the lateral distribution in the water level is almost constant in the rectangular shaped breach channel (Fig. 3.14), but the water level decreases above the breach slopes in the trapezoidal shaped channel (Fig. 3.15). The water level has a peak point in the middle of the cross section and in the two valleys above the breach slopes, especially in the condition of trapezoidal breach shapes.

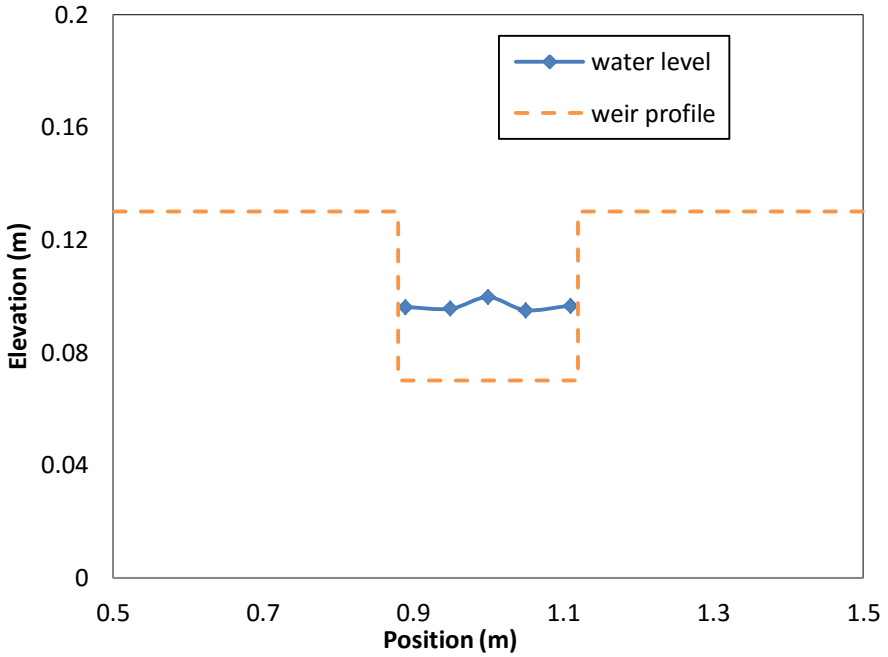


**Figure 3.14 Water level in weir flow condition ($Q$ = 4 l/s, case 1)**

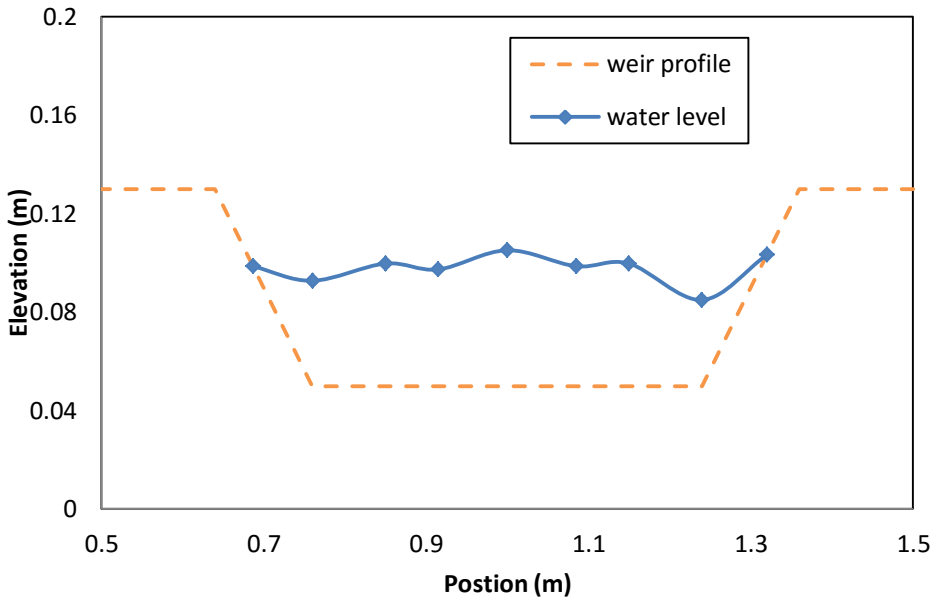


**Figure 3.15 Water level in weir flow condition ($Q$ = 20 l/s, case 5)**

### 3.4.2 Breach Discharge Distribution

It is of great interest to investigate how much water passes though the breach or over the crest, under compound weir flow conditions. It is important to simulate the breaching process and to estimate the discharge contributing to the breaching.

The discharge distributions predicted by Eq. (3.3) and Eq. (3.4) and the test results are plotted in Fig. 3.16, in which $Q_b$ is the discharge through the breach. The analytical predictions for cases 1 and 5 slightly underestimate the experimental data and the analytical predictions overestimate the experiment results in case 3 at low discharges. As for the other cases, the theory and laboratory results fit well. Overall, it can be concluded that the laboratory results for the five cases are in good agreement with the theoretical predictions. Based on the results of theory and experiment, it can be found that the breach discharges less compared to the total discharge with the increase of discharge for each case. It is reasonable that for the stage of high water the effect of the breach is reduced, and that at the same discharge, the larger the breach size is, the more water flows through the breach.

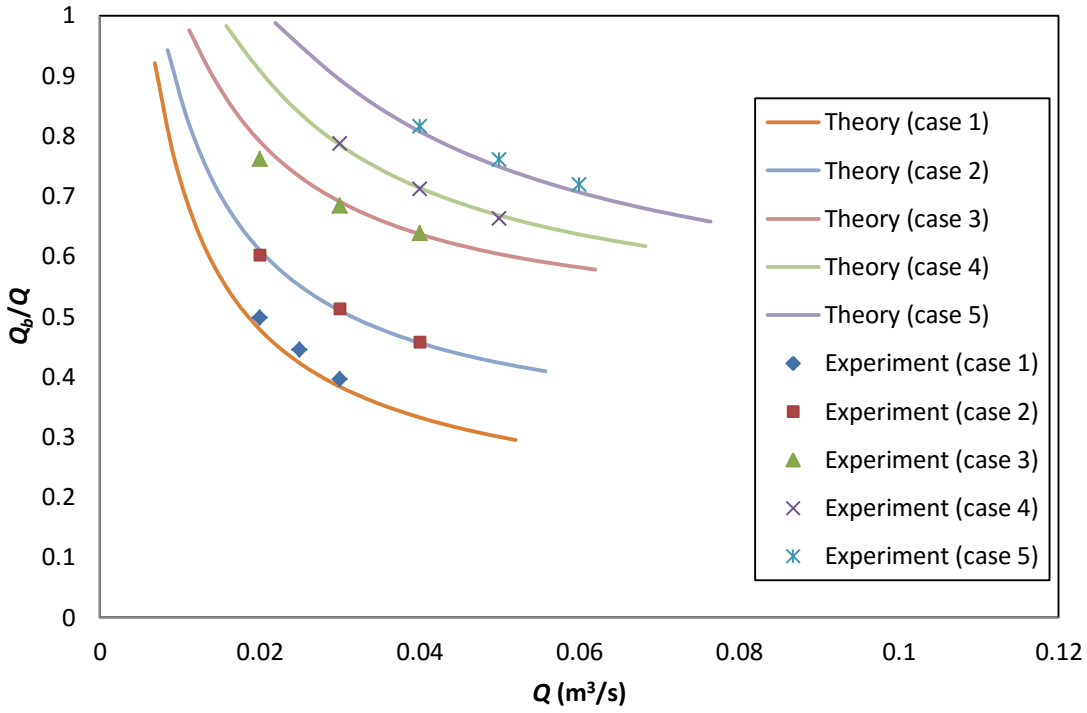


**Figure 3.16 Comparison of theory predictions and laboratory measurements on discharge distribution**

During the experiments, it was found that the flow in the breach first became subcritical, then the flow went over the crest and gradually the tail gate was raised from a low level. The discharge distributions in the situations of case 3, case 4 and case 5 are illustrated in Fig. 3.17. The differences in discharge distribution between perfect weir (critical discharge) and imperfect weir situations (subcritical discharge) in cases 3 and 4 are small, which indicates that the influence of a breach on the distribution is small. But in case 5, which has a larger breach, the difference is evident. Therefore the discharge distribution depends on the stages of breaching in the situation of subcritical flow in the breach and in the situation of critical flow over the crest.

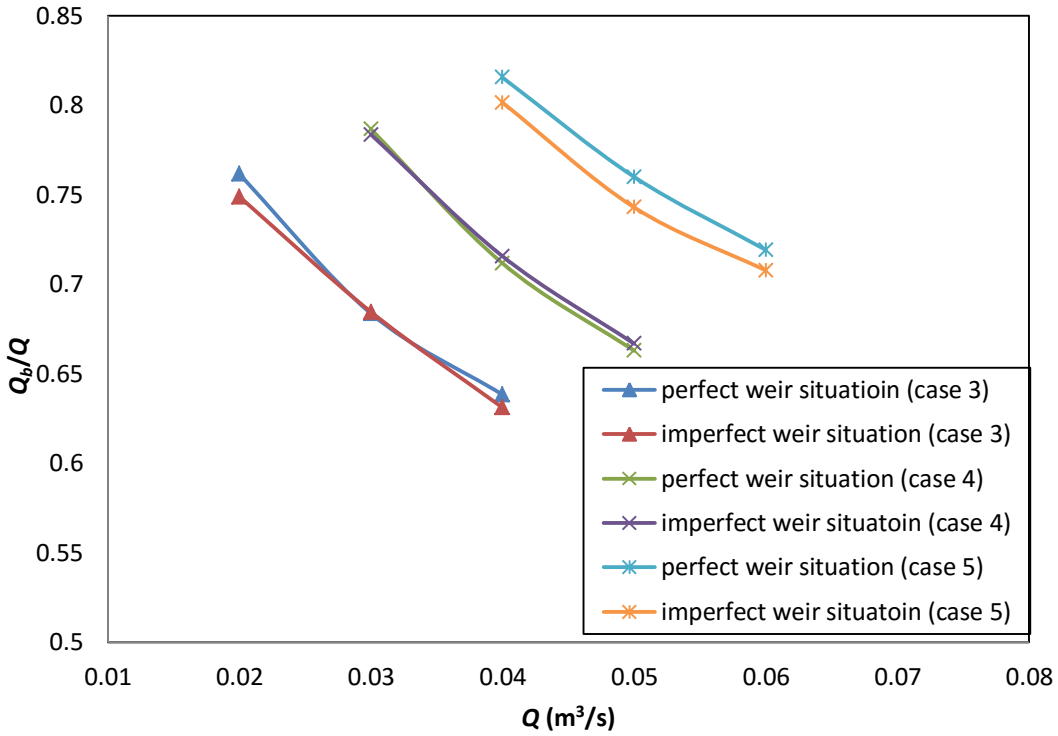


**Figure 3.17 Discharge distributions in the case of subcritical flow in the breach and critical flow over the crest**

### 3.4.3 Velocity Distribution

In the breaching process, the flow velocity plays an important role in the erosion and scour of the embankment, i.e. in the widening and the deepening process of the breach, and in the flood propagation process in downstream.

In the compound weir condition of case 1, the breach flow goes both through the breach channel and over the embankment crest. The flow velocity in the breach channel is higher than that over the crest (Fig. 3.18). In case 5 the velocity in the breach is much higher than over the crest and reaches its maximum value close to the side slopes (Fig. 3.19). There are two peak velocities close to the breach slopes due to the effects from flow turbulences in the breach. Between the two velocity peaks, the velocity reduces step by step, and reaches a minimum velocity in the middle of the breach. The flow (Fig. 3.20) is similar to the helicoidal flow in fluvial channels, and in the breaching process it can be called breach helicoidal flow. Additionally there is a triangular hydraulic jump at the toe of the breach, which is generated by the constrictions of the breach when the flow in the

breach transfers from supercritical flow into subcritical flow.

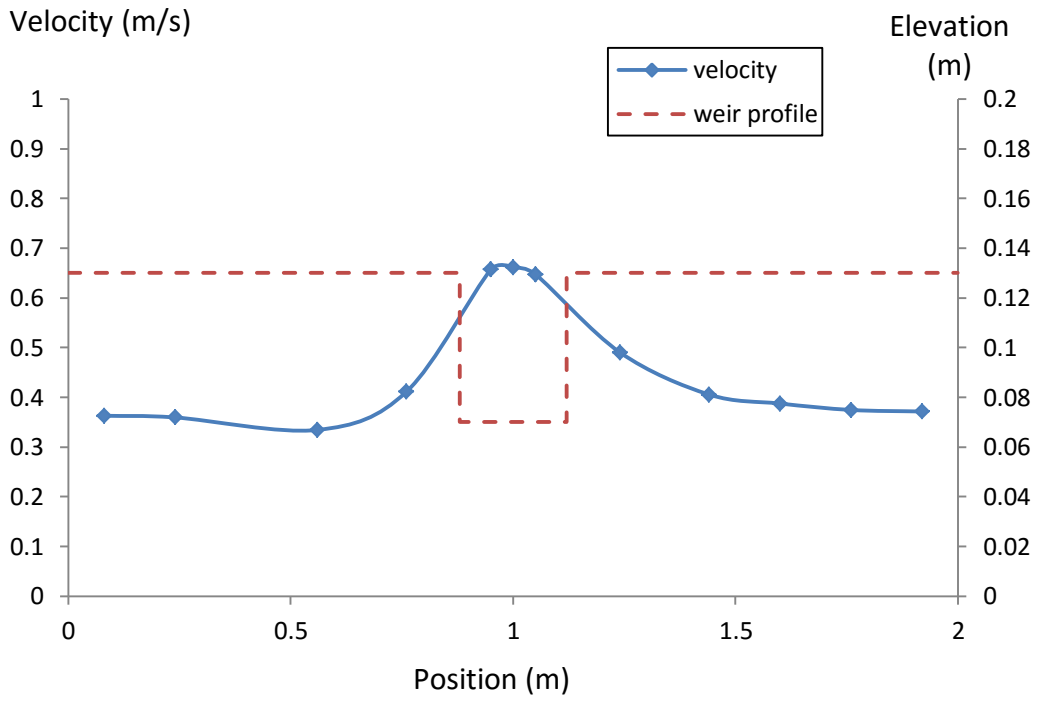


**Figure 3.18 Depth-averaged velocity distribution in breach cross section ($Q$ = 30 l/s, case 1)**

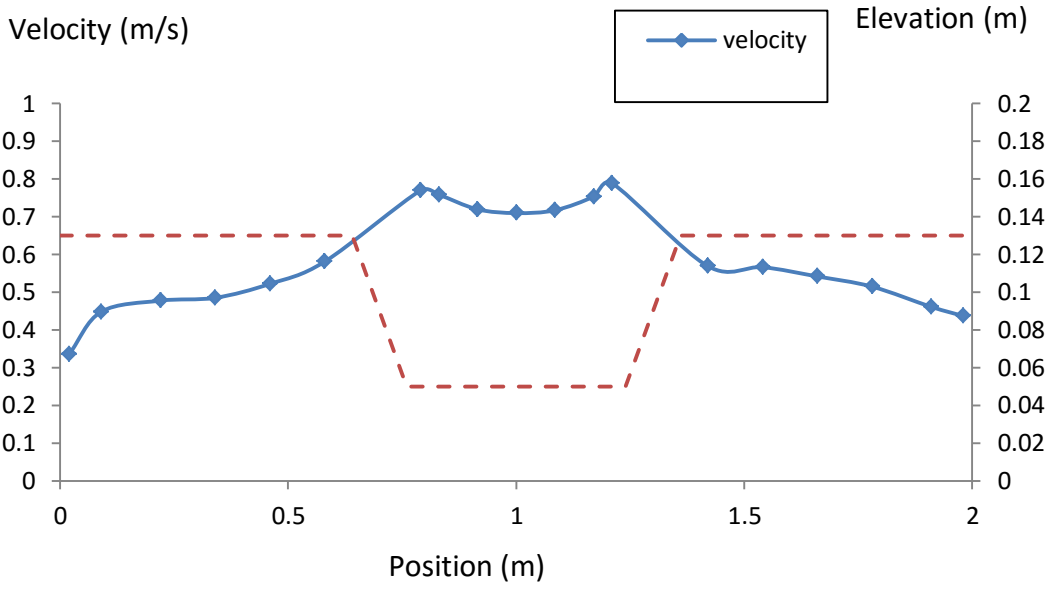


**Figure 3.19 Depth-averaged velocity distribution in breach cross section ($Q$ = 50 l/s, case 5)**

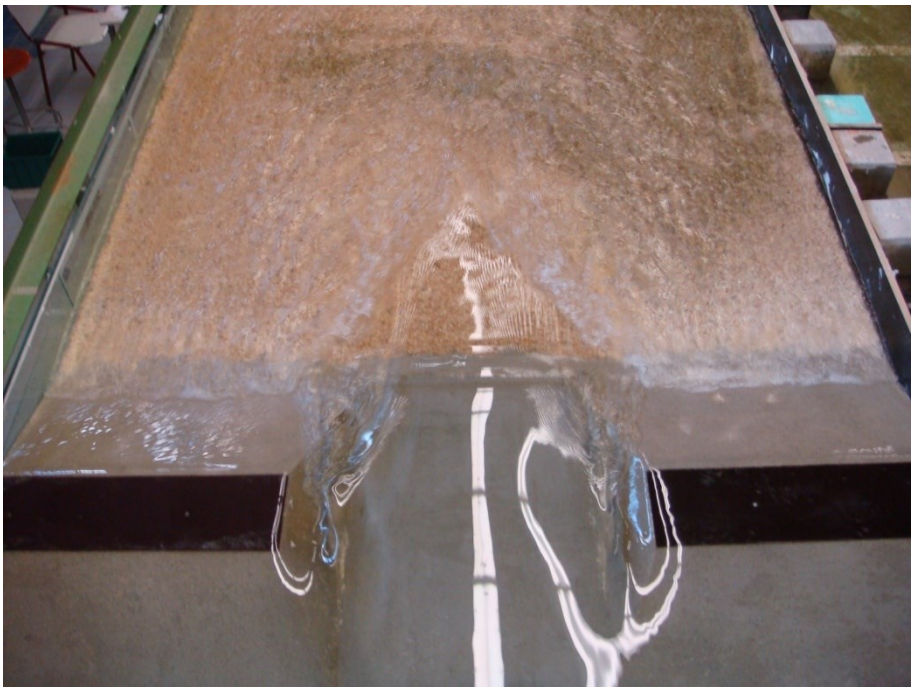

**Figure 3.20 Breach flow pattern in compound weir condition ($Q$ = 50 l/s, case 5)**

In the weir flow condition, the flow only passes through the breach. In Fig. 3.21, in the low discharge condition the flow close to the sides is a bit faster than the middle flow. Nevertheless, by increasing the discharge to the compound weir condition (Fig. 3.18), it can be seen that the velocity in the breach is much larger than the velocity on the crest, and, that the flow also speeds up in the near field of the breach. After a further increase of the incoming flow (Fig. 3.18), the maximum velocity in the breach does not change too much. However, the flow velocity over the crest largely increases. Hence, the difference in velocity between the breach and crest is smaller compared to that with a lower discharge.

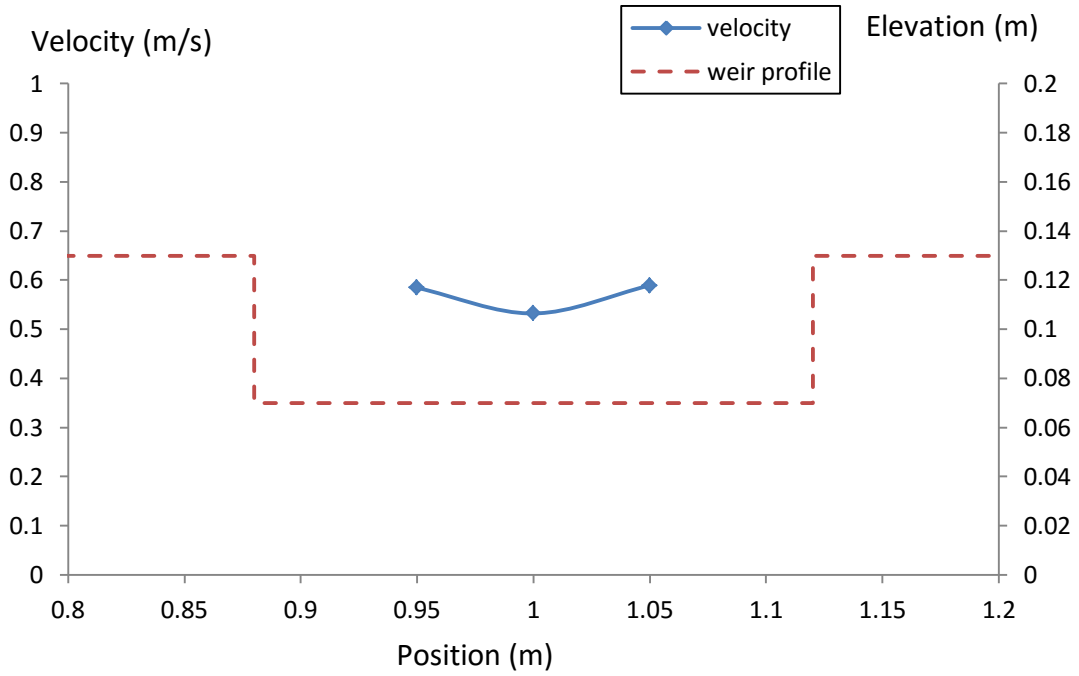


**Figure 3.21 Depth-averaged velocity distribution in breach cross section ($Q$ = 4 l/s, case 1)**

The minimum depth-averaged velocity is found in the middle of the trapezoidal cross section (Fig. 3.22). The helicoidal flow occurred in the breach channel in the weir flow condition (Fig. 3.23). When the flow in the breach transfers from supercritical flow into subcritical flow, there is a triangular hydraulic jump at the toe of the breach, which is generated by the constrictions of the breach. The eddy occurred in the downstream of the breach channel close to both sides of the channel bank downstream of the breach.

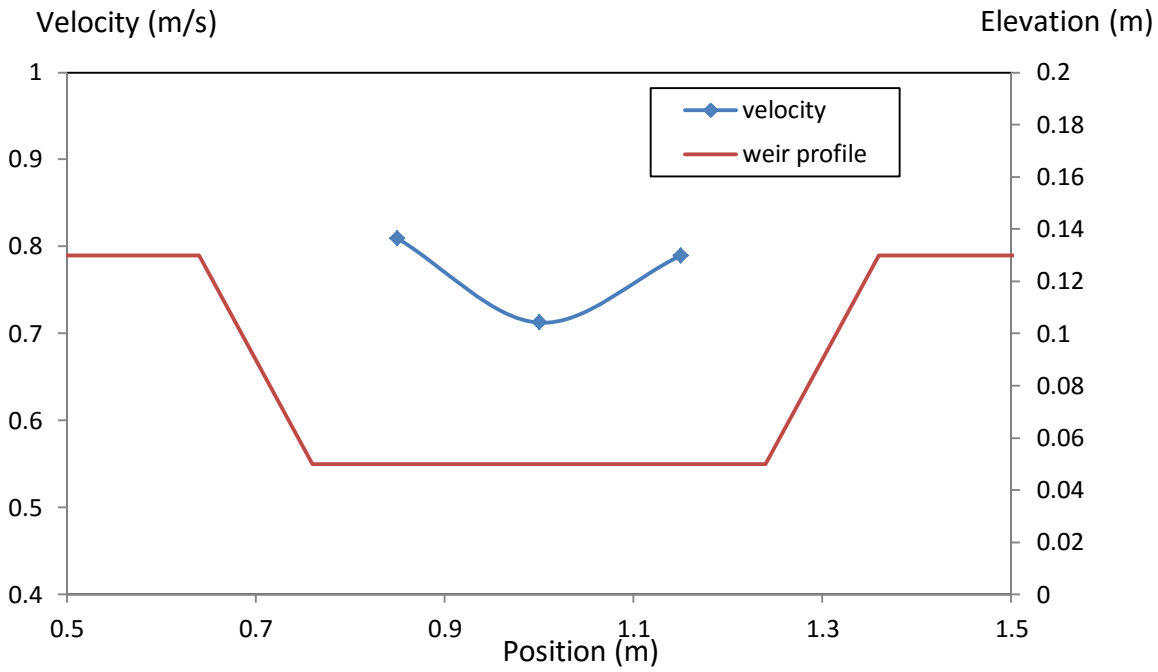


**Figure 3.22 Depth-averaged velocity distribution in breach cross section ($Q$ = 20 l/s, case 5)**

**Figure 3.23 Breach flow pattern in weir flow condition ($Q$ = 20 l/s, case 5)**

### 3.4.4 Breach Energy Loss

In the imperfect weir situation, the upstream flow conditions have a significant influence on the energy head loss for given downstream water levels. According to the energy conservation in the upstream and the momentum balance in the downstream, it can be found that the energy loss can be expressed as follows

$$\Delta H = h_1 + \frac{u_0^2}{2g} - h_2 - \frac{u_2^2}{2g} \tag{3.6}$$

where $h_1$ is the upstream water level, $h_2$ is the downstream water level, $u_0$ is the upstream flow velocity and $u_2$ is the downstream flow velocity.

By applying a high tail gate for each case and by gradually increasing the upstream discharge, the energy head loss against the upstream discharge is shown in Fig. 3.24. It can be seen from the plot that the energy head loss increases with the rising discharge and an obvious break in the slope can be observed for each curve. It is due to the discontinuity caused by the sudden change in the flow control section, which the flow starts to turn into a compound weir flow. According to the curves, the discontinuity occurs in case 1 to case 5, depending on the size of the breach. It is also worth mentioning that the energy loss increases linearly with the increase of discharge, but at different rates in the weir flow condition and in the compound weir flow condition, except for the transition from weir flow condition to compound weir flow condition . In weir flow conditions, the curve rate tends to decrease during the process of enlargement. However, the rate drops significantly in the compound weir flow condition and the curves seem to be parallel to each other. Therefore, the rate of energy loss should remain constant after the flow conducts itself as a compound weir flow.

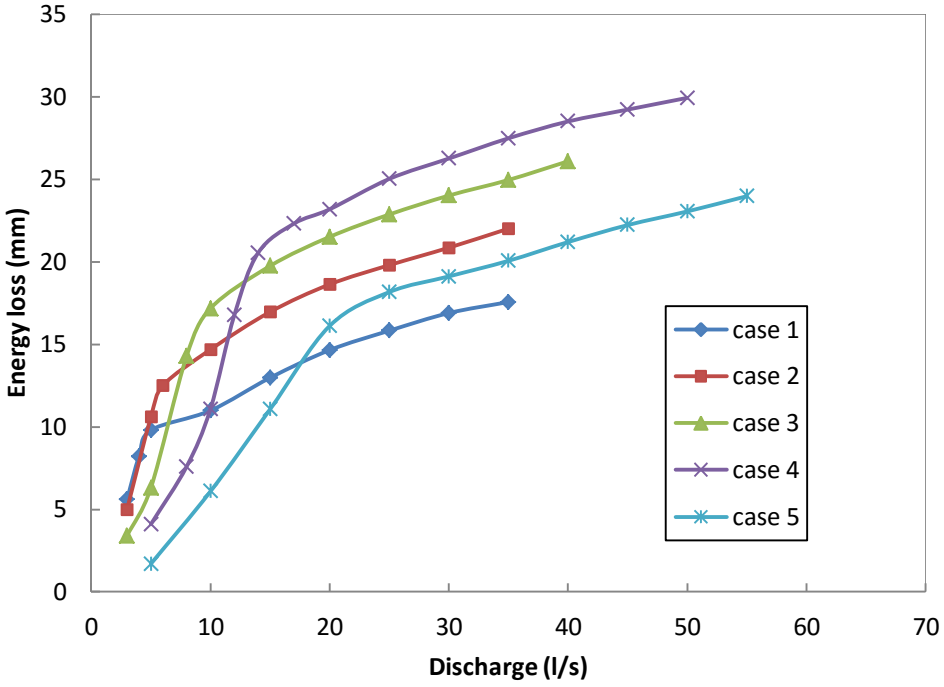


**Figure 3.24 Energy head loss versus upstream discharge at given tail heights**

As stated above, the energy head loss can be expressed as a function of the downstream water depth in a highly compound weir condition (Chow, 1959). In Fig. 3.25, the relation between energy loss and water level is presented. The curves are discontinuous due to the weir geometry and the transition zone can be clearly seen. In both the weir flow and the compound weir flow conditions, case 2 has more energy loss than case 1 at the same downstream water depth, which indicates that the top widening from rectangular into a trapezoidal breach shape results in a higher loss. It is the same among cases 2, 3 and 4. Therefore, the process of top widening and deepening of the breach dissipates more energy. Nevertheless, at the same downstream flow condition, the energy loss drops largely in case 5 after the widening of the breach bottom from case 4.

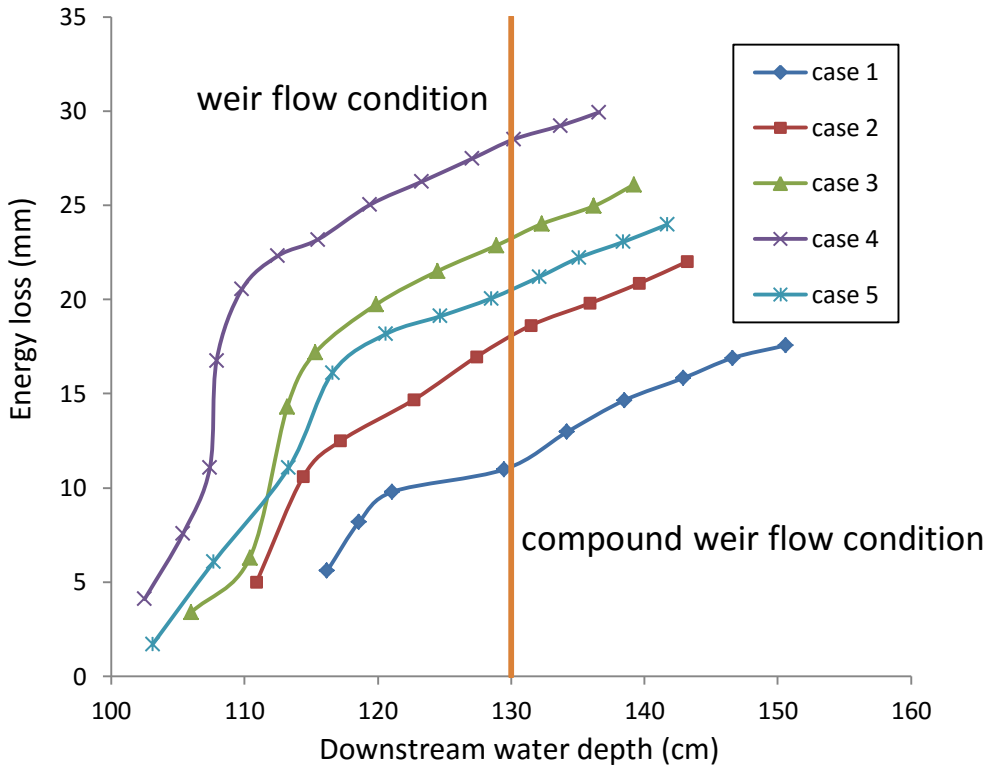


**Figure 3.25 Energy head loss versus downstream water depth**

### 3.4.5 Discharge Coefficient

As the discharge equations for the weir flow and the compound weir flow are both derived from the continuity equation and the energy conservation principle, the corresponding discharge coefficients based on them are comparable (Chow, 1959). The discharge coefficients from the weir flow condition and the compound weir flow condition in regard to the upstream energy head are plotted in Fig. 3.26. The discharge coefficients increase with the rising of the upstream energy head. In a weir flow, the values of cases 1 and 2 have a relatively larger increasing rate than the other three in which the changes are small. After overtopping, the discharge coefficients are closer to each other, increase at a decreasing rate and finally reach more or less constant values. The values for weir flow are more scattered due to the three-dimensional characteristics of the flow there, but the discharge coefficients are close to 0.85 in weir flow condition. However, the influence of the breach reduces in the compound weir flow condition.

There are different effects if a breach is caused by weir flow or compound flow. For instance, the discharge coefficient for case 5 is highest in a weir flow and lowest in a compound weir flow. Moreover, the difference is the smallest in the two flow conditions compared to the other cases. The difference is caused by the fact that the large size of breach is dominant to breach flow. Therefore, it is concluded that the values for the small-sized trapezoidal shape of breach, e.g. case 2, are of great difference under the weir flow conditions and compound weir flow conditions.

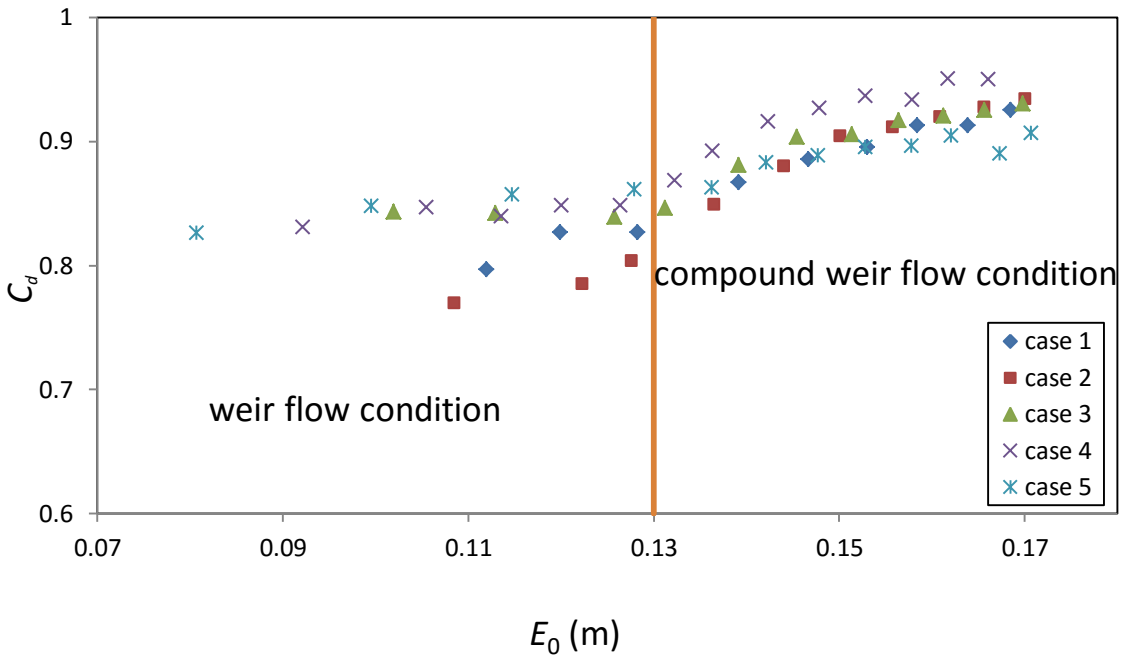


**Figure 3.26 Discharge coefficients versus upstream hydraulic energy $E_0$ from breach flow condition to compound weir flow condition**

## 3.5 Discussion

The breach flow plays an important role in the embankment breaching process since it determines the rate of erosion in the breach. During the breaching process, the flow overtops the whole of the embankment crest and generates the breach channel in the initial phase of breach development. As the breach develops, the breach flow only moves through the breach channel due to the decrease of the upstream water level. So the breach

flow can be classified as a weir flow and a compound weir flow, each of which has its own special characteristics.

In a meandering channel of a river, there is a type of helicoidal flow, which moves as a cork-screw in a meandering flow. It is a contributing factor to the formation of slip-off slopes and river cliffs in meandering sections of a river. The helicoidal motion of the flow aids the processes of hydraulic action and erosion on the outside of the meander, and sweeps sediment across the floor of the meander towards its inside. In a breach, there are two helicoidal flows (Fig. 3.27) above the two breach slopes, which are similar to the helicoidal flow in fluvial channels, and which can be called "breach helicoidal flow" in the breaching process. The helicoidal flow is generated by the roughness of the breach and by the constriction from the breach boundary, which triggers water levels to drop and flow velocity to jump above the breach slopes. The velocity distributions and the water level distribution are changed by the hydraulic boundary of the breach. The helicoidal flow accelerates the erosion of sediment, undermining the breach slopes at the toe and widening the breach in the lateral direction of the embankment.

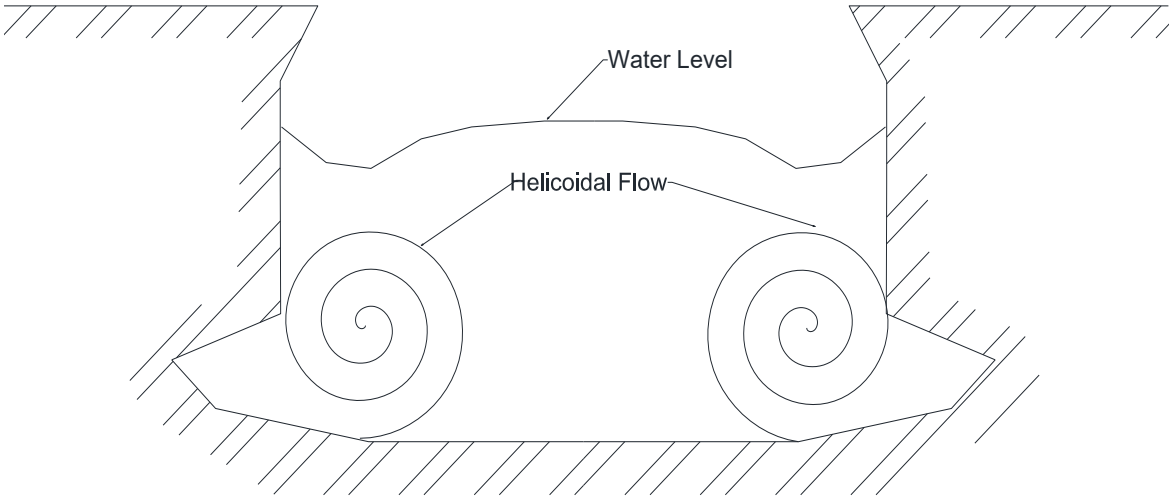


**Figure 3.27 General sketch helicoidal flows in breach channel (front view)**

The triangular hydraulic jump (see Fig. 3.23) happens when the breach flow changes from a supercritical flow into a subcritical flow, with a triangular critical area at the toe of the breach. The triangular hydraulic jump in the breaching process works as a driving force to the headcut erosion and the scour hole development at the toe of the embankment. According to the hydraulic energy loss in the breach, the discharge coefficients are analysed progressing from a weir flow condition to the compound weir condition, which can be very useful in the calculation of the breach discharge in the breach model.

In the past, many researchers (Visser, 1998; Zhu, 2006) have applied the weir formulae in the embankment breach models, however, there is not much known about breach flow hydraulics and universal weir discharge coefficients which can be used in breach models. This research first divided the breach growth process into 5 phases and used the fixed weir model to investigate the breach flow and the breach flow characteristics (e.g., helicoidal flow and triangular hydraulic jump) in different phases of breaching and that the discharge coefficient is about 0.85. The research results can contribute to the modelling of the breach flow.

# Chapter 4 Types of Erosion in Cohesive Embankment Breaching[2]

## 4.1 Introduction

Breach Erosion can be defined as a process and result of the interaction between breach flow and embankment material. Surface erosion starts in the initial phase of breach and causes the initial damage of the embankment. As the surface erosion develops completely, the headcut erosion leads the breaching process by cutting into the embankment slope and, finally, deepens the crest level. The breach side slopes are undermined by the lateral erosion and the breach widens in lateral direction due to the lateral collapses.

After the surface erosion in the beginning phase, the headcut typically starts at the toe of the embankment and then advances upslope until the crest of the embankment is reached. In some cases, a series of stair-step headcut forms on the downslope face of the embankment. The action is similar to that described by Dodge (1988) for model testing of embankment overtopping, which is related to headcut initiation and headcut advance by hydrodynamic and geotechnical mass wasting.

According to Fread (1988) and Zhu *et al*. (2004, 2005), headcut erosion plays a significant role in the breaching process in cohesive embankments. The mechanism of headcut erosion, however, still needs further understanding. A variety of breaching experiments and headcut experiments has been conducted in the recent past (Hanson *et al*., 2001, Zhu *et al*., 2004, Xie, 2013). Still, the mechanism of headcut erosion is insufficiently understood to describe the breaching process and, hence, to adequately simulate headcut erosion in a mathematical model.

[2] Most of this chapter is revised from "Gensheng Zhao, Paul J. Visser, Patrik Peeters, Johannes K. Vrijling. Headcut Migration Prediction of the Cohesive Embankment Breach. Engineering Geology, Volume164, 2013, Pages 18-25."

The lateral erosion widens the breach channel of the embankment. Due to the undermining induced by the helicoidal flow, the breach slopes lose their balance and collapse in the form of blocks. The lateral erosion stimulates the breaching process by increasing the area of the breach channel, which leads to a significant increase of the breach discharge. The lateral migration of the breach determines the breach embankment development in transversal direction and the change of discharge through the breach.

In this chapter, formula for the critical incipient shear strength and velocity are proposed according to the moment equilibrium method for undisturbed clay. A moment equilibrium-based model is proposed to simulate the headcut development and migration in a cohesive embankment breach due to breach flow, as well as the lateral development in the breaching process. The hypothesis is that the particle and mass is removed in the minimum moment on the breach slope. The lateral migration model is developed based on the same approach as the headcut migration model. The proposed models can be important and valuable to predict and simulate the breach erosion in cohesive embankments.

## 4.2 Incipient Motion of Clay

Erosion of clay is an important issue in many hydraulic engineering practices, in particular in the stability of clay coasts, the stability of clay layers in river beds and flood plains, scour around bridge piers, the stability of embankments, and the breach development in dikes and dams (Zhu *et al*., 2008; Knapen *et al*., 2007; Julian and Torres, 2006; Merritt *et al*., 2003; Gaskin *et al*., 2003). Clay offers resistance due to its strength, in particular its cohesive strength (Houwing, 1999; Houwing and Van Rijn, 1998; Panagiotopoulos *et al*., 1997). Resistance of clay to erosion depends on a large number of variables (Trenhaile, 2009; Rose *et al*., 2007), size and shape of the grains, grain size distribution (Fig. 4.1), mineral composition, chemical properties, water temperature, and the characteristics of the flow over the sediments. Undisturbed clay can have a density varying from about 1500 kg/m$^3$ to about 2000 kg/m$^3$, while the density of non-cohesive sediment in water is usually about 2000 kg/m$^3$.

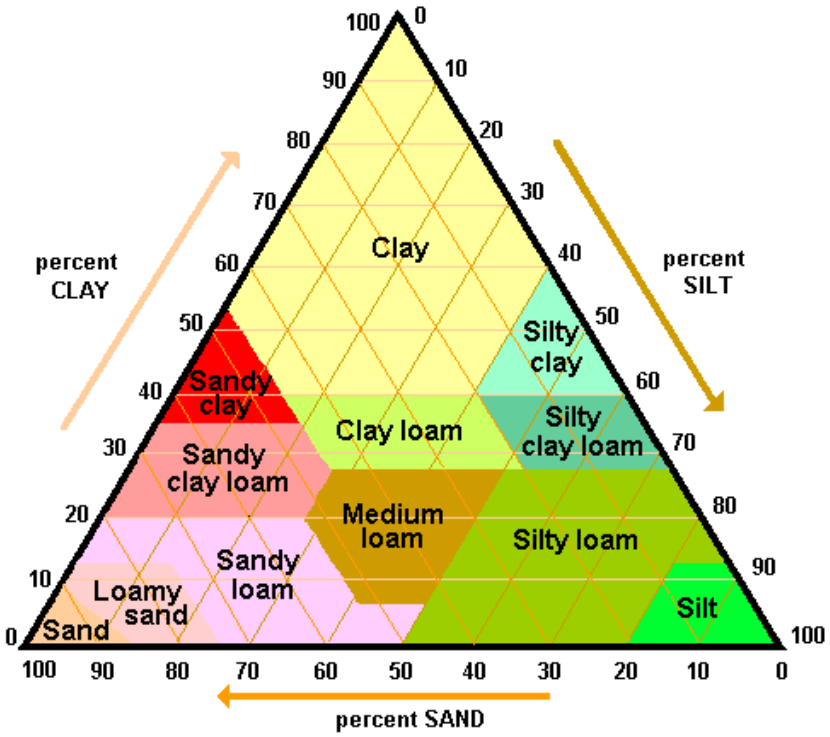


**Figure 4.1 Soil texture triangle-classification system based on grain size (USDA, 1987)**

In river mechanics, the Shields Curve and the Shields Parameter are used to describe the criteria of sediment incipient motion in the flow (Julian and Torres, 2006). The sediment is usually non-cohesive in rivers, e.g., sand and gravel, however, the embankments (e.g., levees, dams) are often constructed with cohesive materials (e.g., clay and sandy clay) (Fig. 4.2). In this section, incipient motion of cohesive materials is studied.

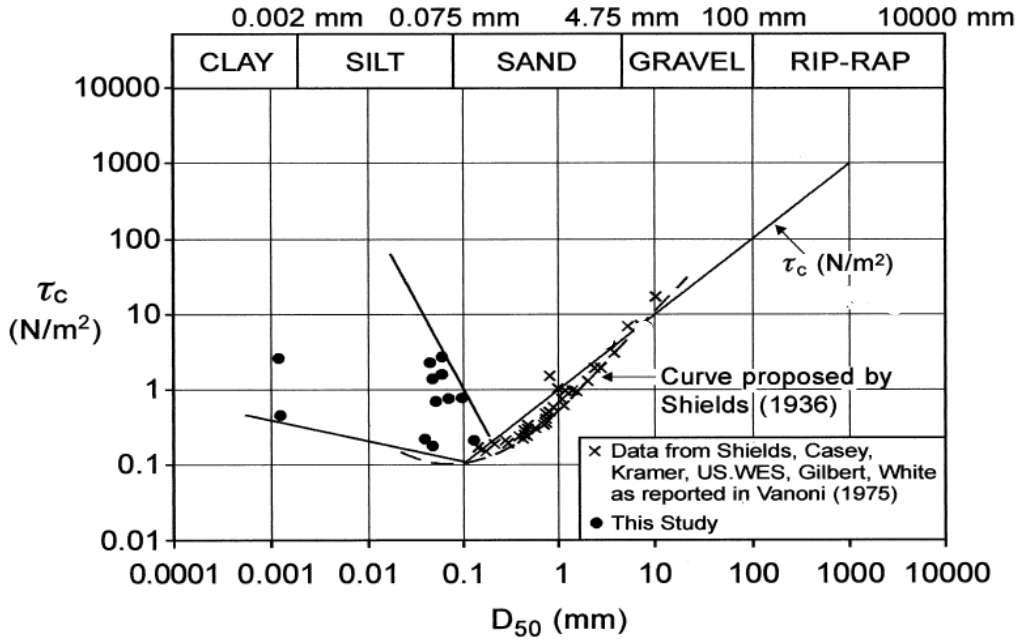


**Figure 4.2 Critical shear strength for sediment with different grain sizes**

### 4.2.1 Forces in Clay Incipient Motion

Due to the large number of variables involved, the identification and prediction of undisturbed clay erosion is a complicated problem in geomorphology and hydraulic engineering (Teisson *et al*., 1993). While the pickup of non-cohesive sediment through discrete particle entrainment may be quantified (if the flow velocities are not very large) by the magnitude of shear stress and particle size, undisturbed clay, in contrast, is eroded through entrainment of lumps of clay. The cohesive strength between and within aggregates causes the erosion to be complex (Zhao *et al*, 2010).

In the hydrostatic condition, there are electrical forces and forces at contacts between particles, and particle weight and water pressure around the particle (Fig. 4.3). In the flow condition, there is one more force, the flow shear stress around the particles (Fig. 4.4). In the large scale, the electrical forces and forces at contacts between particles can be supposed as the cohesive force between clay particles. So, there are at least four forces on a single clay particle in the non-hydrostatic condition, i.e. weight under water, cohesive forces, uplift force and drag force from the flow shear stress (Fig. 4.5).

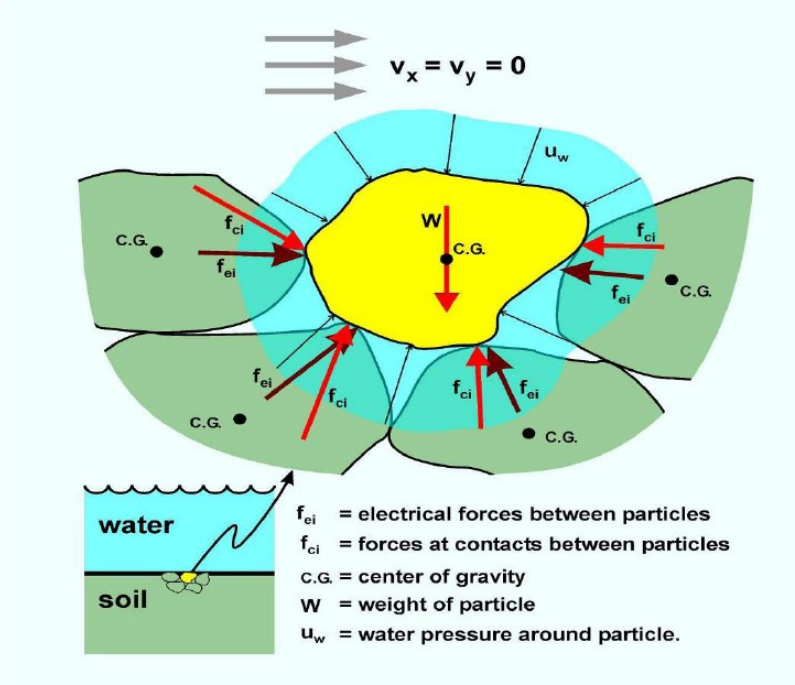


**Figure 4.3 Forces upon the soil particle in hydrostatic condition (after Briaud *et al*., 2008)**

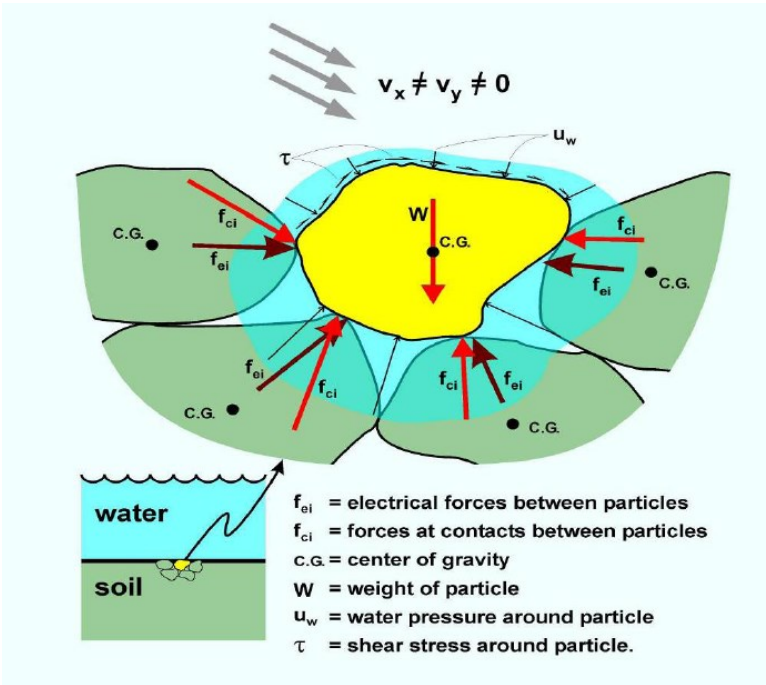


**Figure 4.4 Forces upon the soil particle in flow condition (after Briaud *et al*., 2008)**

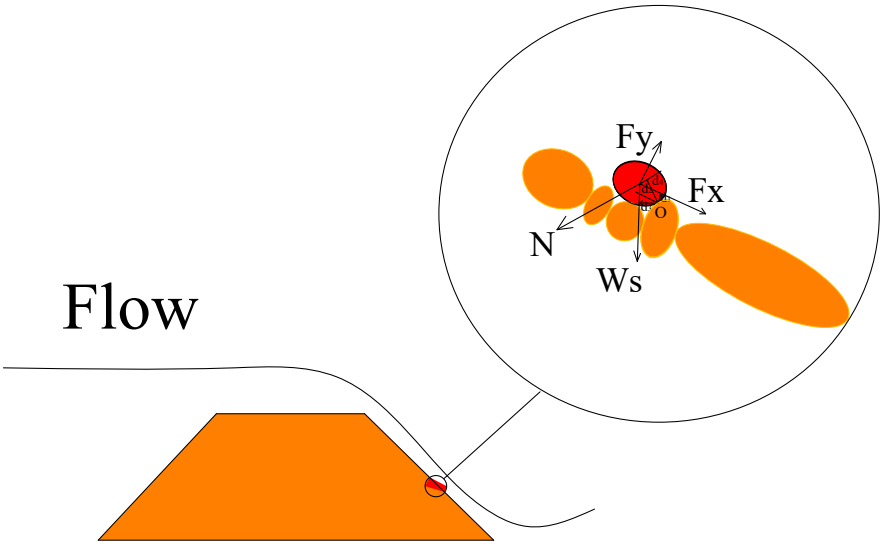


**Figure 4.5 Sketch of forces on a clay particle in breach flow**

(1) Weight

The weight of a single clay particle under water is

$$W_s = a_1 \frac{\pi}{6}(\rho_s - \rho) g D^3 \tag{4.1}$$

where $W_s$ is the weight of a clay particle under water, $a_1$ the shape coefficient, $\rho_s$ the density of clay, $\rho$ is the density of water, and $D$ the diameter of a clay particle.

(2) Shear strength among soil particles

The clay's resistance originates from the bonding forces, that hold clay particles together, and from other material in the soil matrix, such as organic matter, plant roots, and rock fragments. The various mechanical, adhesive, cohesive, and electrostatic bonding forces, acting on the undisturbed clay, increase its shear strength and these forces can generally be considered as cohesive forces as follows

$$\tau_f = \sigma \tan\varphi + c \tag{4.2}$$

where $\tau_f$ is the shear strength, $\sigma$ the normal stress on the clay particle, $\varphi$ the angle of friction, $c$ the cohesive force of clay particles, and

$$N = \frac{\pi D^2}{4} \tau_f \tag{4.3}$$

where $N$ is the shear strength force among clay particles.

Particle movement is supposed to occur when the instantaneous fluid force on a particle is larger than the instantaneous resisting force, which is related to the submerged particle weight and the friction coefficient (Fig. 4.3). The driving forces are also strongly related to the local near-bed velocities. In turbulent flow conditions the velocities are fluctuating in space and time. Considering the randomness of particle size, shape, position and turbulence, incipient motion is not merely a deterministic phenomenon, but also a stochastic process (Van Rijn, 1993 and 2006).

(3) Uplift force

The uplift force (Van Rijn, 1993) can be described with

$$F_y = a_2 c_y \frac{\pi D^2}{4} \frac{\rho U_d^2}{2} \tag{4.4}$$

where $F_y$ is the uplift force acting on the clay particle, $a_2$ the shape coefficient, $c_y$ the uplift force coefficient , $U_d$ the velocity over the clay particle.

(4) Drag force

Similarly, the drag force (Van Rijn, 1993) can be described as

$$F_x = a_3 c_x \frac{\pi D^2}{4} \frac{\rho U_d^2}{2} \tag{4.5}$$

where $F_x$ is the drag force on a clay particle, $a_3$ the shape coefficient, $c_x$ the drag force coefficient.

### 4.2.2 Incipient Motion due to Moment

Considering "$O$" as a fulcrum, according to the moment equilibrium, an equation can be written as

$$F_x d_1 + F_y d_2 - W_s d_3 - N d_4 \geq 0 \tag{4.6}$$

where $d_1$, $d_2$, $d_3$, $d_4$ are the vectors from position "O" for $F_x$, $F_y$, $W_s$, $N$, respectively (see Fig. 4.5).

So the incipient velocity of a clay particle can be written as

$$U_d = \sqrt{\frac{2}{(a_3 c_x d_1 + a_2 c_y d_2)\rho}\left[a_1 \frac{2}{3}(\rho_s - \rho) g D d_3 + \tau_f d_4\right]} \tag{4.7}$$

Supposing $C' = \dfrac{4 a_1 d_3}{3(a_3 c_x d_1 + a_2 c_y d_2)}$, $C = \dfrac{2 d_4}{(a_3 c_x d_1 + a_2 c_y d_2)}$, then

$$U_d = \sqrt{\frac{C'(\rho_s - \rho) g D + C'' \tau_f}{\rho}} \tag{4.8}$$

According to Prandtl Law (Chow, 1959), the velocity at any point in a turbulent flow over a solid surface can be given as

$$v = \frac{1}{\kappa}\sqrt{\frac{\tau_0}{\rho}} \ln \frac{y}{y_0} \tag{4.9}$$

where $v$ is the velocity over the clay particle, $\kappa$ ( Karman constant) is 0.40. Consequently,

$$\rho v^2 = \frac{1}{\kappa^2} \tau_0 \left( \ln \frac{y}{y_0} \right)^2 \tag{4.10}$$

Substituting Eq. (4.10) into Eq. (4.8) yields

$$\frac{1}{\kappa^2}\tau_0\left(\ln\frac{y}{y_0}\right)^2 = C'(\rho_s-\rho)gD + C\tau_f \tag{4.11}$$

$$\frac{\tau_0}{(\rho_s-\rho)gD} = \frac{\kappa^2}{\left(\ln\frac{y}{y_0}\right)^2}\left[C' + C''\frac{\tau_f}{(\rho_s-\rho)gD}\right] \tag{4.12}$$

where $y$ is equal to $0.5D$ under this hypothesis, $y_0$ depends on the characteristics of the clay particle surface, such as roughness, and on the boundary layer transition. In Eq. (4.12), the term C' is associated with particle weight and the term $C''\frac{\tau_f}{(\rho_s-\rho)gD}$ is associated with cohesive stress. In clay particle erosion, cohesion plays a far more important role than weight. If the weight is ignored, then Eq. (4.12) can be written as

$$\frac{\tau_{Cc}}{(\rho_s-\rho)gD} = \frac{\kappa^2}{\left(\ln\frac{y}{y_0}\right)^2}C\frac{\tau_f}{(\rho_s-\rho)gD} \tag{4.13}$$

where $\tau_{Cc}$ is critical shear stress of clay. Clay resists erosion well because of strong cohesive forces between particles. In the condition of high flow velocity, the clay is generally eroded in the format of blocks or lumps rather than individual particles (Peeters, *et al*., 2014; Zhao, *et al*., 2014). Therefore the hypothesis of clay incipient motion is, that the size of the incipient clay block is usually equivalent to the size of non-cohesive sediment, e.g., sand and gravel. The incipient of the clay block can be expressed by the non-cohesive sediment incipient formula as follows

$$\theta_c = \frac{\tau_c}{(\rho_s-\rho)gD_b} \tag{4.14}$$

where $\theta_c$ is the critical Shields parameter, $\tau_c$ is critical shear stress of the non-cohesive sediment particle's incipient with the same size, $D_b$ is the diameter of clay block. In the present study, the size of the clay block can be approximated as multiples of the clay median diameter (e.g., $10D_{50}$, $20D_{50}$, $30D_{50}$, etc.), which depends on the clay types (Peeters *et al*, 2014; Xie, 2013). Assuming the clay block equivalence to gravel sand, Eq. (4.10) and Eq. (4.14), Eq. (4.13) can be written as

$$\theta_{Cc} = \frac{\tau_{Cc}}{(\rho_s - \rho)gD_b} = C\frac{\tau_f}{\rho v^2}\theta_c \tag{4.15}$$

or

$$\tau_{Cc} = C\frac{\tau_c}{\rho v^2}\tau_f \tag{4.16}$$

where $\tau_{Cc}$ is the critical shear stress for the clay incipient motion, $\theta_{Cc}$ is the Shields Parameter for the clay. Eq. (15) and Eq. (16) reflect the clay incipient motion based on the physical mechanics of flow and clay soil. They have the same formats as the clay incipient motion empirical formula of van Rijn (2006).

## 4.3 Headcut Migration Model

Robinson and Hanson (1995), Hanson (1996), and Hanson *et al*. (2001) proposed a stress balanced headcut migration model. But headcut migration is a three-dimensional phenomenon that depends on the embankment geometry, the hydraulic load and soil properties, and it is not solely a static problem only concerned with the balance of forces. Moreover, the headcut migration is a dynamic process involving variation of flow and geometry. Thus, the moment equilibrium model is proposed to describe the dynamic process of the headcut migration using the new clay incipient method (Eq. (4.15) and Eq. (4.16)).

### 4.3.1 Erosion Rate

In the breach development process, the maximum time-averaged hydraulic shear stresses in the vertical and horizontal direction are used to predict the rate of erosion. Based on the dimensionless analysis, the erosion rate can be expressed with an excess stress equation (Hanson *et al*., 2001)

$$\varepsilon = \zeta(\tau_e - \tau_{Cc})^n \tag{4.17}$$

where $\varepsilon$ is erosion rate, $\zeta$ is erodibility coefficient, $\tau_e$ is effective stress, $n$ is an empirical parameter, which equals 1.0.

### 4.3.2 Headcut Migration due to Moment

The schematic in Fig. 4.6 illustrates the forces on the eroded block during headcut migration as water weight $G_0$, flow stress $F$ and tail water pressure $P$ from water, as well as the block weight $G$ and embankment cohesion force $N_1$ and $N_2$. $N_1$ and $N_2$, are not tensile strength, but form the cohesive forces among the soil particles.

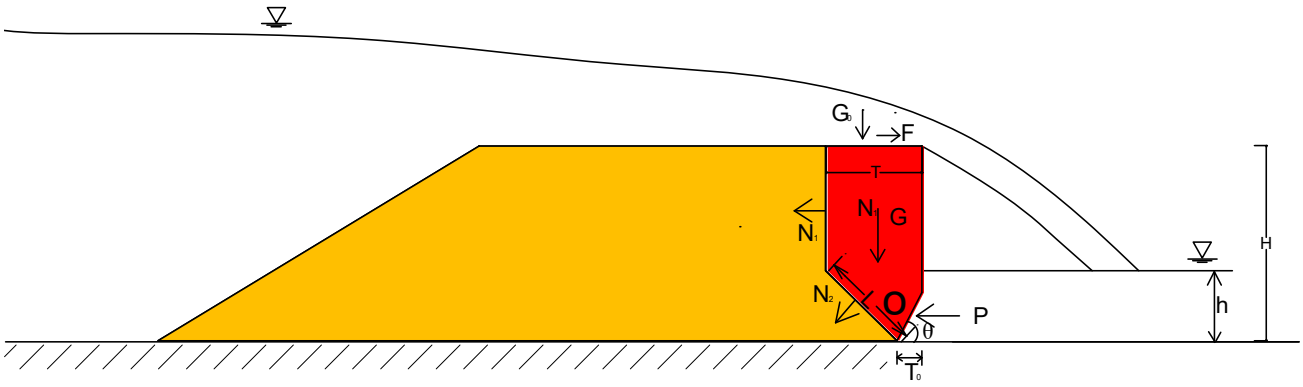


**Figure 4.6 Sketch of headcut migration**

According to the moment principle, a moment equation can be obtained if "O" is seen as the fulcrum:

$$M = F \cdot d_5 - G_0 \cdot d_6 - N_1 \cdot d_7 - N_2 \cdot d_8 + G \cdot d_9 - P \cdot d_{10} \tag{4.18}$$

where $d_{(s)}$ with subscripts are the vectors from point "O" to the position where quantity forces are applied and can be expressed as follows:

$$d_5 = H \tag{4.19}$$

$$d_6 = 0.5T - T_0 \tag{4.20}$$

$$d_7 = 0.5(H + L\sin\theta) \tag{4.21}$$

$$d_8 = 0.5L \tag{4.22}$$

$$d_9 = H\frac{(3H - L\sin\theta)}{3(2H - L\sin\theta)} - T_0 \tag{4.23}$$

$$d_{10} = \frac{1}{3}h \tag{4.24}$$

where $T$ is the headcut distance, $T_0$ is the heacut toe erosion distance required to cause the failure, $L$ is the length of the failure plane, $\theta$ is the failure plane angle, $H$ is the embankment height, $h$ is the tail water depth.

From the relationship of $T, T_0$ and $L$ :

$$T = T_0 + L\sin\theta \tag{4.25}$$

Eq. (4.21), Eq. (4.22) and Eq. (4.23) can be rewritten as

$$d_7 = 0.5(H + T - T_0) \tag{4.26}$$

$$d_8 = 0.5(T - T_0)/\sin\theta \tag{4.27}$$

$$d_9 = H\frac{(3H - T + T_0)}{3(2H - T + T_0)} - T_0 \tag{4.28}$$

In Eq. (4.15), if the $d_5$, $d_6$, $d_7$, $d_8$, $d_9$, $d_{10}$ are substituted by Eq. (4.19), Eq. (4.20), Eq. (4.26), Eq. (4.27), Eq. (4.28), Eq. (24), Eq. (4.15) can be rewritten as a function as follows

$$\begin{aligned} M &= F(T, T_o, G_0, N_1, N_2, G, P) \\ &= \mathrm{F}\cdot\mathrm{H} - G_0\cdot(0.5T - T_0) - N_1\cdot 0.5(H + T - T_0) \\ &- \mathrm{N}_2\cdot\left[0.5(T - T_0)/\sin\theta\right] + G\cdot\left[H\frac{(3H - T + T_0)}{3(2H - T + T_0)} - T_0\right] \\ &- P\cdot\frac{1}{3}h \end{aligned} \tag{4.29}$$

In the headcut developing process, water weight $G_0$, flow stress $F$, tail water pressure $P$, headcut block weight $G$ and embankment cohesion forces $N_1$ and $N_2$ are generally kept as

constant values. Therefore Eq. (4.29) can be simplified into a generally simple format as follows

$$M = f(T, T_o) \tag{4.30}$$

The moment "M" should be larger than 0 if the block can be moved, therefore if the headcut migration occurs:

$$M \geq 0 \tag{4.31}$$

The relationship Eq. (4.30) between $T_0$ and $T$ can be given as

$$T_0 = f(T) \tag{4.32}$$

The headcut migration rate can be described with headcut movement $T$ and the time interval as follows (Hanson *et al*., 2001):

$$\frac{dx}{dt} = \frac{T}{t} \tag{4.33}$$

As the headcut develops, erosion occurs at the toe of the headcut. The embankment block fails and the headcut advances when the vertical erosion exceeds a certain amount and when the base of the embankment cannot ensure the potential failure block. The time interval of failures is monitored by the erodibility and strength of the embankment. It is based on the erosion on the vertical toe of the headcut face, which causes the headcut to become unstable. Therefore, the time interval can be expressed via Eq. (4.17):

$$t = \frac{T_0}{\varepsilon} \tag{4.34}$$

The headcut migration rate can be expressed by Eq. (4.30), Eq. (4.31) and Eq. (4.32):

$$\frac{dx}{dt} = \frac{T}{f(T)}\varepsilon \tag{4.35}$$

Based on the moment balanced method, the headcut migration model can be expressed by Eq. (4.35) which is different from the stress balanced model (Hanson *et al*., 2001). Eq. (4.32) can be iterated and gets a deterministic T and $f(T)$. The headcut migration process will stop when the toe erosion rate $\varepsilon = 0$, which well fits the headcut development in the prototype.

Headcut migration is a hydrodynamic process in the cohesive embankment breach. The model is based on the moment equilibrium principle, the clay incipient formulae (Eq. (4.15) and Eq. (4.16)), as well as on the erosion rate with the excess stress method (Eq. (4.17)). The new headcut migration model is developed to predict the key progress of the cohesive embankment breaching.

## 4.4 Lateral Erosion

The lateral erosion (see Fig. 4.7) starts to fully affect the breach, when the headcut erosion goes through the embankment crest starting from the toe of the embankment (Peeters, *et al*., 2014; Zhao, *et al*., 2014). The material blocks fall due to the undermining erosion at the toe of the breach side slope. As a result, the peak breach outflow can occur during the lateral erosion phase, as the breach opening continues to enlarge under a relatively constant reservoir head. For this reason, lateral erosion is an important factor that should be included in the breach simulation model.

The schematic in Fig. 4.7 illustrates the forces on the eroded block during lateral migration as tail water pressure $P$ from water, the block weight $G$ and embankment cohesion force $N_1$ and $N_2$ , the failure plane angle $\theta$.

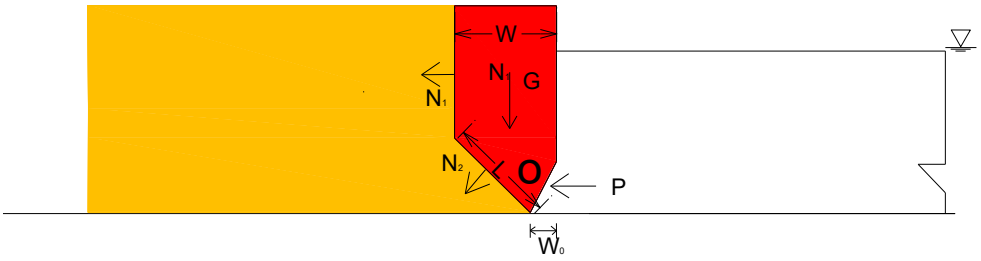


**Figure 4.7 Sketch of lateral migration of embankment breaching**

According to the moment principle, a moment equation can be obtained if $O$ is seen as the fulcrum:

$$M = G \cdot d_{11} - N_1 \cdot d_{12} - N_2 \cdot d_{13} - P \cdot d_{14} \tag{4.36}$$

where $d_{(s)}$ with subscripts are the vectors from point O to the position, where quantified forces are applied and can be expressed as follows:

$$d_{11} = H \frac{(3H - L\sin\theta)}{3(2H - L\sin\theta)} - W_0 \tag{4.37}$$

$$d_{12} = 0.5(H + L\sin\theta) \tag{4.38}$$

$$d_{13} = 0.5L \tag{4.39}$$

$$d_{14} = \frac{1}{3}h \tag{4.40}$$

where $W_0$ is the breach slope toe erosion required to cause the failure, $L$ is the length of the failure plane, $\theta$ is the failure plane angle, $H$ is the embankment height, $h$ is the breach channel water depth.

From the relationship of $W$, $W_0$ and $L$:

$$W = W_0 + L\sin\theta \tag{4.41}$$

Eq. (4.37), Eq. (4.38) and Eq. (4.39) can be rewritten as

$$d_{11} = 0.5(H + W - W_0) \tag{4.42}$$

$$d_{12} = 0.5(W - W_0)/\sin\theta$$

(4.43)

$$d_{13} = H \frac{(3H - W + W_0)}{3(2H - W + W_0)} - W_0 \tag{4.44}$$

In Eq. (4.36), if the $d_{11}$, $d_{12}$, $d_{13}$, $d_{14}$ are substituted by Eq. (4.37), Eq. (4.42), Eq. (4.43), Eq. (4.44), the lateral block moment equilibrium Eq. (4.36) can be rewritten as a function as follows

$$\begin{aligned} M &= F(W, W_o, N_1, N_2, G, P) \\ &= \mathrm{G}\cdot\left[0.5(H + W - W_0)\right] \\ &- N_1 \cdot \left[0.5(W - W_0)/\sin\theta\right] \\ &- N_2 \cdot \left[ H \frac{(3H - W + W_0)}{3(2H - W + W_0)} - W_0 \right] - P \cdot \frac{1}{3}h \end{aligned} \tag{4.45}$$

In the lateral erosion developing process, tail water pressure $P$, embankment block weight $G$ and embankment cohesion force $N_1$ and $N_2$ are generally kept as constant values. Therefore Eq. (4.45) can be simplified into

$$M = f(W, W_o) \tag{4.46}$$

The moment "m" should be larger than 0 if the block can be moved, therefore if the block failure occurs:

$$m \geq 0 \tag{4.47}$$

The relationship between $W_0$ and $W$ can be given as

$$W_0 = f(W) \tag{4.48}$$

The lateral migration rate can be described with Lateral movement $W$ and the time interval $t$ as follows:

$$\frac{dy}{dt} = \frac{W}{t} \tag{4.49}$$

As the lateral movement develops, erosion occurs at the toe of the breach slope. The embankment block fails when the vertical erosion $W_0$ exceeds a certain amount and the base of the embankment cannot ensure the potential failure block. The time interval of failures is monitored by the erodibility and strength of the embankment. It is based on the erosion on the vertical toe of the breach slope, which causes the breach slope to become unstable. Therefore, the time interval can be expressed via Eq. (4.17):

$$t = \frac{W_0}{\varepsilon} \tag{4.50}$$

Lateral migration rate can be expressed by Eq. (4.46), Eq. (4.471) and Eq. (4.48):

$$\frac{dy}{dt} = \frac{W}{f(W)}\varepsilon \tag{4.51}$$

Based on the moment balanced method, the lateral migration model can be expressed by Eq. (4.51) which has the same form as the headcut migration rate formula Eq. (4.35). It can be iterated and gets a deterministic W and $f(W)$. The lateral migration process will

stop when the toe erosion rate $\varepsilon = 0$, i.e., the lateral block cannot be infinitely tall if there is no erosion in the model, which well fits the lateral erosion development in prototype.

## 4.5 Incipient Velocity Test and Validation

In order to validate the proposed critical shear stress formulae for clay, the undisturbed clay erosion experiments (GeoDelft, 2003) were applied in Eq. (4.16). In the test, the rotating cylinder erosion device consists of a vertically placed metal cylinder with 1cm wide blades attached on the inside (Fig. 4.8). The internal diameter of the metal cylinder is 16 cm. The cylindrical soil sample, having a diameter of 6.6 cm and a height of 5 cm, is placed between two spindles with spikes of a few millimetres penetrating the sample. The sample and the two spindles are placed on a vertical metal axis. The axis is pierced through the centre of the sample and the spindles. The spindles are fixed onto the axis, which is placed between two ferrules, ensuring an independent rotation of the sample with respect to the rest of the apparatus.

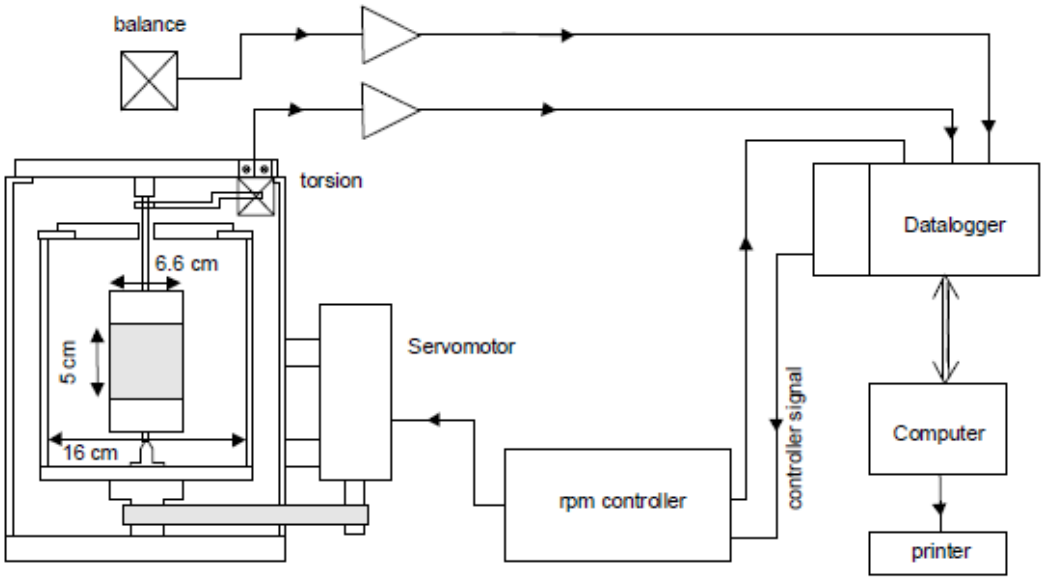


**Figure 4.8 Sketch of erosion test setup**

By rotating the metal cylinder, the inside water around the sample applies torsion on the sample. Due to the fact that the sample is independently hung from the rest of the apparatus, this torsion can be constantly measured. The erosion rate is measured every 10 minutes by measuring the weight of the sample.

The rotating cylinder erosion device is controlled by a computer. In the test procedure the rotation speed is kept constant during a certain period of time and is increased in steps. The working procedure is shown in Fig. 4.9.

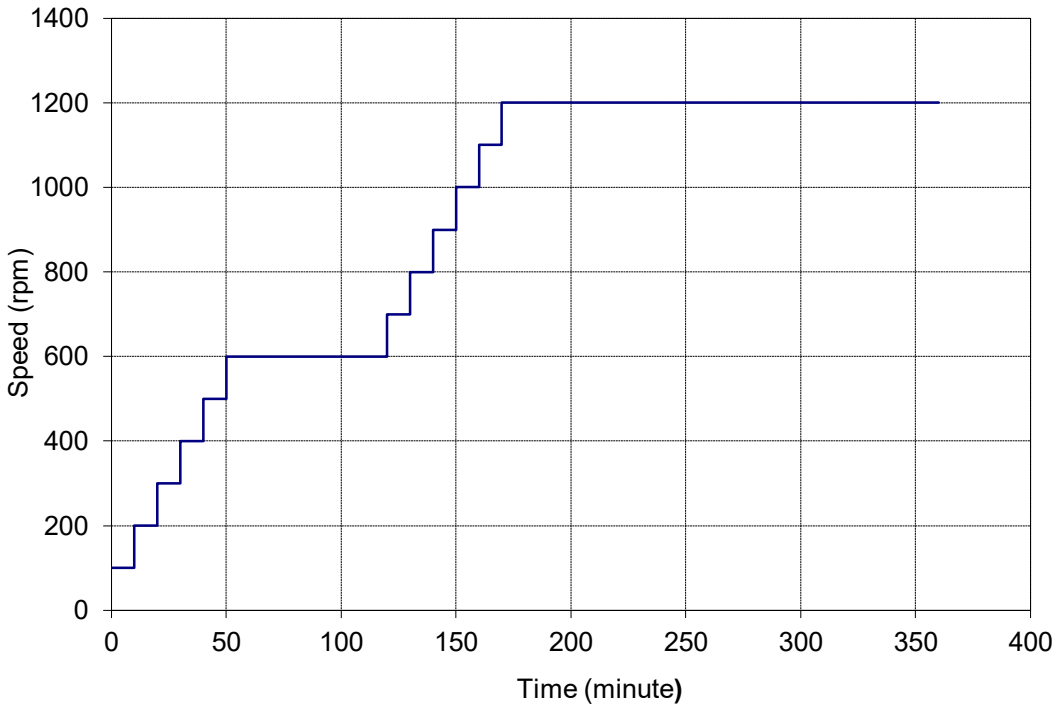


**Figure 4.9 Sketch of operation procedure of rotating cylinder erosion device**

Clay samples EG and CG were collected from Elisabethgroden and Cäciliengroden in the Netherlands, respectively. Their relevant properties are given in Table 4.1.

In the experiment two clay samples (EG and CG) were tested with the rotating cylinder erosion device. The shear stress was measured every 10 minutes. The detailed model

input can be seen in Appendix A. The shear stress to velocity was plotted for EG and CG in Fig. 4.11 and Fig. 4.12, respectively.

**Table 4.1 Properties of the clay samples**

| Clay type | | EG | CG |
|---|---|---|---|
| **Soil type** | | Cs13 | Csi2 |
| **Particle size distribution [%]** | < 2 μm | 24.2 | 48.8 |
| | < 16 μm | 38.6 | 77.3 |
| | > 2 μm and < 63 μm | 36.8 | 40.4 |
| | > 63 μm | 39.0 | 10.8 |
| **Water content in-situ [%]** | | 23 | 45 |
| **Undrained shear strength [kN/m$^2$]** | | 29.32 | 35.55 |
| **Specific density [g/cc]** | | 2.66 | 2.72 |

Notation: "EG" stands for the clay sample form Elisabethgroden and "CG" stands for clay sample from Cäciliengroden. "Cs13" stands for sandy clay; "Csi2" stands for silt clay.

In Eq. (4.15) and Eq. (4.16), the shear stress for the non-cohesive sediment should be used with the same diameter of undisturbed clay block. Therefore, the Shields Curve (Fig. 10) should be used to confirm the Shields Parameter $\theta_c$ in the calculation of shear stress of clay particle. For simplicity, $D_{50}$ is used to represent the non-cohesive sediment particle diameter. Then, the shear stress on clay block can be calculated with Eq. (4.16) for EG and CG, and is plotted in Fig. 4.11 and Fig. 4.12.

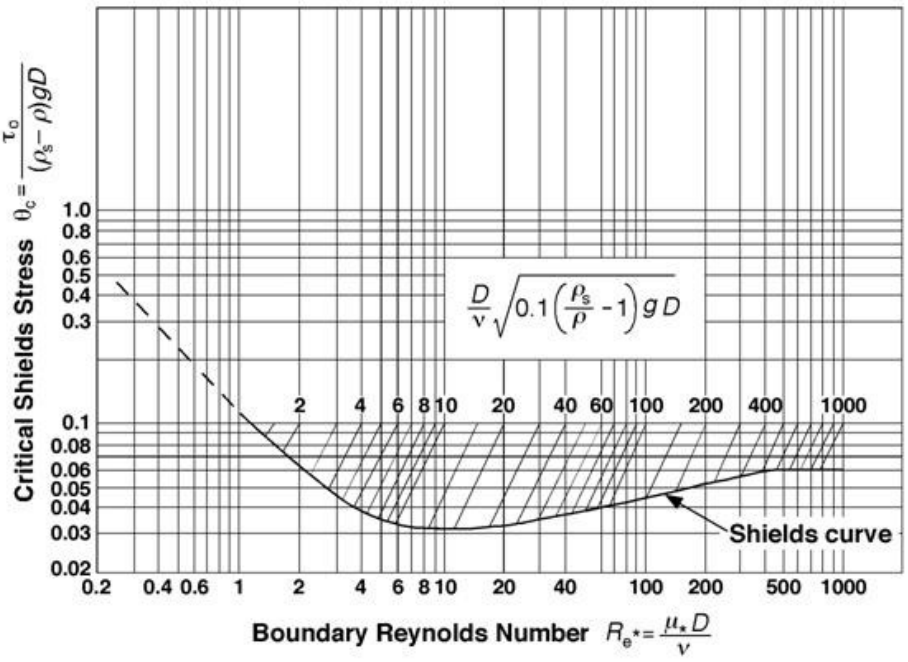


**Figure 4.10 Shields curve of non-cohesive sediment (Cao *et al.*, 2006)**

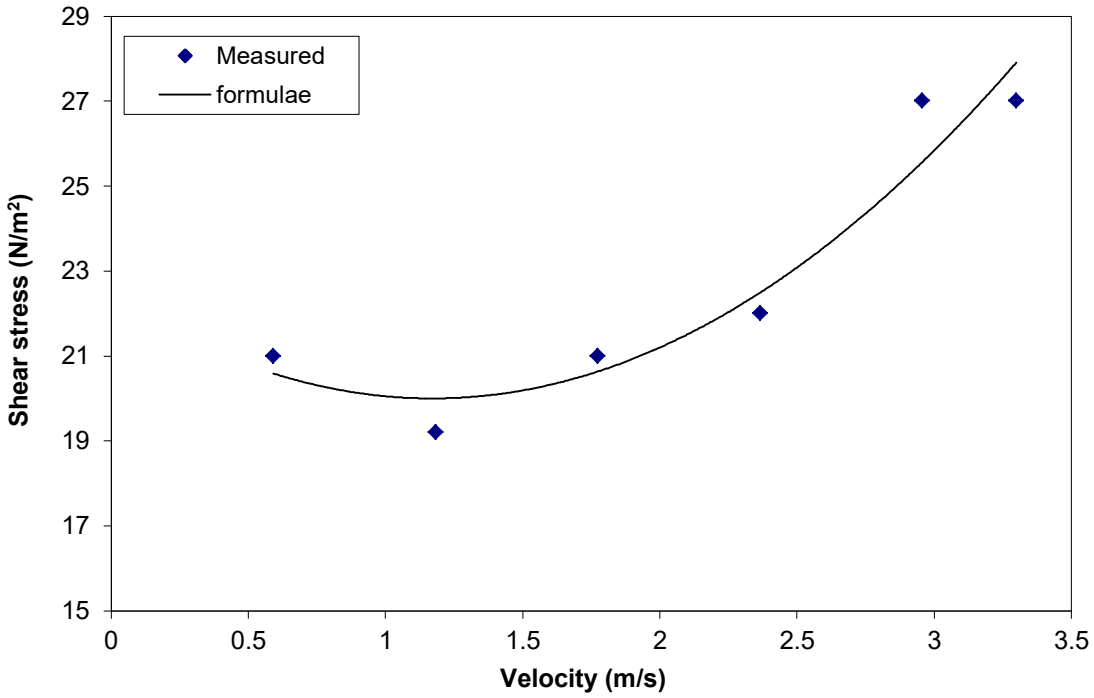


**Figure 4.11 Comparison of shear strength between measured data and calculated data for EG**

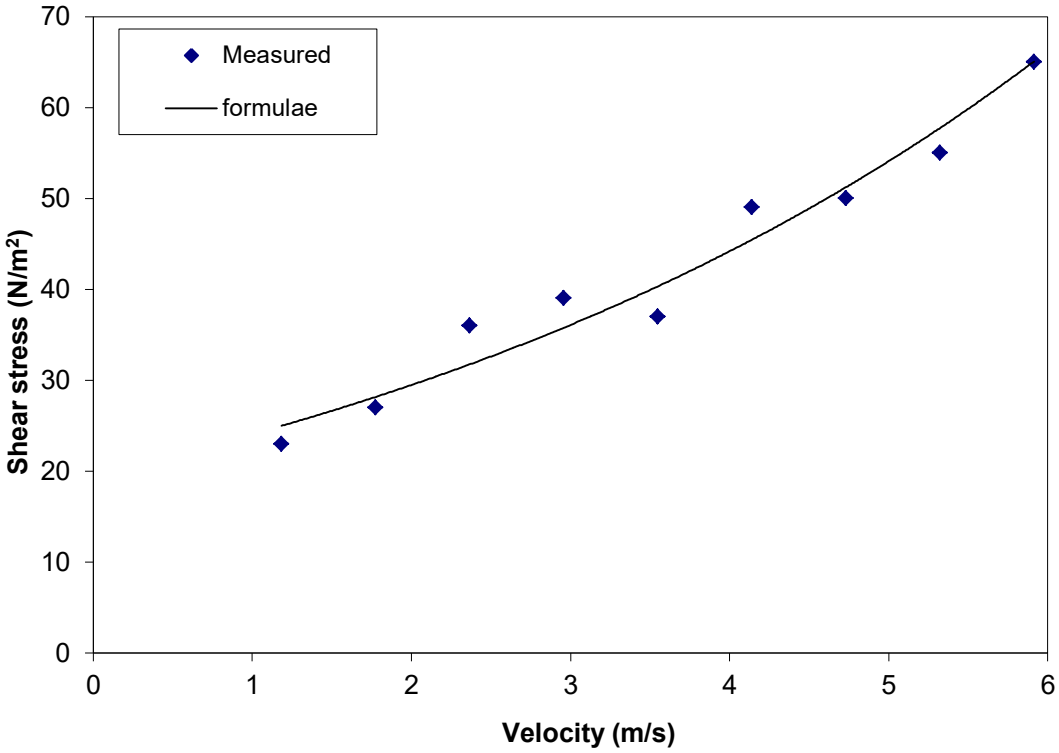


**Figure 4.12 Comparison of shear strength between measured data and calculated data for CG**

In the calculation of shear strength for sample clay, the calculated data can be fitted to the measured data with reasonable accuracy. Therefore, Eq. (4.15) and Eq. (4.16) can be used to calculate the shear strength of undisturbed clay. The relationships between shear strength and velocity of EG and CG are plotted in Fig. 4.11 and Fig. 12. These relationships can be used to predict other conditions without performing other tests.

## 4.6 Headcut Migration Model Validations

### 4.6.1 Headcut migration tests (Robinson and Hanson, 1995; Hanson *et al.*, 2004)

The tests were conducted in a flume with a length of 29.0 m and a width of 2.4 m. In the tests the upstream discharge was fixed as a constant flow rate. Headcut model heights varied from 0.9 m to 1.5 m. The properties of the series of tests are shown in Table 4.2. The materials included stratified and homogenous types of soil. During the constructions

of the headcut models, the soil materials were rolled layer by layer to build the model. The same material was used in every layer of the homogenous type, but the materials were changed in each layer in the case of the stratified type, i.e., one layer was made of sand and the next layer was made of clay. The surface of the fill was protected using carpet strips or a soil cement surface layer to minimize surface erosion and emphasize headcut migration.

Fourteen runs of headcut migration tests were done. The headcut migration rate appears to be different for each type of material under the same hydraulic parameters. The model materials played an important role in the headcut progress.

### 4.6.2 Model Validations

The clay incipient model (Eq. (4.15)) and headcut model (Eq. (4.35)) were validated by the fourteen headcut tests (Robinson and Hanson, 1995; Hanson *et al*., 2004. see Table 4.2). According to the material properties and the hydraulic parameters, the headcut migration rates were calculated based on the hydraulic parameters and the material properties. The calculated headcut migration rates were plotted in Fig. 4.13 to compare them with the measured data from the 14 tests. For the model built with the high erodibility rate ($\varepsilon$=0.172 m/s) materials, the headcut migration rates are close to, but a little lower than, the measured data. As for the moderate erodibility rate materials, the calculated headcut migration rates are close to the measured data, but for the low erodible materials, the calculated headcut migration rates are much lower than the measured data. The erosion rate is impacted by many factors from the materials, especially the materials that are not homogenous. The detailed model input can be seen in Appendix B.

**Table 4.2 Parameters for the headcut migration tests (Robinson and Hanson, 1995; Hanson *et al*., 2004)**

| Test | Material Type | $\rho_s$ (Kg/m$^3$) | $\varepsilon$ (m/s) | | $\tau_c$ (Pa) | | Wc (%) | Qu (KPa) | Q (m$^3$/s) | H (m) | h (m) | U (m/s) | dx/dt (m/h) |
|---|---|---|---|---|---|---|---|---|---|---|---|---|---|
| | | | Clay | Sand | Clay | Sand | | | | | | | |
| 1 | stratified | 1540 | 0.172 | 0.04 | 0.01 | 0.11 | 9.24 | 29 | 0.86 | 1.3 | 1.1 | 2.0 | 17.6 |
| 2 | homogeneous | 1540 | 0.172 | -- | 0.01 | -- | 9.24 | 29 | 0.86 | 1.3 | 1.1 | 2.0 | 18.6 |
| 3 | stratified | 1680 | 0.078 | 0.04 | 0.01 | 0.11 | 9.20 | 58 | 0.84 | 1.2 | 1.0 | 2.0 | 4.7 |
| 4 | homogeneous | 1680 | 0.078 | -- | 0.01 | -- | 9.20 | 58 | 0.84 | 1.2 | 1.0 | 2.0 | 5.4 |
| 5 | stratified | 1590 | 0.068 | 0.04 | 0.08 | 0.11 | 11.60 | 21 | 0.86 | 1.3 | 1.0 | 2.0 | 9.1 |
| 6 | homogeneous | 1590 | 0.068 | -- | 0.08 | -- | 11.60 | 21 | 0.86 | 1.3 | 1.0 | 2.0 | 6.8 |
| 7 | stratified | 1790 | 0.006 | 0.04 | 1.32 | 0.11 | 14.40 | 89 | 0.86 | 1.3 | 1.0 | 2.0 | 1.7 |
| 8 | homogeneous | 1790 | 0.006 | -- | 1.32 | -- | 14.40 | 89 | 0.86 | 1.3 | 1.0 | 2.0 | 0.2 |
| 9 | stratified | 1790 | 0.007 | 0.04 | 1.21 | 0.11 | 14.23 | 83 | 0.85 | 1.2 | 1.0 | 2.0 | 1.7 |
| 10 | homogeneous | 1790 | 0.007 | -- | 1.21 | -- | 14.23 | 83 | 0.85 | 1.2 | 1.0 | 2.0 | 0.3 |
| 11 | stratified | 1710 | 0.009 | 0.04 | 0.72 | 0.11 | 14.36 | 63 | 0.85 | 1.3 | 1.0 | 2.0 | 2.2 |
| 12 | homogeneous | 1710 | 0.009 | -- | 0.72 | -- | 14.36 | 63 | 0.85 | 1.3 | 1.0 | 2.0 | 0.9 |
| 13 | stratified | 1780 | 0.002 | 0.04 | 2.46 | 0.11 | 15.93 | 40 | 0.88 | 1.2 | 0.9 | 2.0 | 3.6 |
| 14 | homogeneous | 1780 | 0.002 | -- | 2.46 | -- | 15.93 | 40 | 0.88 | 1.2 | 0.9 | 2.0 | 0.1 |

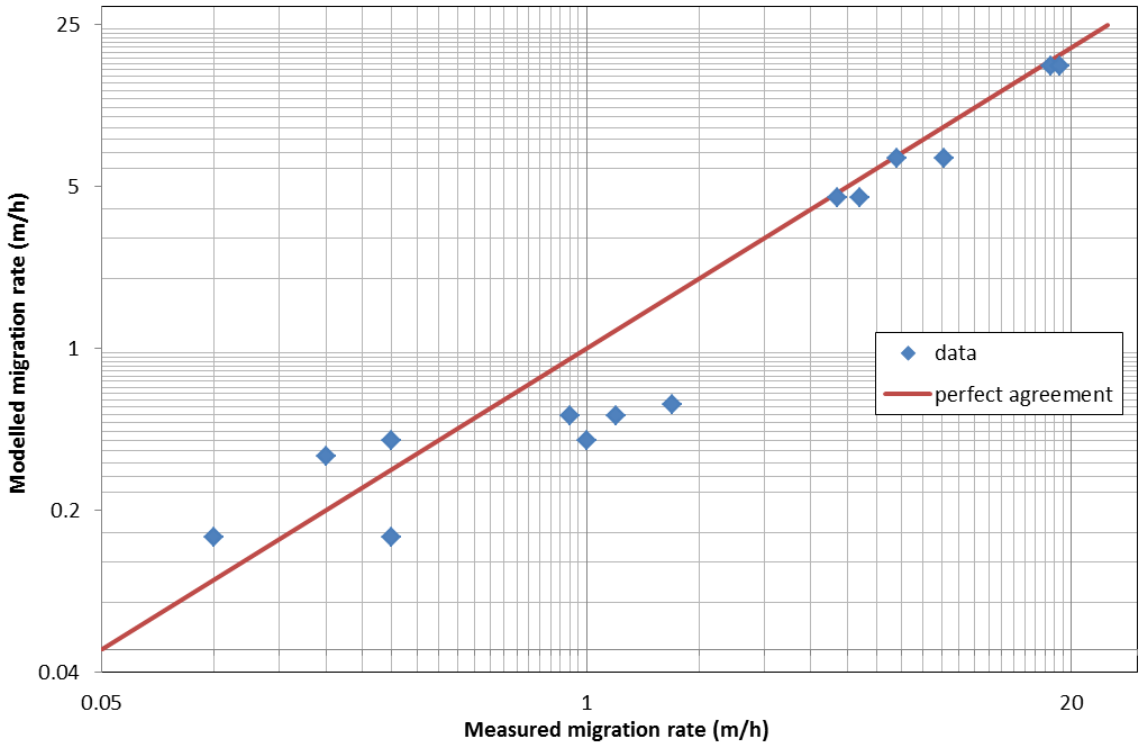


**Figure 4.13 Agreement between measured headcut migration rate and calculated headcut migration rate**

It can be concluded that the calculated results are slightly lower than the measured data, however, the agreements are very good when considering the variability of the materials. The new headcut migration model has been applied to the equilibrium moment principle and to the new clay incipient motion theory. It can simulate and predict the hydrodynamic erosion process of the headcut on the breach slope. The moment based method is a good approach to describe the dynamic headcut process based on the validations.

## 4.7 Discussion

Due to the cohesion among clay particles, this research proposes that the clay erosion is in the form of clay blocks, however, clay erosion was, in past research, assumed to take place in the form of single particles. An erosion and moment equilibrium-based method is proposed to simulate the headcut development and migration in cohesive embankment

breaching. The new headcut model (Eq. (4.16) and Eq. (4.35)) is able to simulate the hydro-dynamic and morphologic headcut migration. It can be applied to calculate the incipient motion of the soil and the migration of the headcut movement in the breach in the cohesive embankment. The new method has been validated using laboratory data (GeoDelft, 2003; Robinson and Hanson, 1994). It is found that the calculated results give good predictions of the development of the headcut erosion on the breach slope. The lateral erosion model has been proposed in the same way as the headcut migration model. The lateral migration model Eq. (4.51) can simulate and predict the breach development in the lateral direction, and it reflects the widening process of the breach. Additionally, the clay incipient motion model, the headcut migration model and the lateral erosion model can be coupled to describe the breach erosion process in three dimensions. Both the headcut erosion model and the lateral erosion model will be coupled together to simulate the breaching process of cohesive embankments (see Chapter 7). Once again, the headcut erosion and lateral erosion are in the form of clay blocks. The proposed erosion models are of significance to estimate the breach growth in cohesive embankments.

# Chapter 5 Large-Scale Embankment Breaching Experiments[3]

## 5.1 Introduction

Doing breach experiments (Wahl, 2007) is an effective methodology to get insight into the embankment breaching mechanism. Visser (1998) conducted a laboratory test and a field test to study the sandy dike breaching process. Zhu (2006) studied the clayey dike breach in a flume in the Laboratory for Fluid Mechanics of Delft University of Technology. Zhang *et al*. (2009) and Peeters *et al*. (2012, 2014) conducted field tests to study the real embankment dam and dike breaching mechanisms, respectively. The prototype data analysis (e.g. Tangjiashan Landslide Barrier breach) is also used to study the mechanism of embankment breaching process.

In a laboratory flume, the scale effects increase the uncertainty of the breach development and the measured results may introduce distortions. In situ, the prototype data are analysed to study the embankment breaching process, however, these data are usually inaccurate and not complete. The field test can be a good option to reduce the scale influence from the model, but the real breaching test usually involves higher costs than the laboratory test and requires quite an effort to adhere to efficient and accurate measurement.

In this chapter, a series of large-scale embankment breaching tests in a large flume are described, that were designed to reduce the scale impacts and defects of the prototype experiments. They were performed to investigate the embankment breaching process, including surface erosion, headcut erosion, and lateral erosion as well as the breach

[3] This chapter is revised from "Gensheng Zhao, Paul Visser, Patrik Peeters. Large Scale Embankment Breach Experiments in Flume. Report of Delft University of Technology, Flanders Hydraulics Research and Rijkswaterstaat, 2014."

hydraulics in different breaching stages. The breach hydrological processes and the topographical changes were also measured. The large-scale embankment breach experiments can greatly contribute to the study of the embankment breaching mechanism, but can also be applied to verify and calibrate mathematical breach models.

## 5.2 Experimental Setup

### 5.2.1 Introduction of the Flume

Experiments were conducted in the large flume (60 m long, 3 m wide and 3 m high) of Changjiang River Scientific Research Institute, Changjiang River Water Resources Commission, China. The maximum discharge that can be supplied is 1 $m^3/s$. The flume layouts are shown in Fig. 5.1, Fig. 5.2 and Fig. 5.3. Two sidewalls of the flume were made up of enforced concrete frames and reinforced glass, and the transit channel and outlet channel were built with bricks. There are 14 glass windows in the main test reach with a total length of 35 m.

To the flume system, a reservoir and a sedimentation basin of 20 m long, 10 m wide and 3 m deep, in which the sediment well deposited, are connected (see Fig. 5.1). The discharge is generated by 7 pumps and controlled by two electromagnetic flow meters.

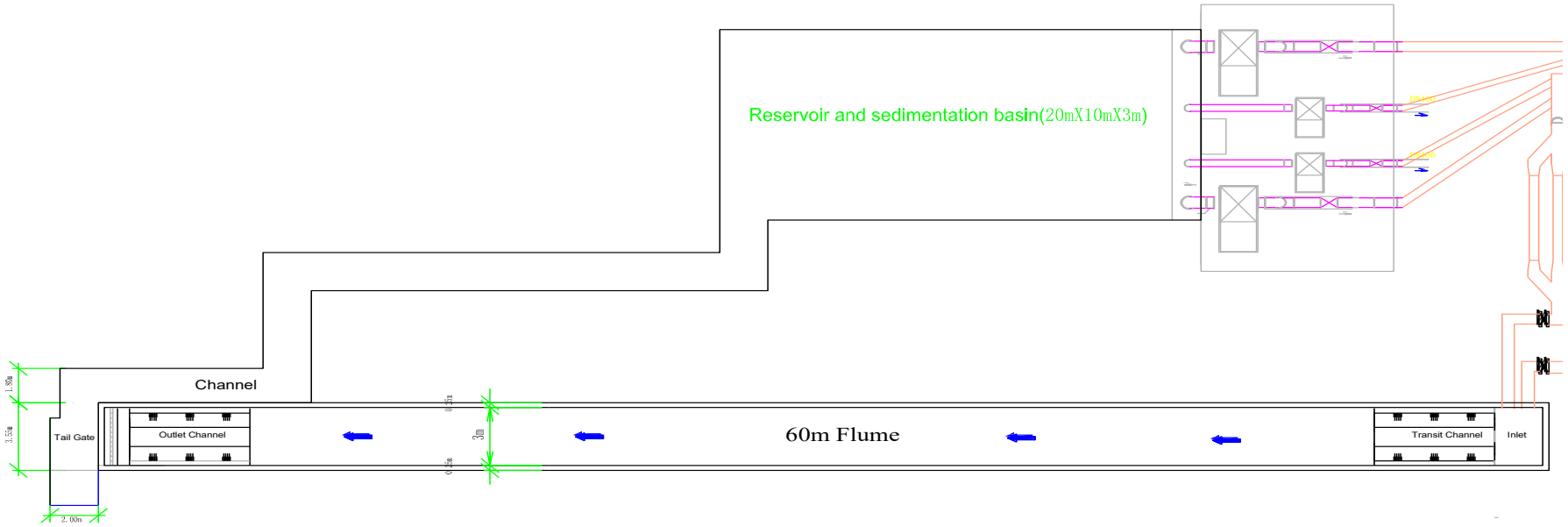


**Figure 5.1 Layout of the flume (to be constituted)**

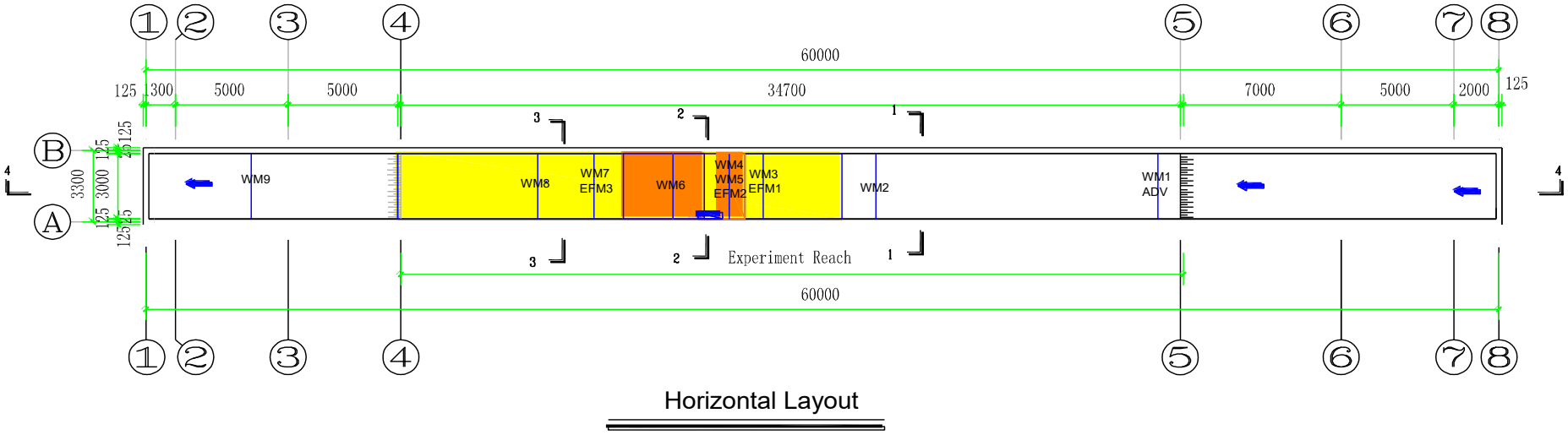


**Figure 5.1 Layout of the flume (to be constituted)**

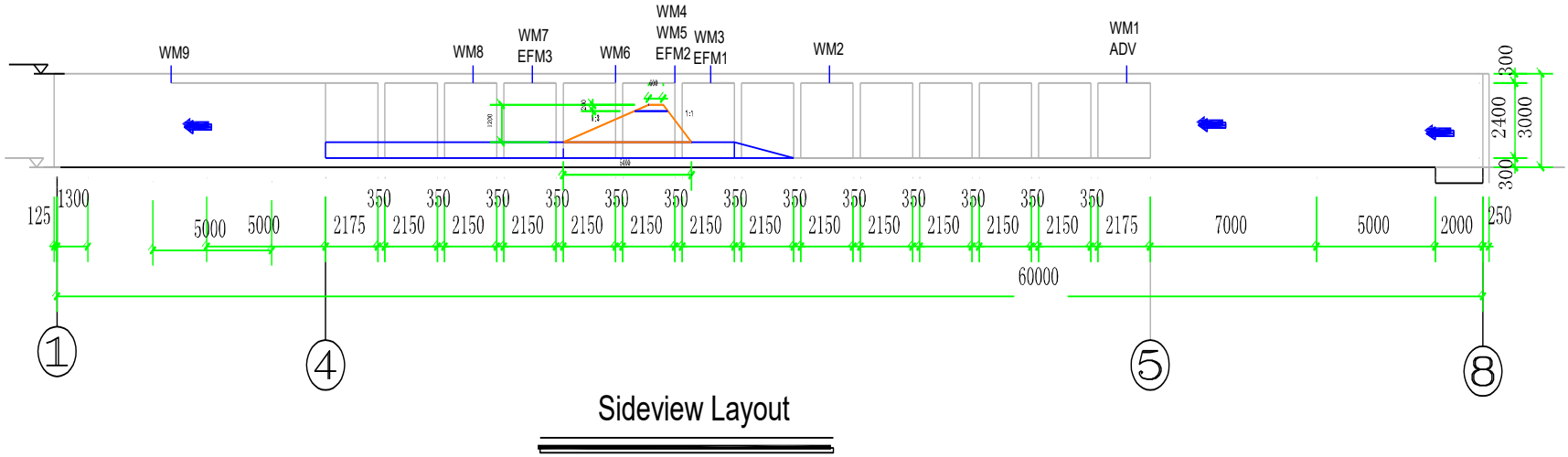


**Figure 5.1 Layout of the flume (to be constituted)**

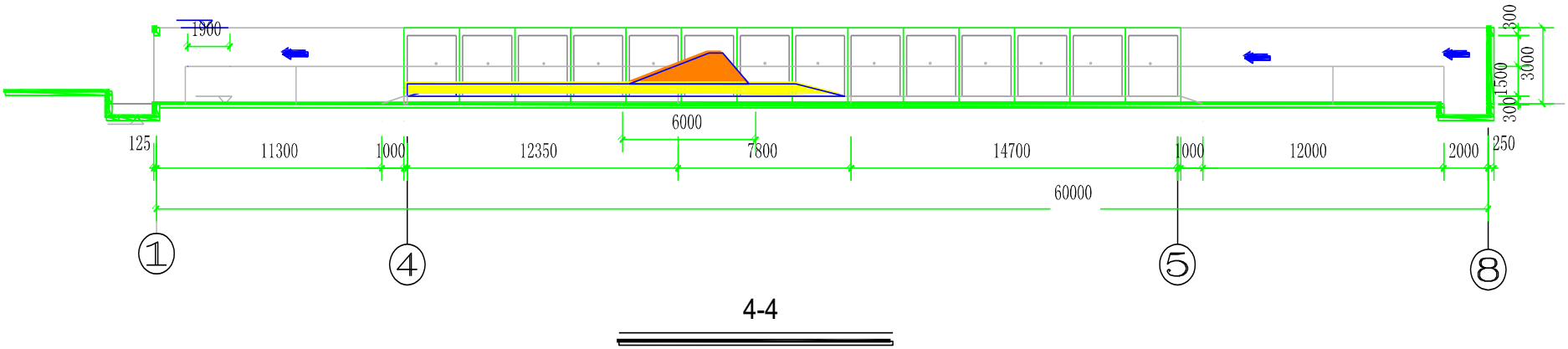


**Figure 5.1 Layout of the flume (constituted)**

**Figure 5.2 Overview of flume from tailgate (Model 1)**

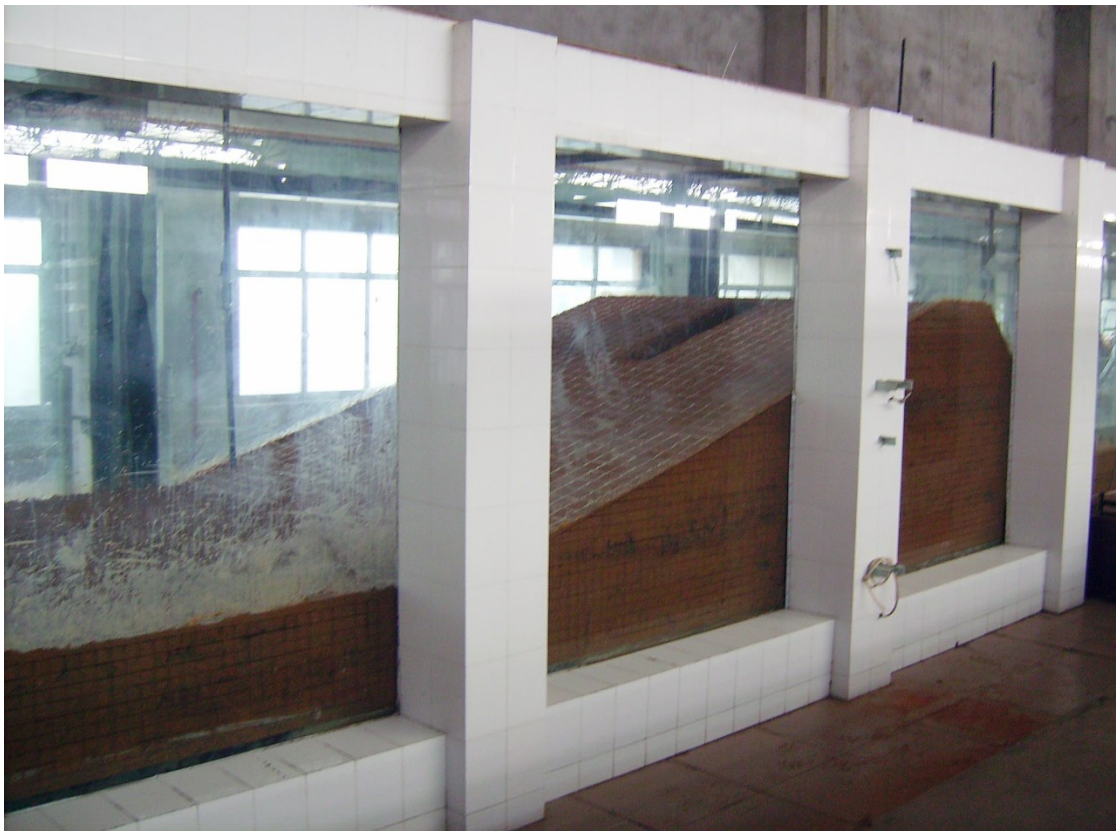

**Figure 5.3 Flume side view (Model 5)**

### 5.2.2 Embankment Model Design

Five embankment breaching experiments were performed in the flume. All the model parameters are shown in Table 5.1, Fig. 5.4, Fig. 5.5, Fig. 5.6, Fig. 5.7 and Fig. 5.8. The embankments were built on an erodible flume bed, 0.8 m thick of clay with the same characteristics as the clay of the model dike. Four experiments were done with an embankment height of 1.20 m, and one experiment was done with an embankment height of 0.6 m to investigate the scale effect. The waterside slopes were 1:1 in all models, the landside slopes were 1:3 and 1:2 to investigate the influence of variation in the slope. The crest widths were 0.6 m in all models. The initial trench was 0.3 m wide and 0.4 m deep.

**Table 5.1 Breach scale model parameters**

| Parameters | Model 1 | Model 2 | Model 3 | Model 4 | Model 5 |
|---|---|---|---|---|---|
| Experiment Date | 01/02/2013 | 27/02/2013 | 07/03/2013 | 14/03/2013 | 22/03/2013 |
| Initial Trench Location | Side | Side | Side | Side | Middle |
| Dam Length (m) | 3 | 3 | 3 | 3 | 3 |
| Dam Height (m) | 0.6 | 1.2 | 1.2 | 1.2 | 1.2 |
| Dam Crest Width (m) | 0.6 | 0.6 | 0.6 | 0.6 | 0.6 |
| Waterside slope | 1V:1H | 1V:1H | 1V:1H | 1V:1H | 1V:1H |
| Landside slope | 1V:2H | 1V:2H | 1V:3H | 1V:3H | 1V:3H |
| Bottom Width (m) | 3.6 | 4.2 | 5.4 | 5.4 | 5.4 |
| Flume bed Length (m) | 20 | 20 | 20 | 20 | 20 |
| Flume bed Thickness (m) | 0.5 | 0.5 | 0.5 | 0.5 | 0.5 |
| Volume($m^3$) | 33.78 | 38.64 | 40.8 | 40.8 | 40.8 |

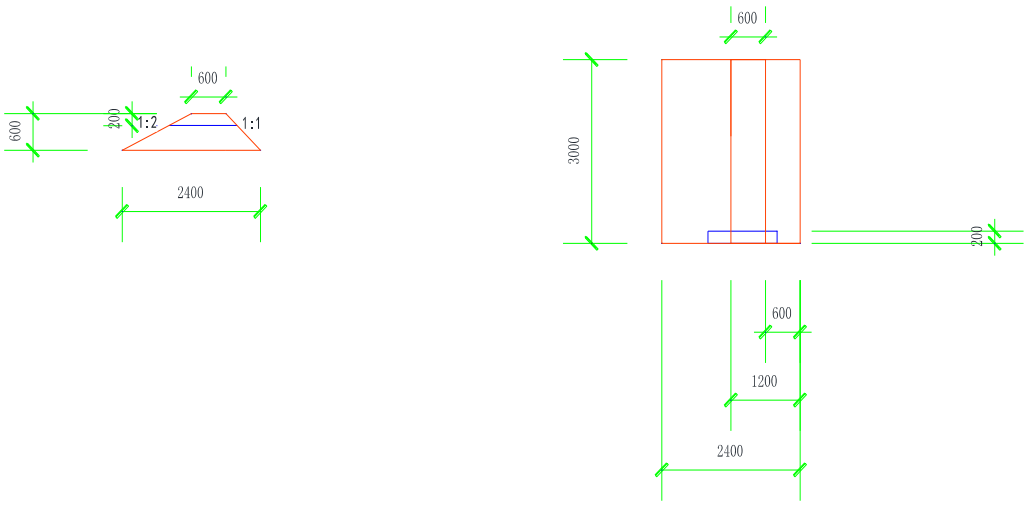


**Figure 5.4 Design of Model 1**

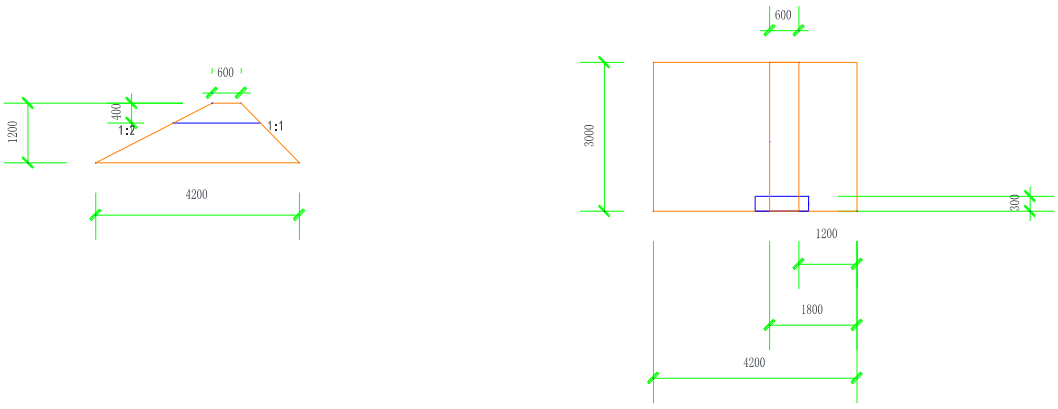


**Figure 5.5 Design of Model 2**

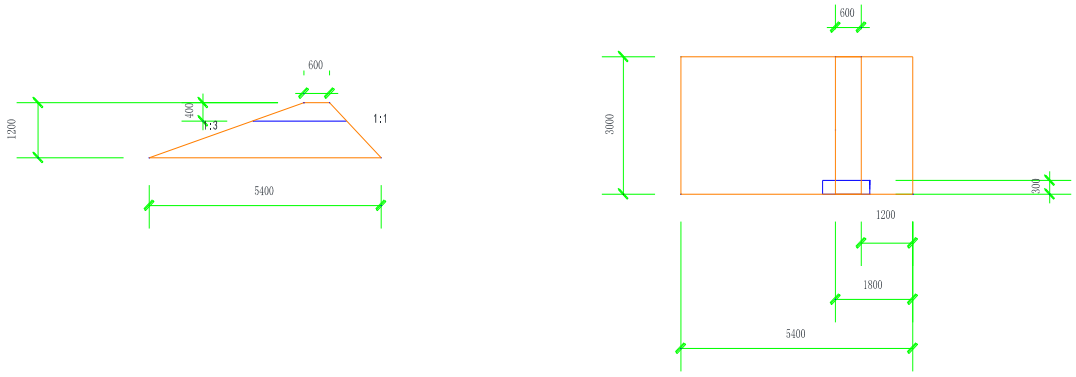


**Figure 5.6 Design of Model 3**

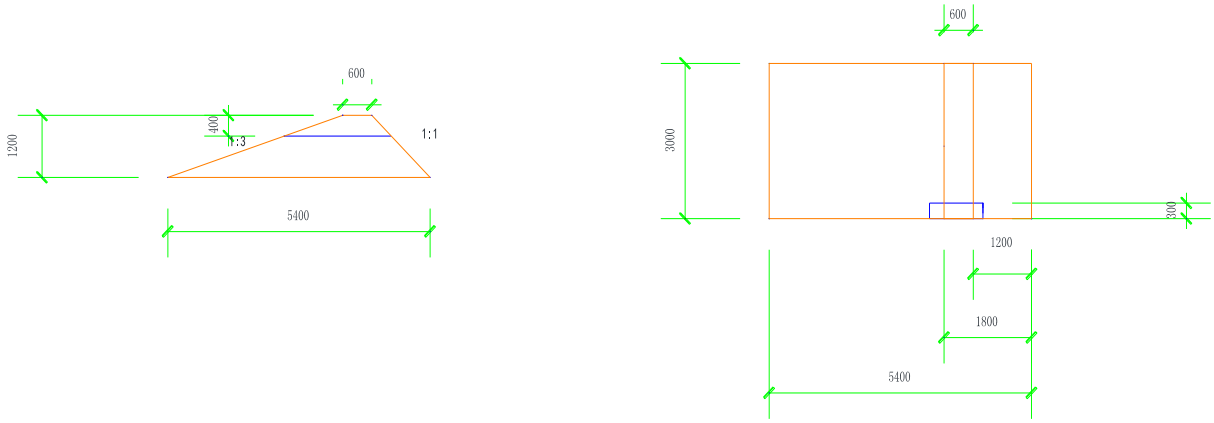


**Figure 5.7 Design of Model 4**

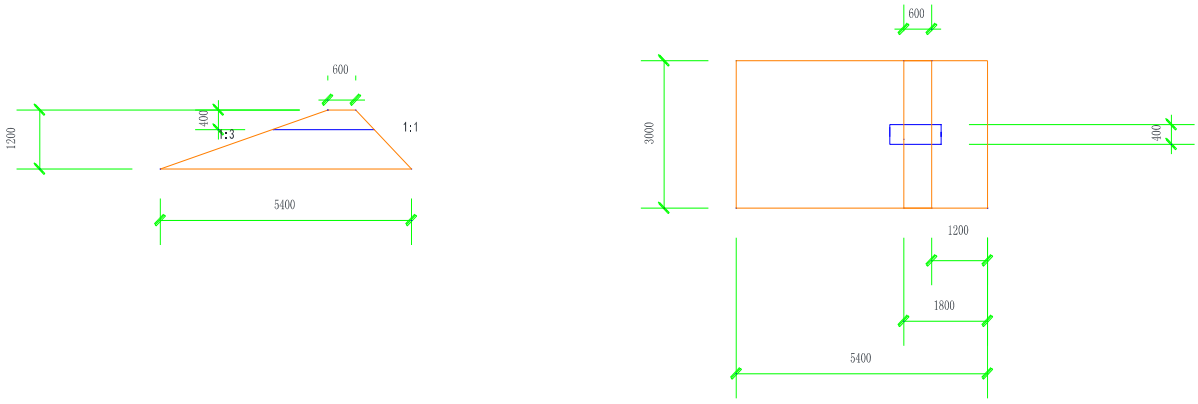


**Figure 5.8 Design of Model 5**

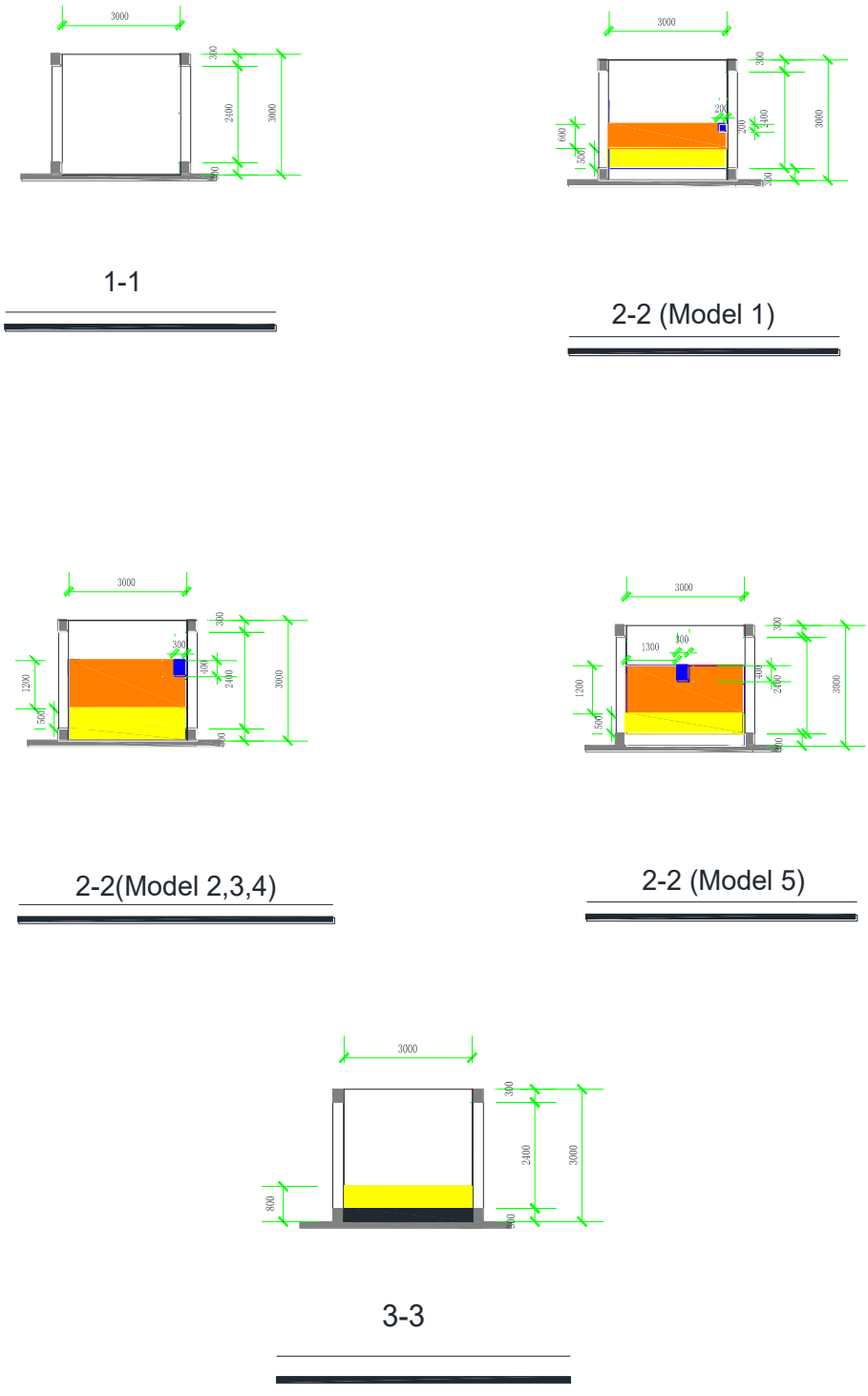


**Figure 5.9 Cross-sections (Side Breach; Middle Breach)**

In order to study the impact of the initial breach location, two locations of the initial breach trench were applied: against the side wall of the flume (Fig. 5.10) and in the middle of the flume (Fig. 5.11). The flow through the initial breach channel triggers the breaching process, i.e., in practice, it is the weakest point in the embankment.

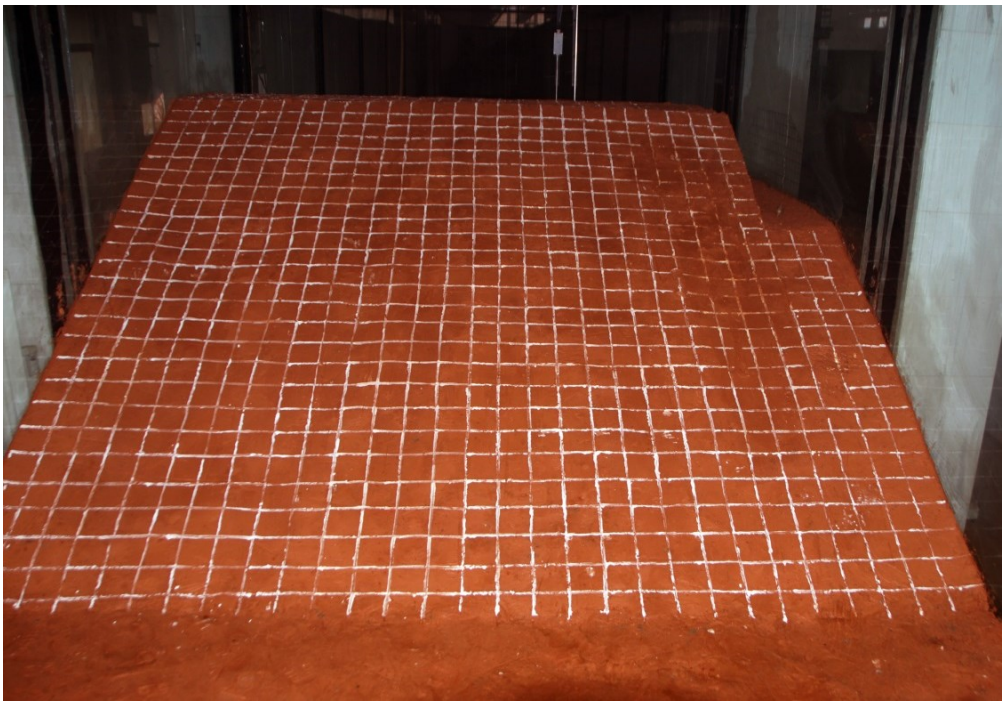

**Figure 5.10 Model 2 with side initial breach channel from downstream slope**

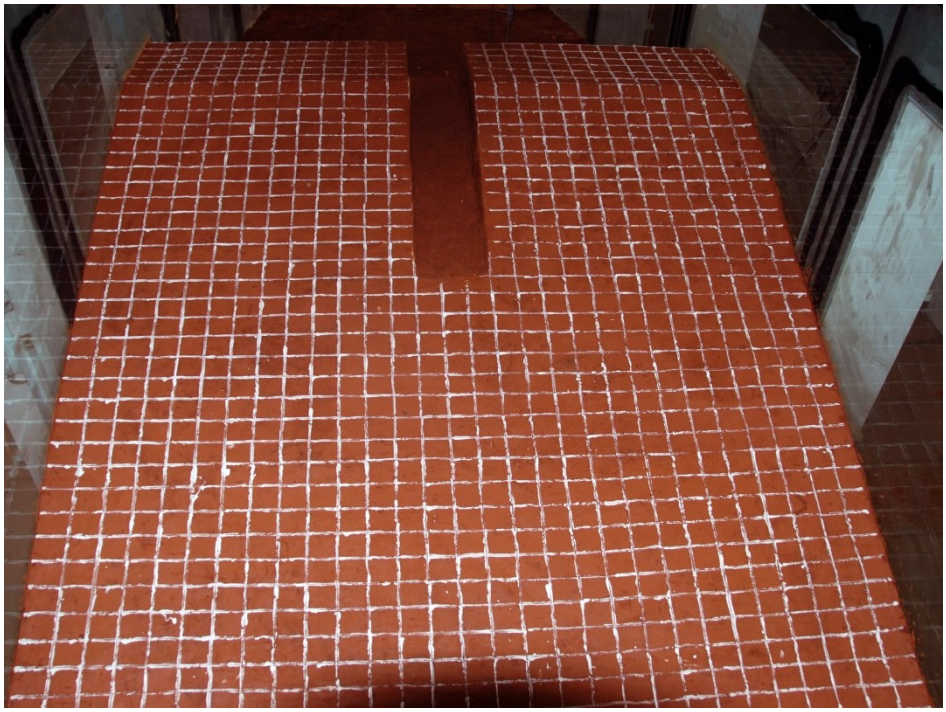

**Figure 5.11 Model 5 with middle initial breach channel from downstream slope**

## 5.3 Laboratory Soil Test

### 5.3.1 Introduction

Cohesive embankment breaching is a hydraulic problem coupled with soil mechanics. Thus, a series of soil tests were conducted in the laboratory before the flume experiments. A wide variety of laboratory tests can be performed on soils to measure various soil properties. Some soil properties are intrinsic to the composition of the soil matrix and are not affected by sample disturbances, while other properties depend on the structure of the soil as well as its composition, and can only be effectively tested on relatively undisturbed samples. Some soil tests measure direct properties of the soil, while others measure "index properties", which provide useful information about the soil without directly measuring the property desired.

In the next part of this chapter, the soil tests in the laboratory involved in this breach experiment will be described, including the water content of soil, soil density (dry density, relative density), aspects of particle size analysis, proctor compaction test, Atterberg

limits (Shrinkage limit, Plastic limit, Liquidity limit), direct shear stress, triaxial shear test, permeability and compression of soil.

### 5.3.2 Density and Water Content

In order to keep the embankment homogenous, the models were made layer by layer, each layer having a thickness of 20 cm. The samples were collected after every layer had been compressed. Then, the bulk density, dry density and water content were tested in the soil mechanics lab. The bulk density distributions are shown in Fig. 5.12. The bulk density distributions in the 5 models differ slightly due to the small material variations in the constructions. The dry densities are shown in Fig. 5.13 and also have good homogenous distributions. Water content tests (Fig. 5.14) provided the water content of the soil, normally expressed as a percentage of the weight of water to the dry weight of the soil. It can influence the cohesion of the model material.

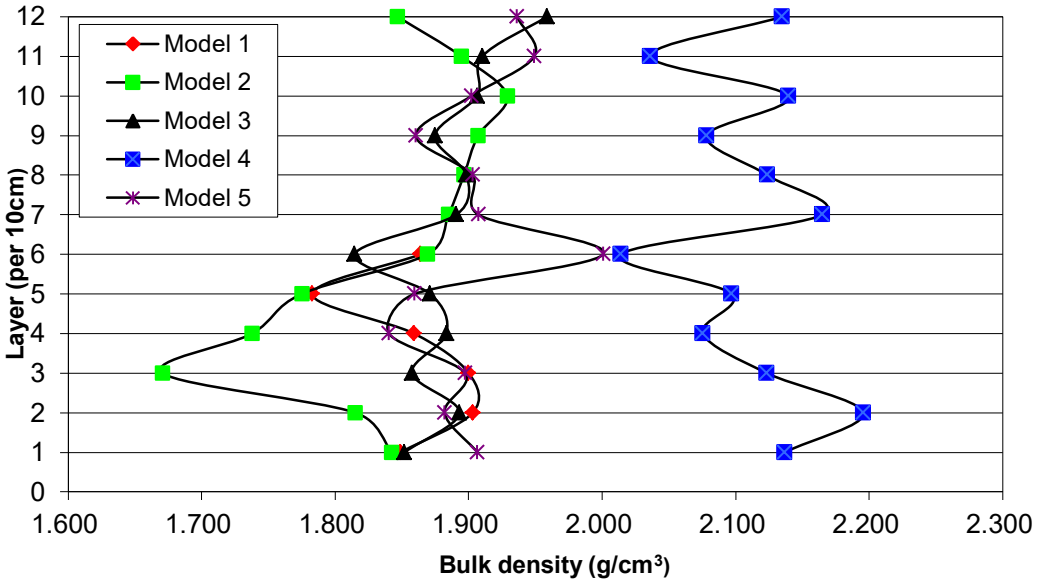


**Figure 5.12 Model material bulk density distributions**

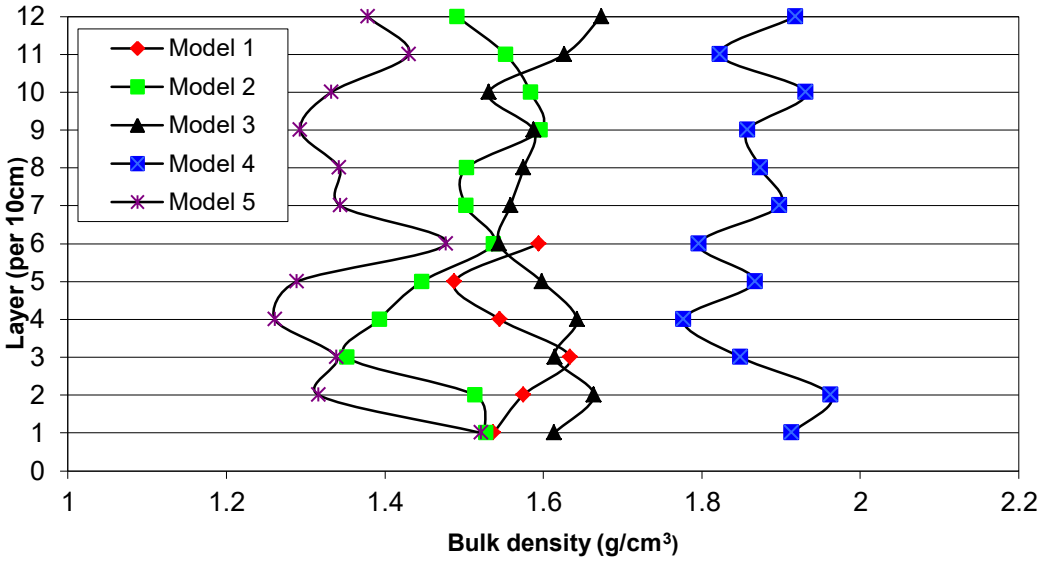


**Figure 5.13 Model material dry density distributions**

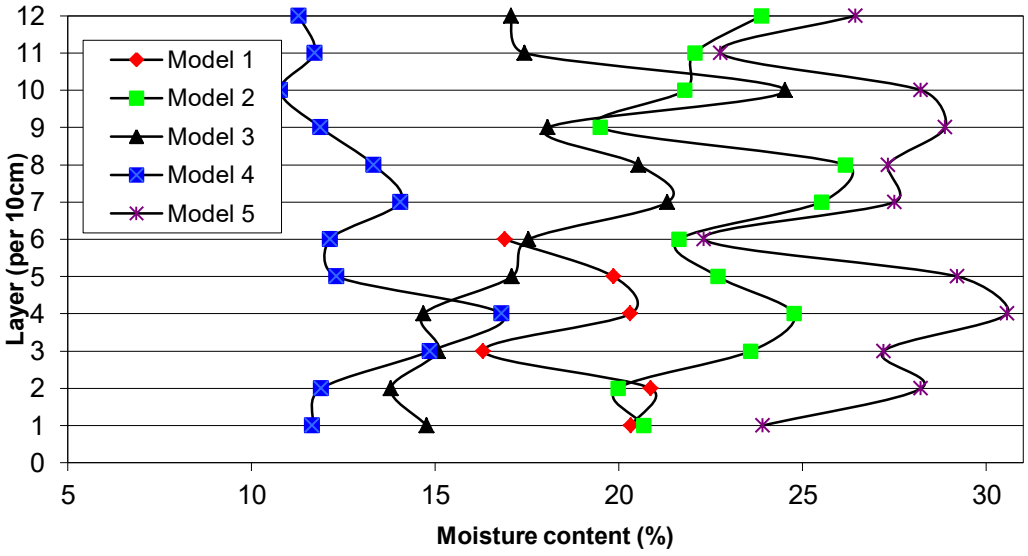


**Figure 5.14 Model material water content distributions**

### 5.3.3 Particle Size Analysis

A particle size analysis was performed to determine the soil gradation. Coarser particles were separated in the sieve analysis portion, and the finer particles were analysed with a hydrometer. The distinction between coarse and fine particles is usually made at 75 μm. The sieve analysis shakes the sample through progressively smaller meshes to determine its gradation. The hydrometer analysis uses the rate of sedimentation to determine particle gradation (see Fig. 5.15). The sand-clay mixture was used to build Model 4.

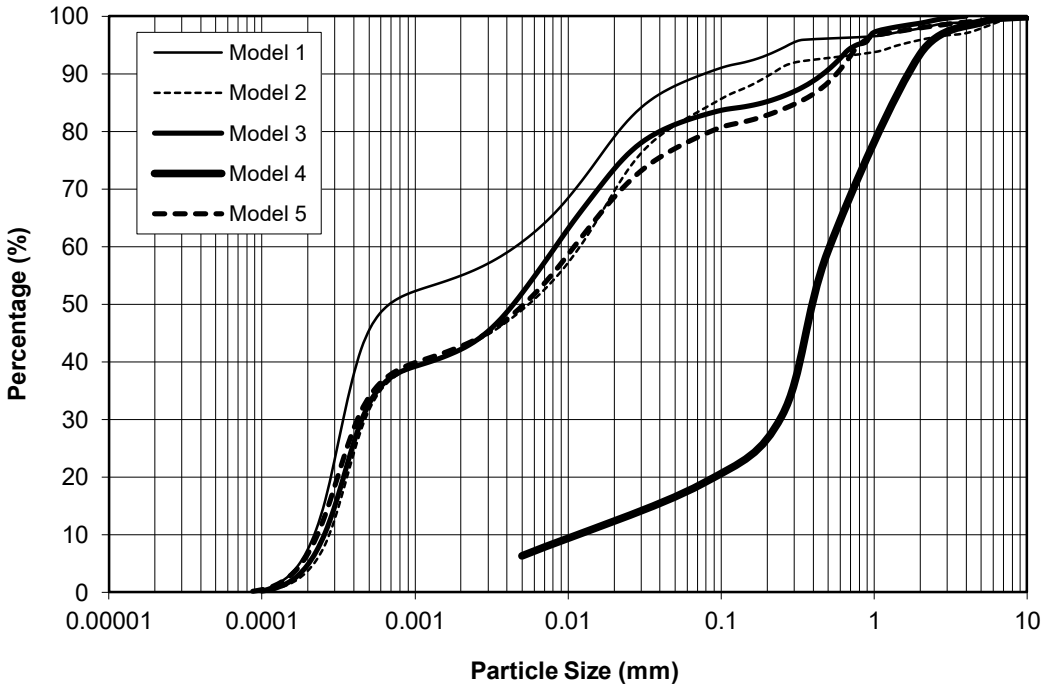


**Figure 5.15 Model material grading**

### 5.3.4 Proctor Compaction Test

Compaction is the process by which the bulk density of an aggregate of matter is increased by driving air out. For any soil, for a given amount of compactive effort, the density obtained depends on the moisture content. At very high moisture contents, the maximum dry density is achieved when the soil is compacted to near-saturation, where (almost) all the air is driven out. At low moisture contents, the soil particles interfere with each other; addition of some moisture will allow greater bulk densities, with a peak density where this effect begins to be counteracted by the saturation of the soil.

According to the proctor compaction test process, 4 clay samples (without Model 4) were prepared with different compaction times. The relationships between optimum water content and dry density were obtained after 5 times of compaction (see Fig. 5.16). The optimum water content is 21.3% and the maximum dry density is 1.61 g/m$^3$ based on the compaction tests.

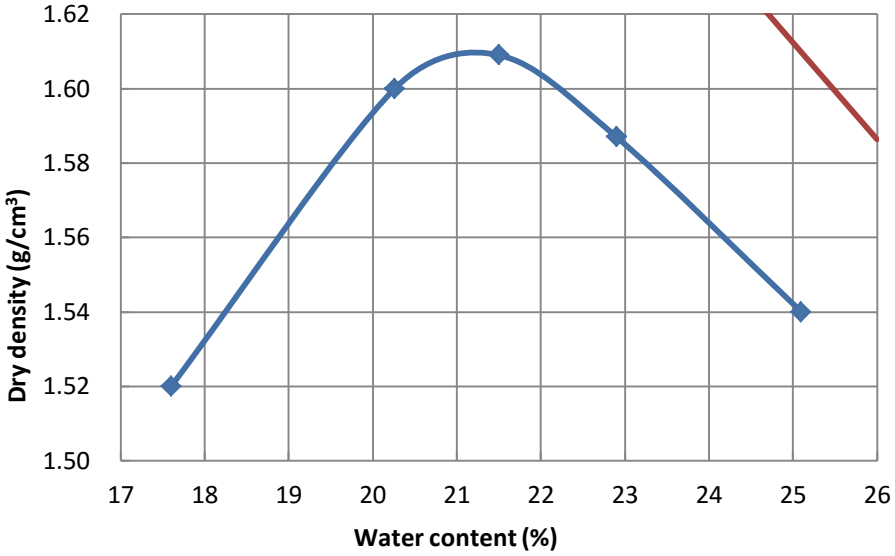


**Figure 5.16 Relationship between optimum water content and dry density**

### 5.3.5 Atterberg Limits

The Atterberg limits are a basic measure of the nature of a fine-grained soil. Depending on the water content of the soil, it may appear in four states: solid, semi-solid, plastic and liquid. In each state the consistency and behaviour of a soil is different and consequently, so are its engineering properties. Thus, the boundary between each state can be defined based on a change in the soil's behaviour. The Atterberg limits can be used to distinguish between silt and clay and can distinguish between different types of silts and clays. The Atterberg Limits test results are shown in Table 5.2.

(1) Shrinkage limit

The shrinkage limit (SL) is the water content, where further loss of moisture will not result in any more volume reduction. The test to determine the shrinkage limit is ASTM

International D4943. The shrinkage limit is much less used than the liquid and plastic limits.

(2) Plastic limit

The plastic limit is determined by rolling out a thread of the fine portion of a soil on a flat, non-porous surface. The procedure is defined in ASTM Standard D-4318. If the soil is plastic, the thread will retain its shape down to a very narrow diameter. The sample can then be re-modelled and the test repeated.

As the moisture content falls due to evaporation, the thread will begin to break apart at larger diameters. The plastic limit is defined as the moisture content where the thread breaks apart at a diameter of 3 mm.

(3) Liquid limit

The liquid limit (LL) is the water content at which a soil changes from plastic to liquid behaviour. The original liquid limit test of Atterberg involved mixing a part of clay in a round-bottomed porcelain bowl of 10 - 12 cm diameter. A groove was cut through the paste of clay with a spatula, and the bowl was then struck many times against the palm of one hand.

**Table 5.2 Atterberg limits test results**

| Liquid limit (LL) | Liquid limit (LL) | Plastic limit | Plasticity Index | Plasticity index |
|---|---|---|---|---|
| $W_{L17}$ | $W_{L10}$ (%) | $W_p$ | $I_{P17}$ | $I_{P10}$ |
| 48.3 | 38.6 | 19.6 | 28.7 | 19.0 |

## 5.3.6 Direct Shear Stress

The direct shear test determines the consolidated, drained strength properties of a sample. A constant strain rate is applied to a single shear plane under a normal load, and the load

response is measured. If this test is performed with different normal loads, the common shear strength parameters can be determined (see Table 5.3).

### 5.3.7 Triaxial Shear Test

This type of test is used to determine the shear strength properties of a soil. It can simulate the confining pressure a soil would have deep into the ground. It can also simulate drained and undrained conditions.

The unconsolidated undrained tests were used to test the Zhuankou (China) clay sample. In the test, the sample is not allowed to drain. The shear characteristics are measured under undrained conditions and the sample is assumed to be unsaturated. Based on the Mohr's strain circle method, the triaxial shear test results are shown in Table 5.3.

**Table 5.3 Model sample characteristics**

| NO. | Sample | Soil Type | Sample Characteristics | | | | |
|---|---|---|---|---|---|---|---|
| | | | Median diameter | Moisture content | Bulk density | dry density | Degree of saturation |
| | | | $D_{50}$ | $w$ | $\rho$ | $\rho_d$ | $S_r$ |
| | | | $\mu$m | % | g/cm$^3$ | g/cm$^3$ | % |
| 1 | Model 1 | silty clay | 0.7 | 28.8 | 1.86 | 1.47 | 92.6 |
| 2 | Model 2 | silty clay loam | 5 | 28.7 | 1.84 | 1.49 | 94.8 |
| 3 | Model 3 | silty clay | 5 | 25.6 | 1.88 | 1.51 | 86.5 |
| 4 | Model 4 | loam sand | 400 | 16.1 | 2.11 | 1.84 | 93.2 |
| 5 | Model 5 | silty clay | 5 | 26.4 | 1.90 | 1.54 | 93.7 |
| 6 | Model Layer | silty clay loam | 5 | 29.5 | 2.01 | 1.48 | 95.0 |

**Table 5.3 Model sample characteristics (continued)**

| NO. | Mechanic Indicator | | | | | | Permeability test |
|---|---|---|---|---|---|---|---|
| | Compression test | | Direct shear stress | | Triaxial shear test (UU) | | |
| | $a_{v1\text{-}2}$ | $Es_{1\text{-}2}$ | $C_q$ | $\varphi_q$ | $C_u$ | $\varphi_u$ | $K_{20}$ |
| | $MPa^{-1}$ | MPa | kPa | ° | kPa | ° | cm/s |
| 1 | 0.322 | 5.6 | 15.4 | 3.6 | 12.7 | 3.0 | 8.02E-06 |
| 2 | 0.327 | 5.5 | 20.2 | 1.6 | 8.1 | 2.0 | 7.90E-06 |
| 3 | 0.313 | 5.7 | 15.9 | 4.8 | 16.9 | 5.0 | 5.50E-06 |
| 4 | 0.082 | 18.2 | 8.2 | 33.6 | 4.4 | 32.1 | 1.36E-04 |
| 5 | 0.254 | 7.0 | 16.0 | 4.2 | 14.6 | 6.0 | 1.75E-05 |
| 6 | 0.312 | 6.1 | 16.0 | 1.9 | 11.9 | 1.9 | 5.71E-06 |

### 5.3.8 Permeability Test

Constant head permeability tests were used to calculate seepage potential through earthen dams and embankments such as dikes. In the testing a specialized device, referred to as a constant head permeameter, is used. In the test, the permeameter is filled with test soil and water is run through the sample until the soil is saturated. The amount of water that is discharged from the soil and the water mixture of time in a measured length are used as an input to a formula used to determine the soil permeability. The length of time used in the test can vary, but should be consistent during all tests performed for one location. The permeability rate is listed in Table 5.3 for 5 runs of experiments, as well as for the clayey layer of the model.

### 5.3.9 Compression Test

A common method of conducting the test, as described in several published standard test methods, is to compress a box at a constant rate of 12.5 mm per minute between two rigid platens. The platens can be fixed so that they remain parallel or one can be pivoted or “floating”. The test can be conducted on empty or filled boxes, with or without a box closure.

The measurement of the compression test of Zhuankou clay resulted in the compression factor $a_{v1\text{-}2}$ is 0.265 $MPa^{-1}$, and the compression modulus $Es_{1\text{-}2}$ is 62.30 MPa.

## 5.4 Flume Tests

### 5.4.1 Measurement Instrumentation

In the breaching process of cohesive embankments, the morphological changes depend on the hydraulic parameters; conversely, the morphology influences the hydraulic parameters. Therefore the hydraulic and morphological parameters both play an important role in the breaching process. In the present flume tests, the water levels were measured with water level meters, and flow velocities with electromagnetic velocity meter. ADV was also used in the tests. The topography was measured with a 3D laser scanner and with video cameras.

Eight water level meters (see Fig. 5.17) were setup along the flume from the inlet of the channel to the tailgate (see Fig. 5.1). Four meters were fixed to measure the water level changes upstream of the embankment. Two meters were used to measure the water levels just above the crest of the embankment and in the initial channel of the embankment. Downstream of the embankment, one meter was used to measure the water level and one meter to control the tailgate water level.

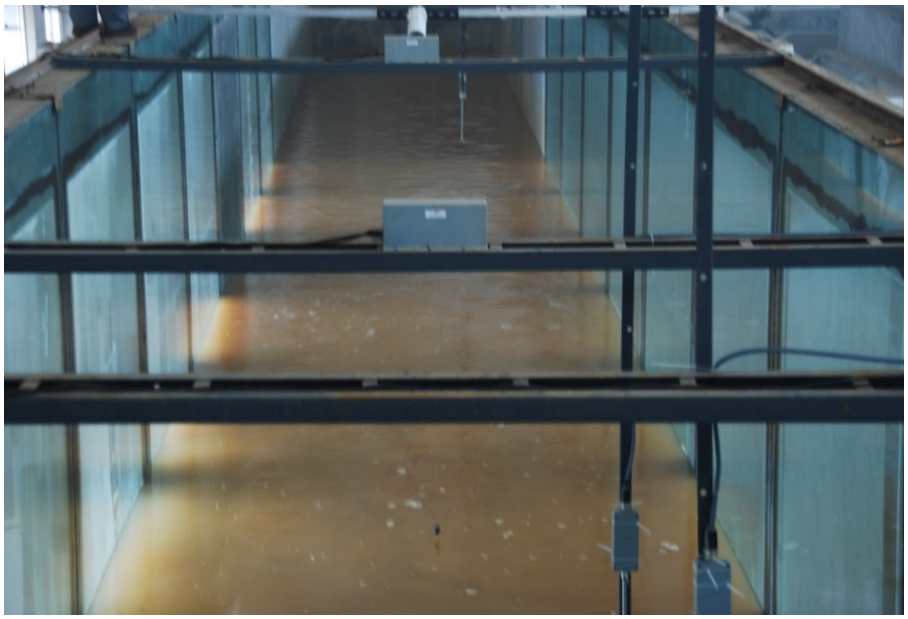

**Figure 5.17 Water level meter**

Three electromagnetic velocity meters were fixed upstream of the breach, in the breach channel and downstream of the breach to measure the flow velocities (Fig. 5.17). Particle tracing was used to indicate the velocity distribution at the flow surface, while the three high-speed video camera systems recorded the breaching process. According to the video records, the surface velocity could be measured and calculated using the traced particle movements.

A 3D laser scanner (see Fig. 5.18) was used to measure the breach geometry variation, every 5 minutes. The scour hole and the breach channel development were measured and recorded with topography survey instruments and video cameras through the glass wall of the flume.

**Figure 5.18 Three dimensional laser scanner systems**

### 5.4.2 Boundary Conditions

Five experimental runs were conducted in the flume and the embankment models were built according to the designs (see Fig. 5.1 and Table 5.1). Run 1 (the test with Model 1) was conducted February 1, 2013; Run 2, Run 3, Run 4 and Run 5 (the tests with Model 2, Model 3, Model 4 and Model 5, respectively) were conducted on February 27, March 7, March 14 and March 22, 2013, respectively.

The upstream boundaries for each run of the experiments were controlled by the discharge and the water level. The front water level of the embankment was kept in the submerged condition, i.e. water levels were controlled at 2.00 m for Model 2, Model 3, Model 4 and Model 5, and the water level was controlled at 1.40 m for Model 1. In order to control the water at a semi-constant level, the discharge (Fig. 5.19) was adjusted by the electromagnetic discharge meter.

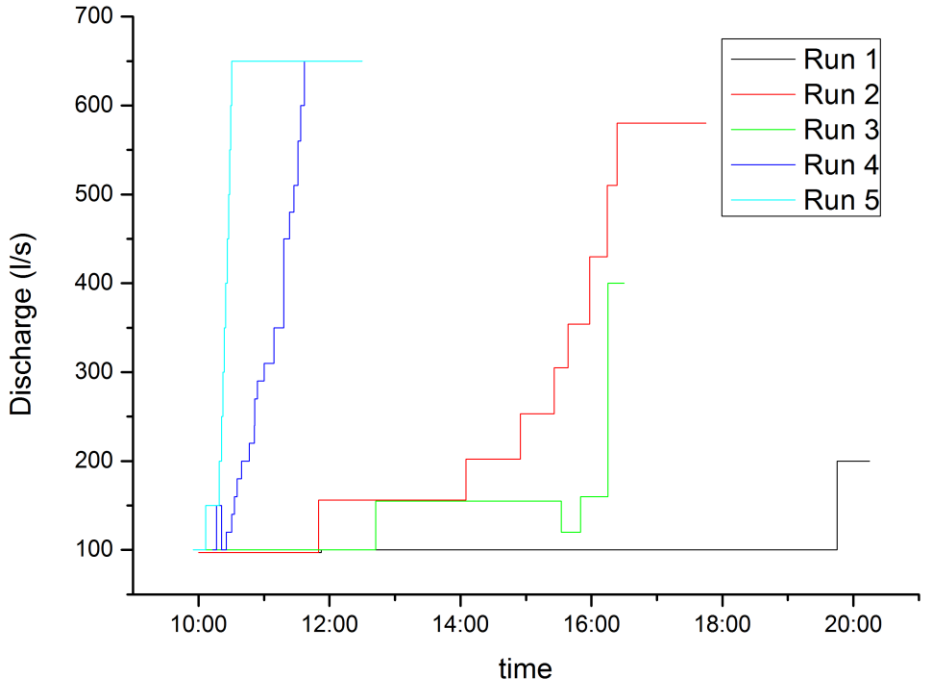


**Figure 5.19 Discharge process for 5 runs of experiments**

In each run of the experiments, the water temperatures and sediment concentrations were measured. The results are shown in Table 5.4. All water temperatures were above 10°C and the sediment concentrations increased from 3.74 g/l in the first run of the experiment to 5.00 g/l in the last run of the experiment since the recycled water was stored in the reservoir.

**Table 5.4 Water temperature and sediment concentration**

| RUN | Water temperature (°C) | Sediment concentration (g/l) |
|---|---|---|
| Run 1 | 10 | 3.74 |
| Run 2 | 15 | 3.88 |
| Run 3 | 13 | 4.56 |
| Run 4 | 10 | 4.86 |
| Run 5 | 13 | 5.00 |

### 5.4.3 Measured Water Levels

In the 5 runs of breach experiments, the water levels were measured and recorded upstream and downstream of the model embankment. There are 9 water level meters (WM1, WM2, WM3, WM4, WM5, WM6, WM7, WM8, and WM9) fixed in the flume (Fig. 5.1). WM1 measured the controlling water level of the flume. WM4 and WM5 measured the upstream water level close to the embankment crest. WM9 controls the tailgate water level. The measured water levels are shown in Fig. 5.20, Fig. 5.21, Fig. 5.22, Fig. 5.23, and Fig. 5.24, as function of time $t$ ($t$=0 at the start of the experiment).

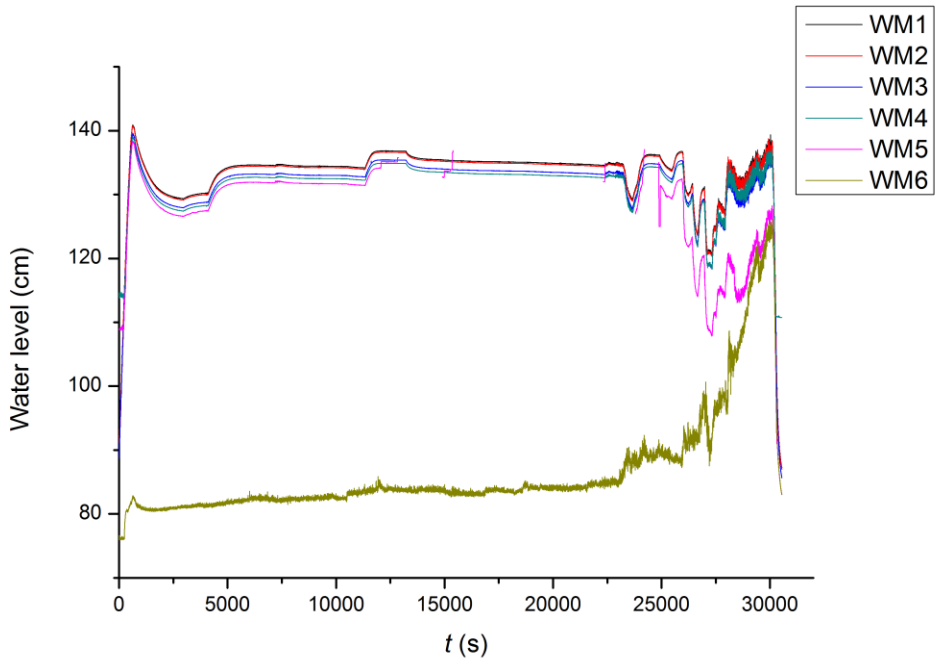


**Figure 5.20 Water levels measured in Run 1**

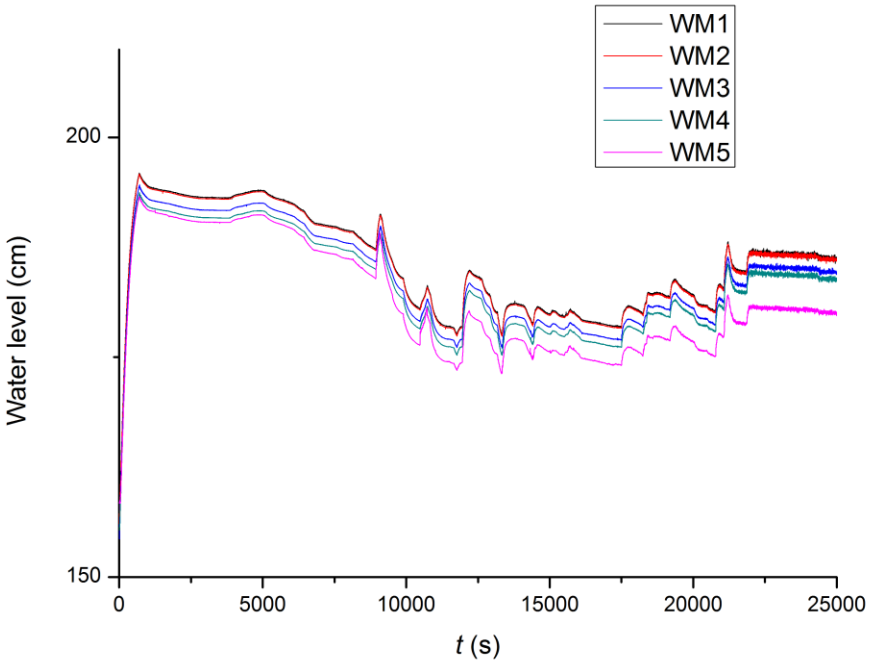


**Figure 5.21 Water levels measured in Run 2**

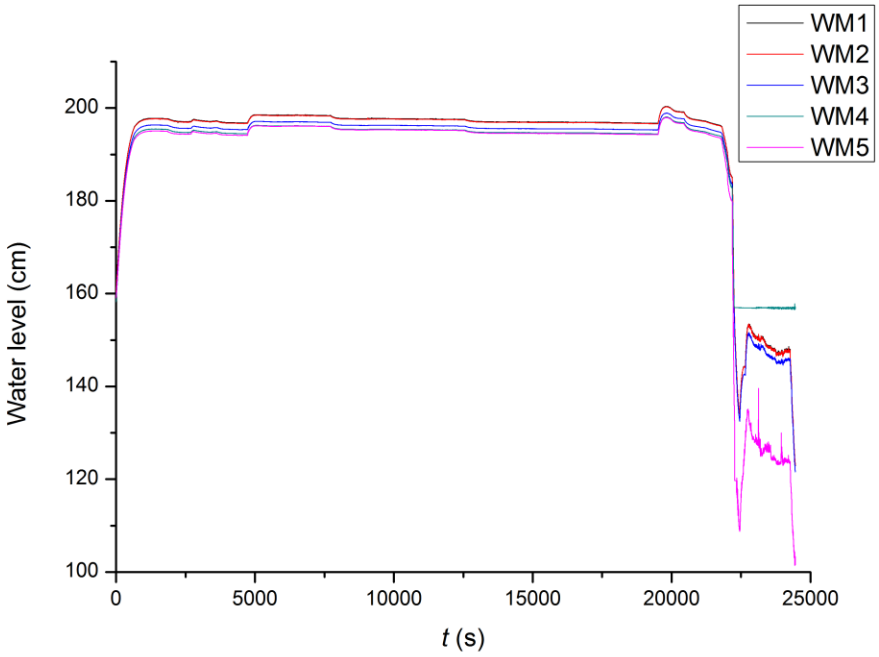


**Figure 5.22 Water levels measured in Run 3**

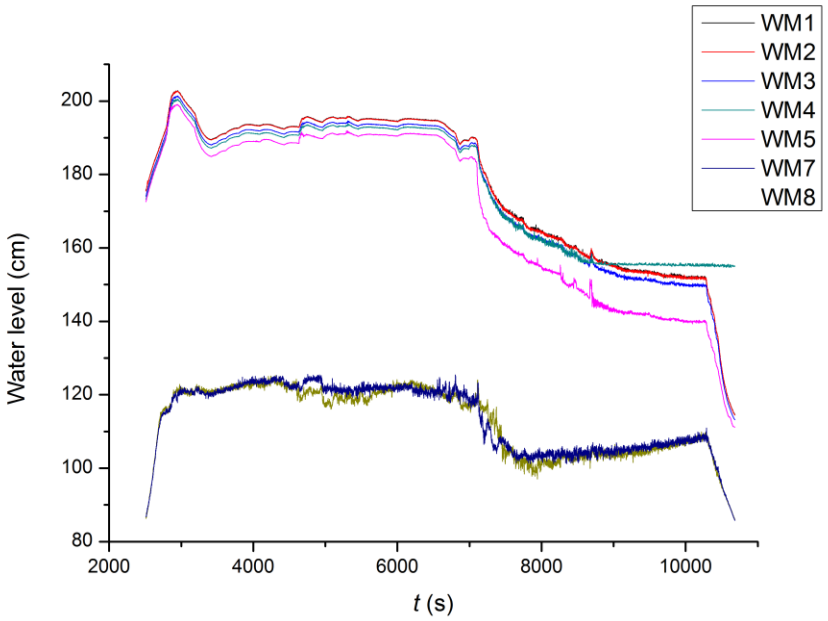


**Figure 5.23 Water levels measured in Run 4**

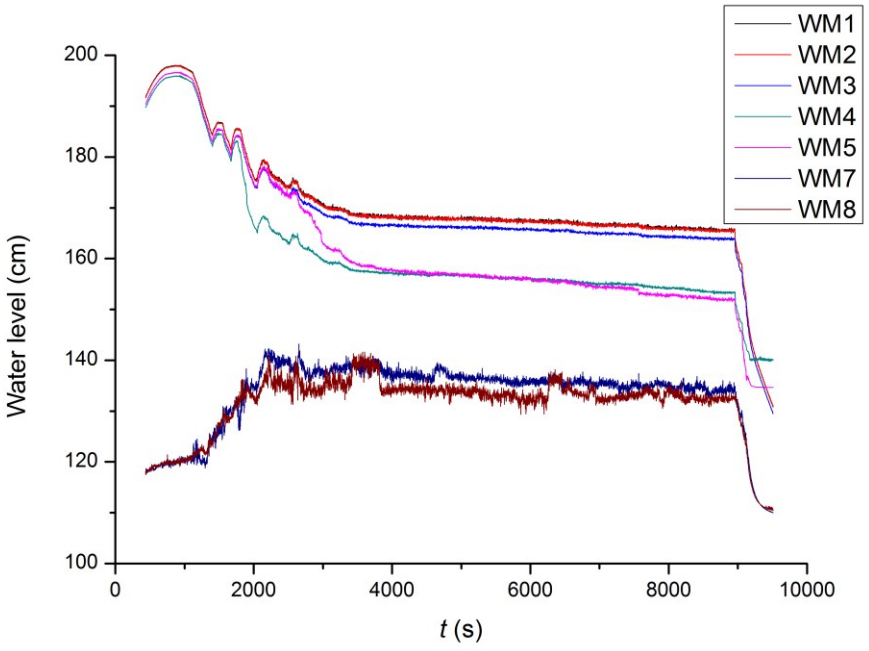


**Figure 5.24 Water levels measured in Run 5**

### 5.4.4 Morphological Processes in the Breach

Morphological processes play an important role in the breaching process of cohesive embankments. The morphological changes are the results of the erosion triggered by the breach flow. In these experiments, the morphological process was measured every 5 minutes by a 3D scanner. In this section, Run 4 with Model 4 is taken as an example to describe morphological changes in the breach development process.

Before the experiment started, the total topography of the flume model was scanned (Fig. 5.25). In the five runs of the experiments, Model 4 had an initial breach channel at the side of the flume, and when the flow came from the upstream and went through the initial channel, the breaching process started. The surface erosion happened due to the high flow velocities supplied by the flow from the reservoir (Fig. 5.26). The flow first broke the embankment surface and then washed away blocks of the model material, but not as single particles.

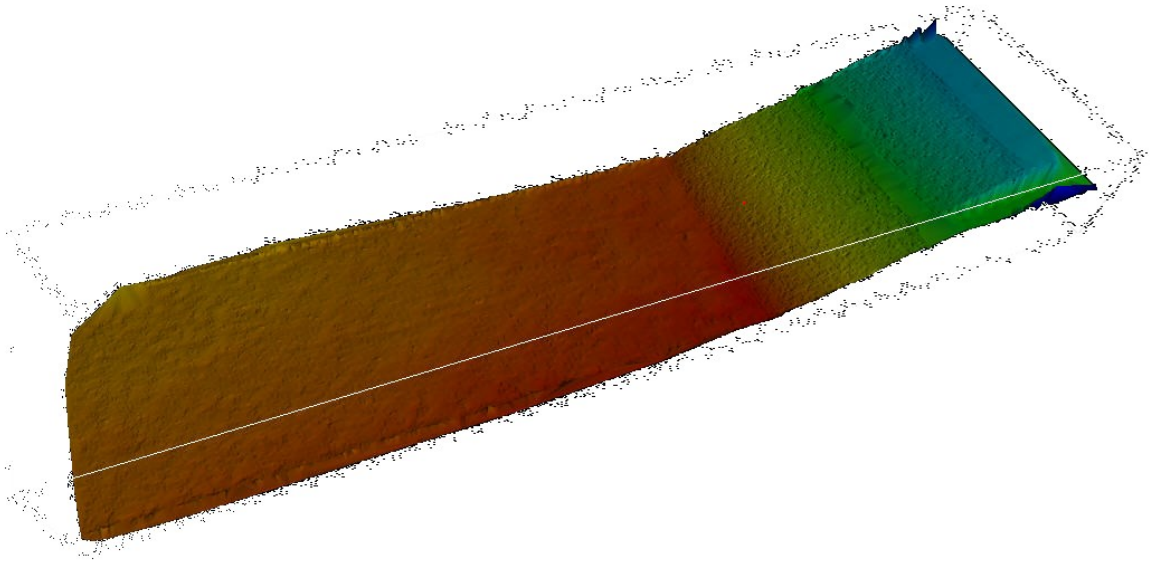

**Figure 5.25 Topography of the model before the test (Model 4)**

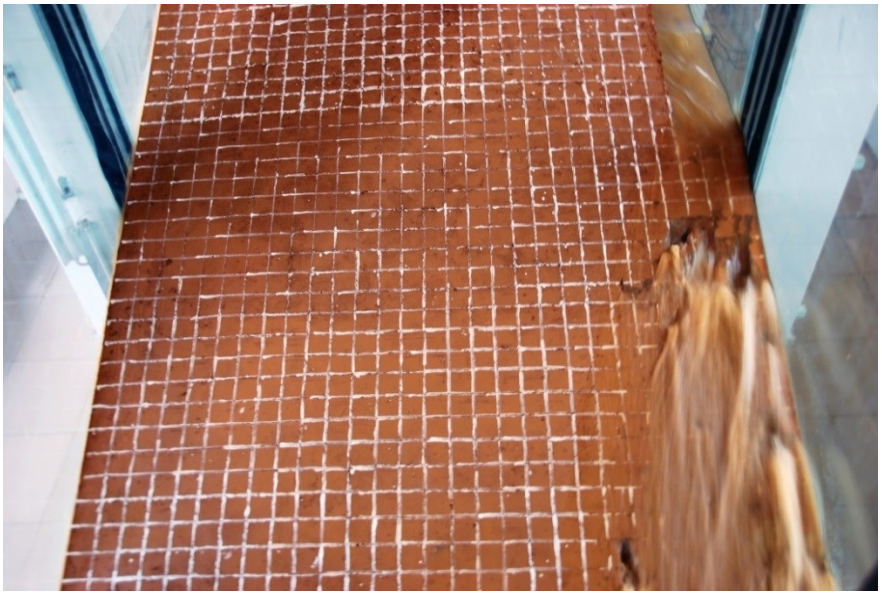

**Figure 5.26 Surface erosion at the initial phase of breach (Run 4)**

As the breach developed, the cascade headcut erosion started to develop from the toe of the embankment after the full completion of the surface erosion on the model surface (see Fig. 5.27). The blocks of the clay were washed out by the high flow velocity in the breach. The width of the initial breach channel increased to 1.02 m stimulated by the breach flow and the embankment toe was fully eroded by the headcut erosion (Fig. 5.28).

**Figure 5.27 Photo of headcut erosion in Run 4**

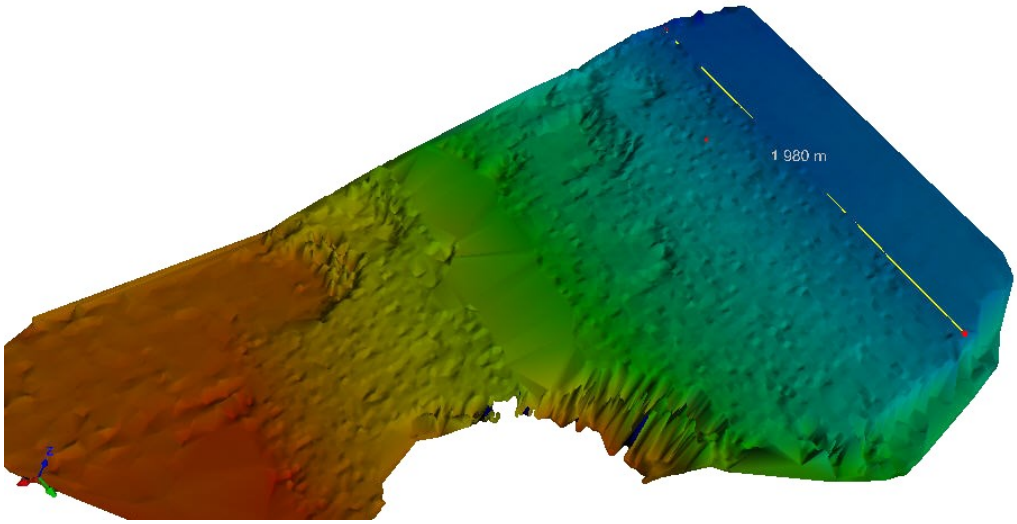


**Figure 5.28 Topography change during the test of Run 4**

The lateral erosion started to play an important role in the breaching process when the development of the headcut erosion progressed. Due to the helicoidal flow (secondary flow) in the breach channel, the undermining process triggered the erosion at the toe of the side slope of the embankment (Fig. 5.29). The lateral erosion at the toe of the side slope broke the balance of the embankment and the material blocks collapsed due to the unbalanced situation of the embankment. The lateral erosion stimulated the lateral development of the breach channel and immediately increased the breach width. Due to the cohesion of the material, the lateral breach slope became very steep. The undermining process at the toe of the side slope of the breach channel usually caused the breach slope to become negative (Fig. 5.30).

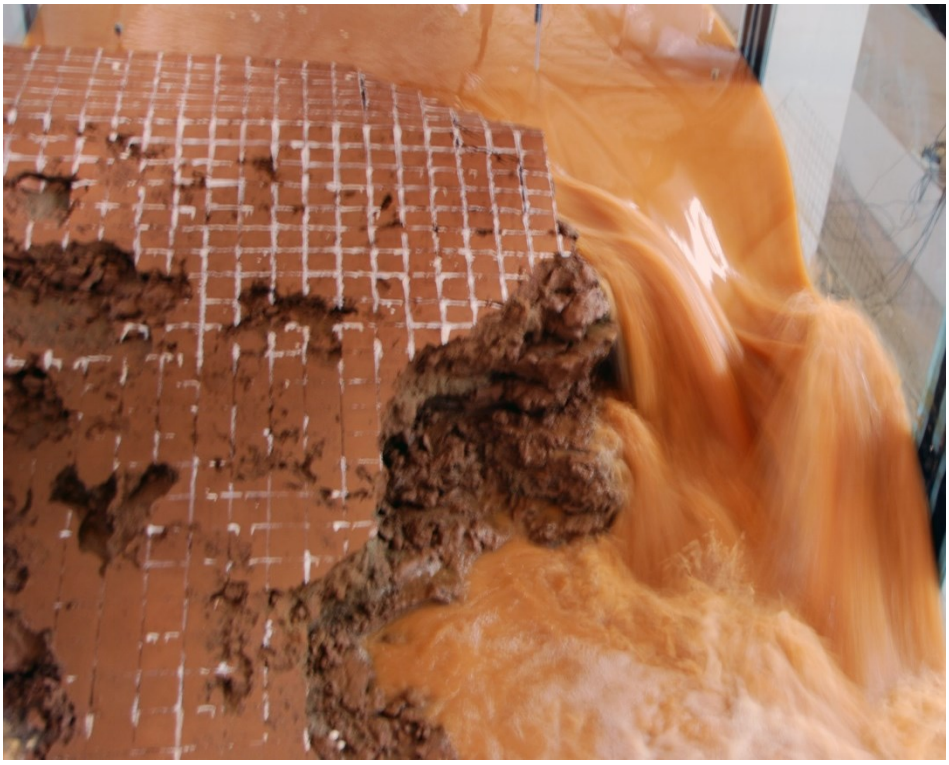

**Figure 5.29 Lateral erosion of the breach in Run 4**

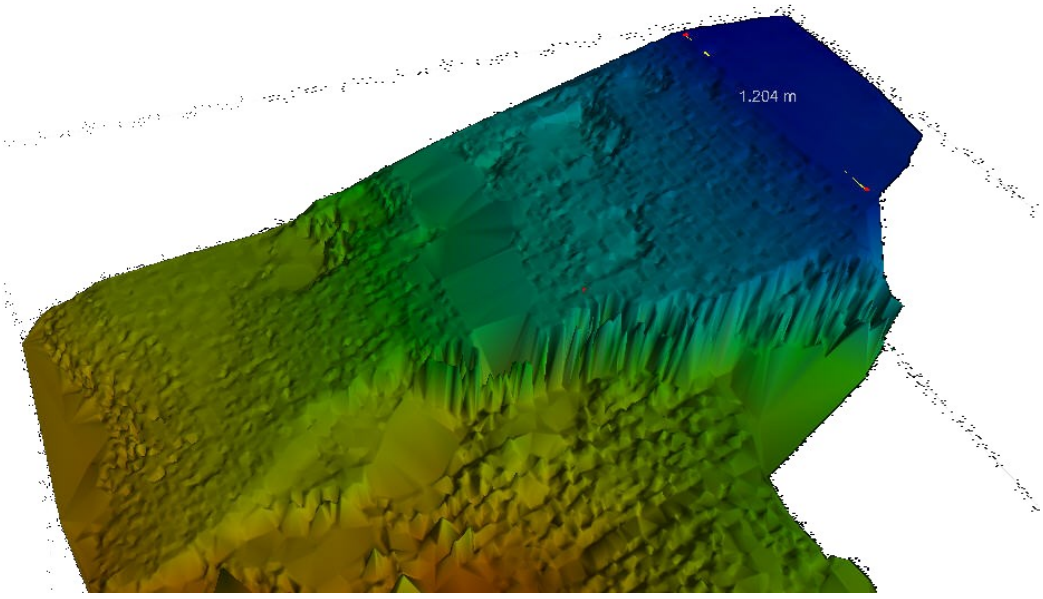


**Figure 5.30 Steep breach side slope of Run 4**

After the initial surface erosion, the embankment breaching process was driven by headcut erosion and lateral erosion. Due to the high velocity of the flow through the breach, a scour hole developed in the breach channel and at the toe of the embankment (Fig. 5.31). The scour hole near the embankment toe started to form in the early stage of the breaching process, but the eroded material from the embankment covered the scour hole during the following phases of the breaching process. The scour hole formed at the bottom of the embankment in the last phase of the breaching and the eroded material was washed away towards the downstream.

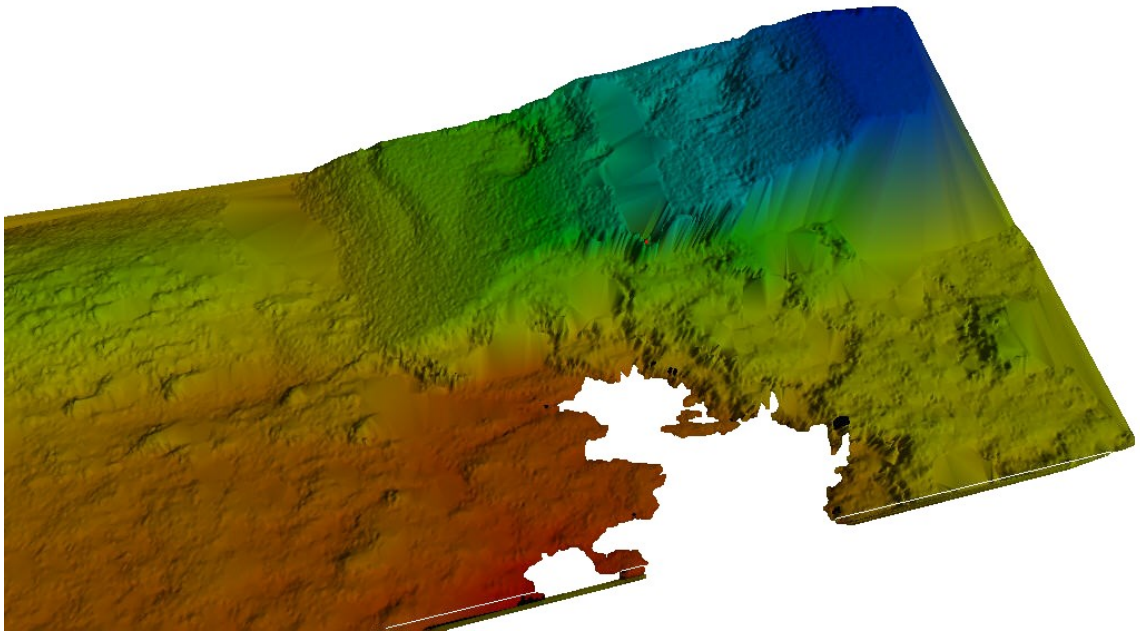

**Figure 5.31 Final scour hole of breach of Model 4**

The typical breach topography was formed by the breach flow and by the breach erosion. The headcut erosion contributed to the longitudinal development of the breach and the lateral erosion stimulated the breach to become wider and wider, and finally stopped when the breach flow was too small to erode the embankment material. The scour hole developed at the toe, but disappeared due to deposition of sediment from the breach. At the embankment site, the breach flow eroded the bottom and formed a scour hole there

(Fig. 5.32). The embankment breaching stopped when the upstream water level was equal to the downstream water level.

The deposition occurred during the breaching process (Fig. 5.30 and Fig. 5.31). Since the velocity at the downstream of the un-breached side of embankment was very low compared to the flow velocity downstream of the breach, the sediment was deposited in the channel. The deposited sediment was distributed at the downstream of the un-breached embankment and formed a sediment belt.

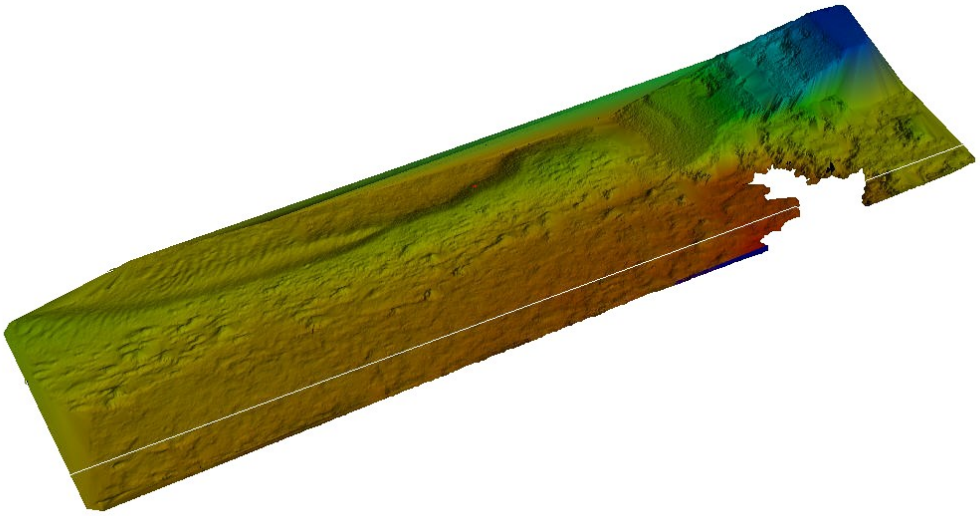

**Figure 5.32 Final topography of Model 4**

**Figure 5.33 Final topography of Model 4 from the downstream overview**

The breach channel was 2.50 m wide and the side slope of the breach was very steep with negative values at several locations, due to the undermining process of lateral erosion (Fig. 5.34). The material of the front embankment was eroded by the upstream convergent flow. The upstream breach width was larger than the downstream breach width, e.g. 0.21 m in Model 4.

**Figure 5.34 Final topography of Model 4 from the upstream overview**

### 5.4.5 Headcut Migrations and Lateral Migrations

The headcut migrations for Run 1, Run 2, Run 3 and Run 4 are shown in Fig. 5.35, Fig. 5.36, Fig. 5.37, Fig. 5.38, respectively, as function of time $t$ ($t$ = 0 at the start of the experiment). It can be seen that the headcut migration is not a linear process.

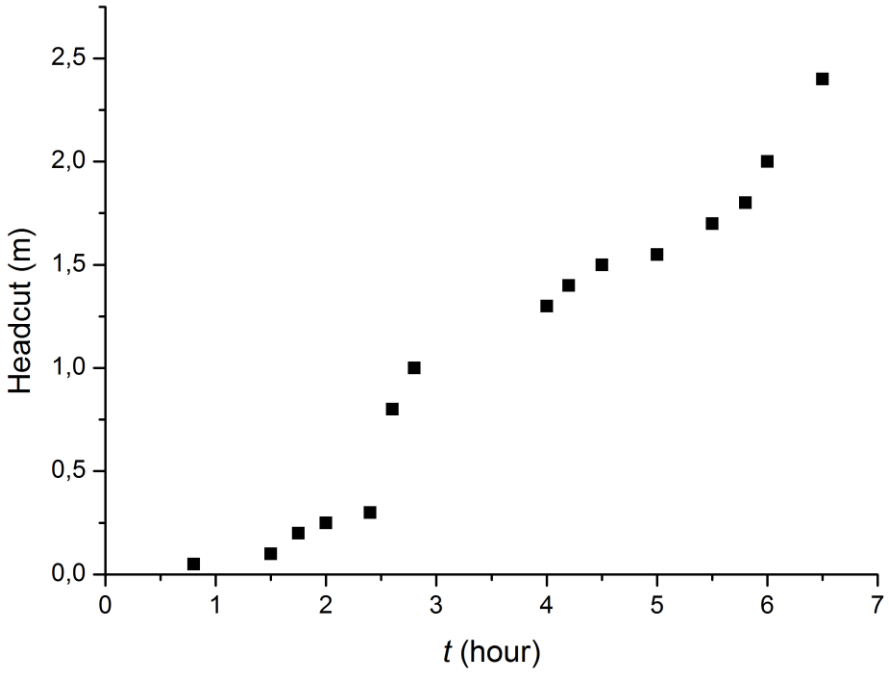


**Figure 5.35 Breach headcut migrations in Run 1**

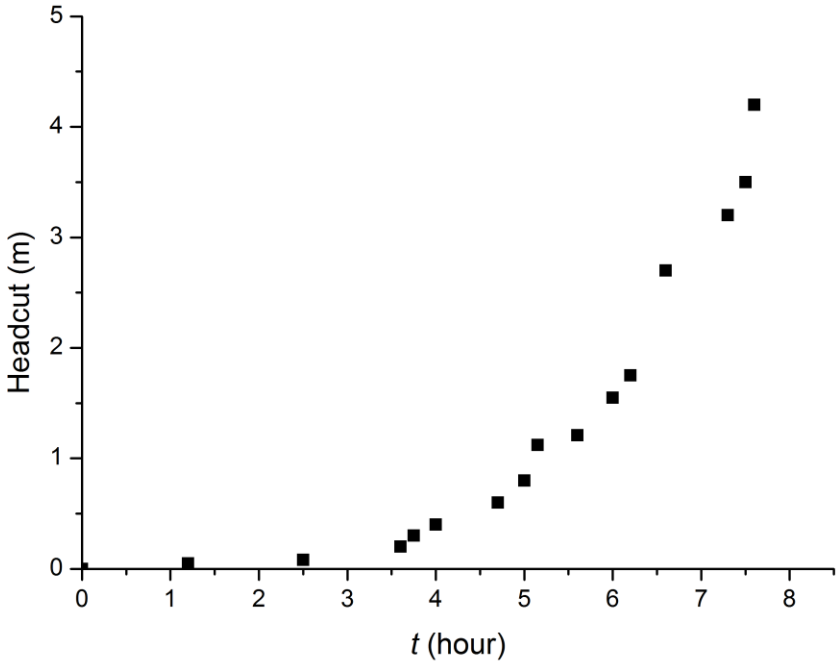


**Figure 5.36 Breach headcut migrations in Run 2**

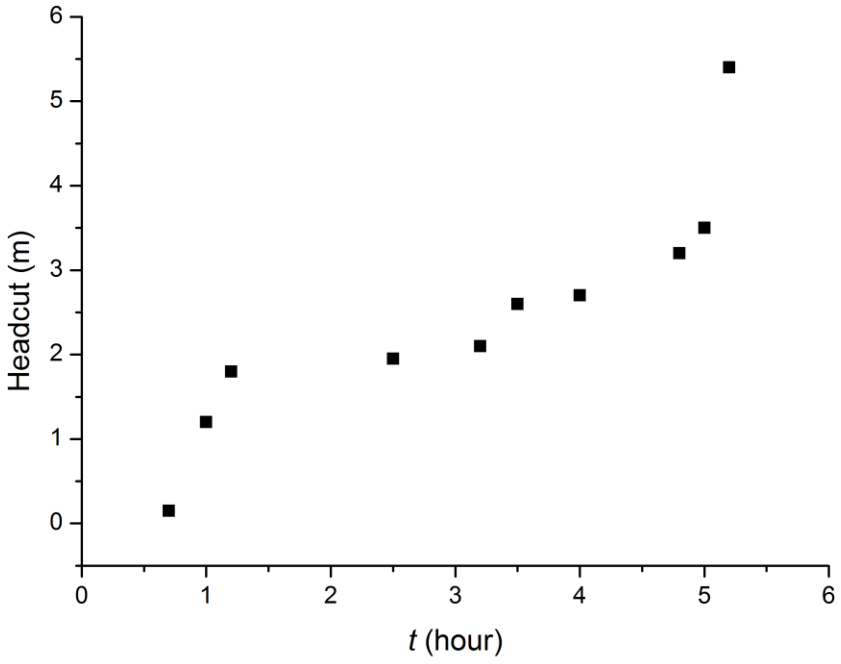


**Figure 5.37 Breach headcut migrations in Run 3**

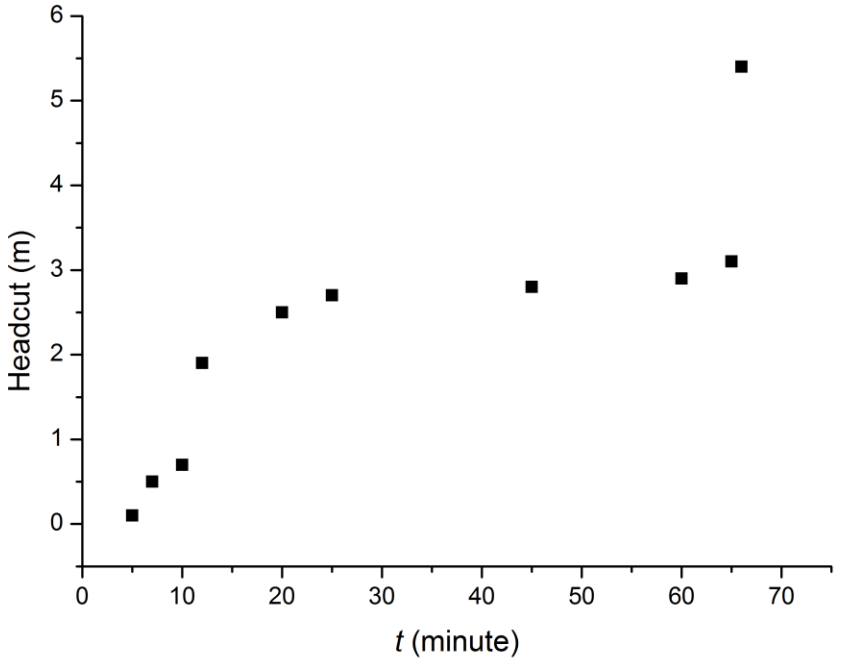


**Figure 5.38 Breach headcut migrations in Run 4**

The lateral migrations for Run 1, Run 2, Run 3, Run 4 and Run 5 are shown in Fig. 5.39, Fig. 5.40, Fig. 5.41, Fig. 5.42, Fig. 5.43, respectively ($t$ = 0 at the start of the experiment).

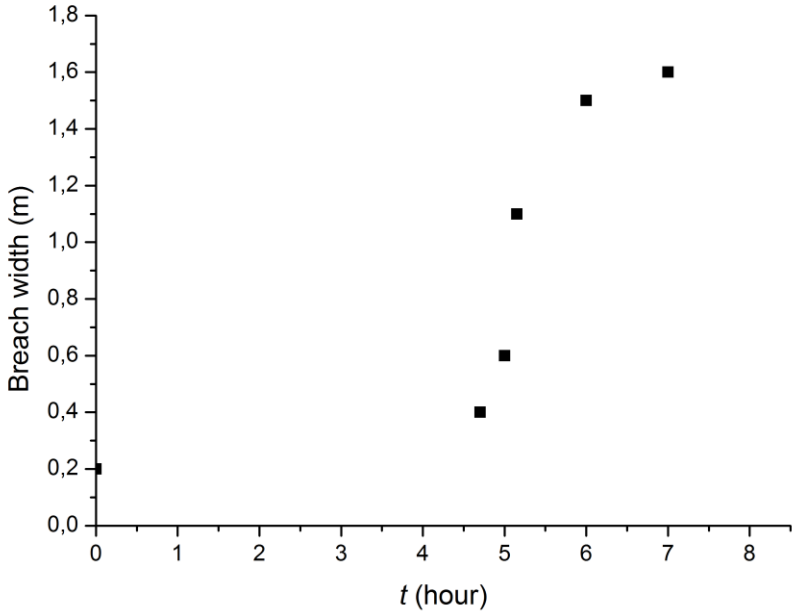


**Figure 5.39 Breach lateral migrations in Run 1**

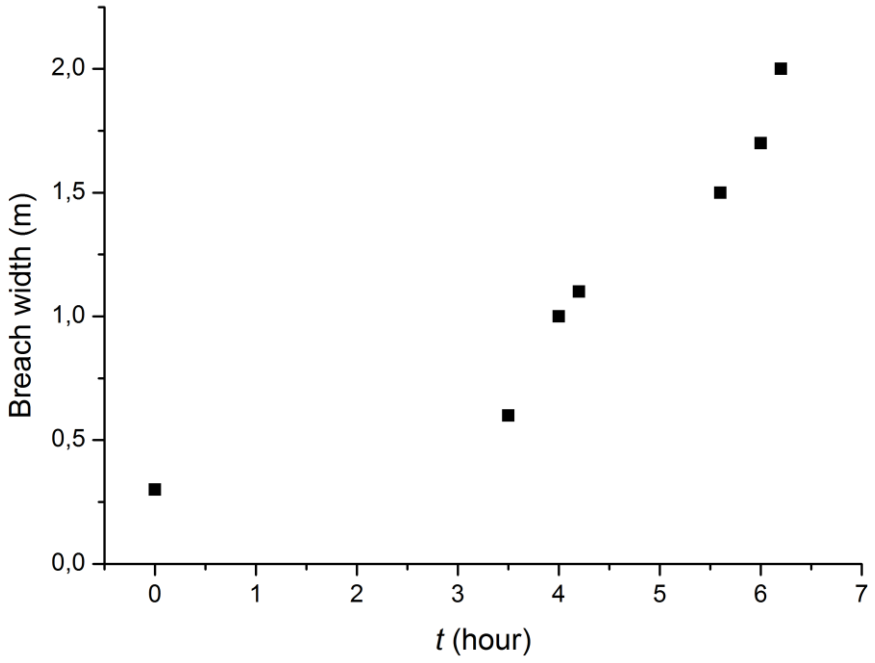


**Figure 5.40 Breach lateral migrations in Run 2**

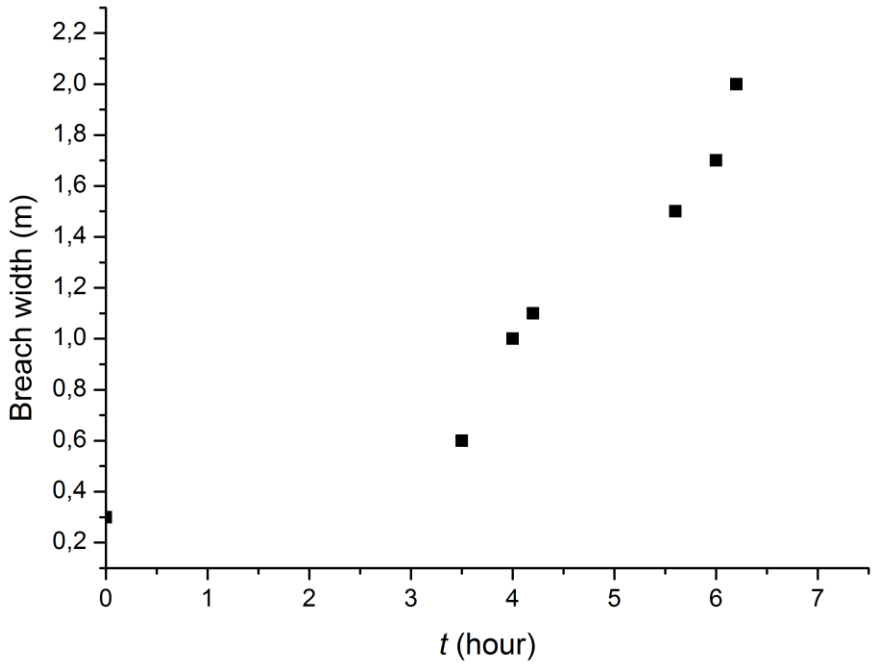


**Figure 5.41 Breach lateral migrations in Run 3**

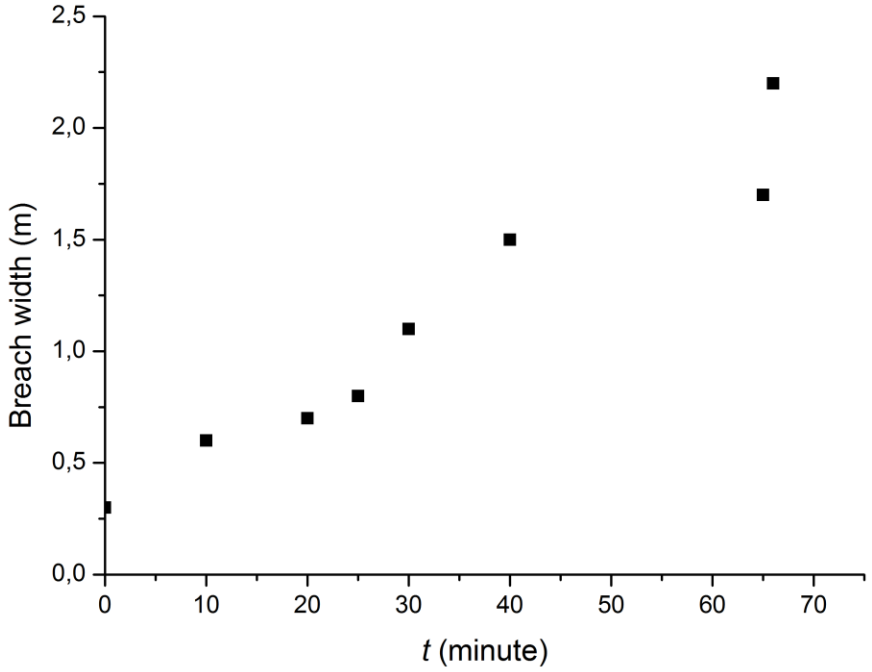


**Figure 5.42 Breach lateral migrations in Run 4**

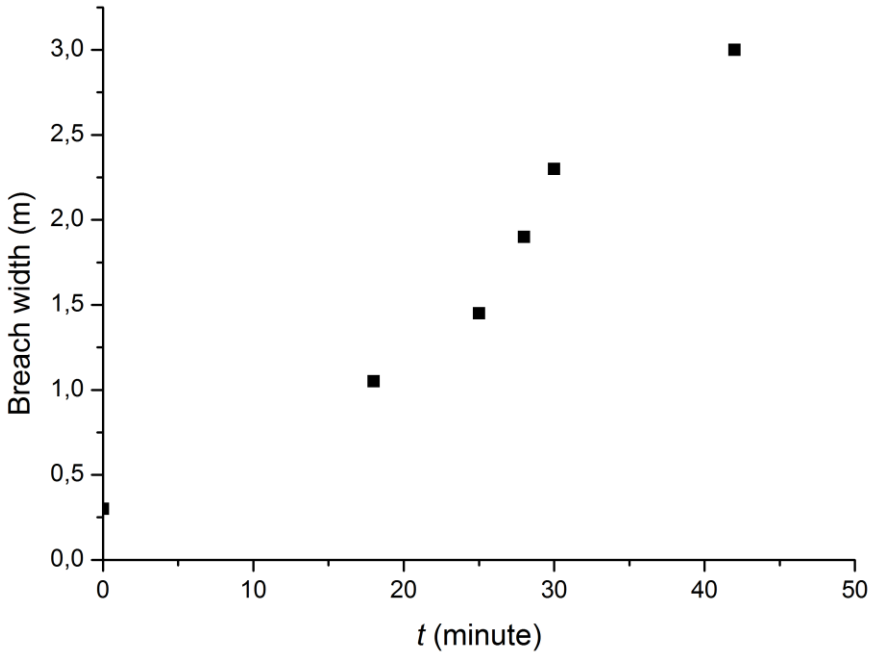


**Figure 5.43 Breach lateral migrations in Run 5**

## 5.5 Discussion

In this chapter five runs of breach experiments, which were conducted in a relatively large flume, are described. The experimental results strongly support the hypothesis that cohesive embankment breaching is a hydrodynamic process coupled with soil mechanics. The breaching starts with the initial erosion of the embankment surface and, then wash away the embankment surface. Due to the surface erosion at the toe of the embankment, the headcut erosion is stimulated on the embankment slope. The headcut erosion can also develop into cascade headcut migration, due to the non-homogenous characteristics of the embankment material (Hanson, *et al*., 2001). While headcut migration stimulates the breach to develop in longitudinal direction, the lateral erosion triggers the breach to widen in lateral direction. Three types of erosion (surface erosion, headcut erosion and lateral erosion) contribute to the erosion process of the breaching in the embankment, however, the breach flow is the driving force for the erosion. Sediment deposition in the breaching process can be of importance, but is generally ignored in the embankment breaching studies. Due to scale effects, the small-scale breach model cost more breaching time than the larger ones.

# Chapter 6 Mathematical Model for Embankment Breaching

## 6.1 Introduction

Embankment breaching is a complex process of flow motion, sediment incipient motion and sediment transport. This applies in particularly to the breaching of cohesive embankments. In this chapter a mathematical model is developed to couple breach flow (Chapter 3) and breach erosion (Chapter 4).

The proposed model is based on the 'state of the art' and gains new concepts from past research (Chapter 2). The model focuses on detailed flow characteristics and erosion processes, respectively. The study is supported by large-scale flume experiments and field surveys as well as the available data analysis from former projects (Visser, 1998; Zhu, 2006; Morris *et al*., 2009). A numerical model is developed, improved, validated and calibrated via sources from the 'state of the art' (Zhu, 2006; Liu *et al*., 2009) and the data collected in Chapter 5 of the present study.

## 6.2 Breach Model in Cohesive Embankments

### 6.2.1 Model Scheme

Erosion functions as the link between breach flow and the embankment material (Fig. 6.1). Surface erosion starts in the initial breach phase and triggers the initial damage of the embankment (Fig. 6.2 (a)). As the surface erosion develops fully, the headcut erosion leads the breaching process by cutting the embankment slope and in the end by deepening the crest level (Fig. 6.2 (b) and Fig. 6.3). The lateral erosion undermines the side slopes of the breach and widens the breach in lateral direction by triggering the breach side slope to collapse (Fig. 6.4).

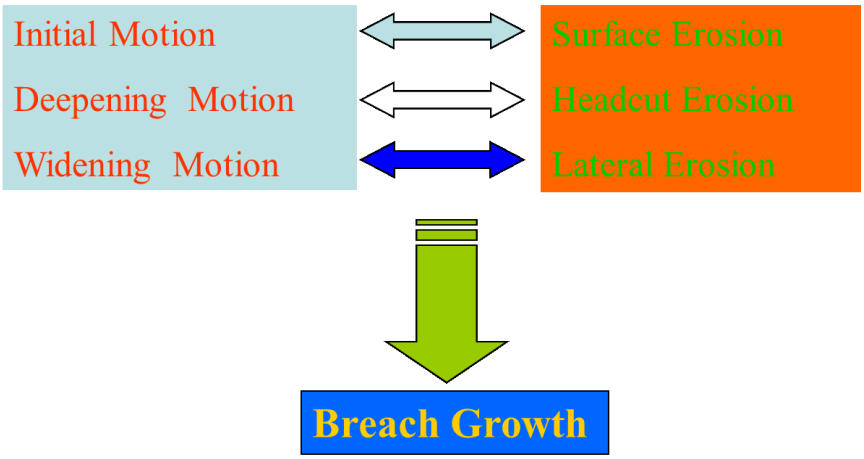


**Figure 6.1 Scheme of breach model coupling flow and erosion**

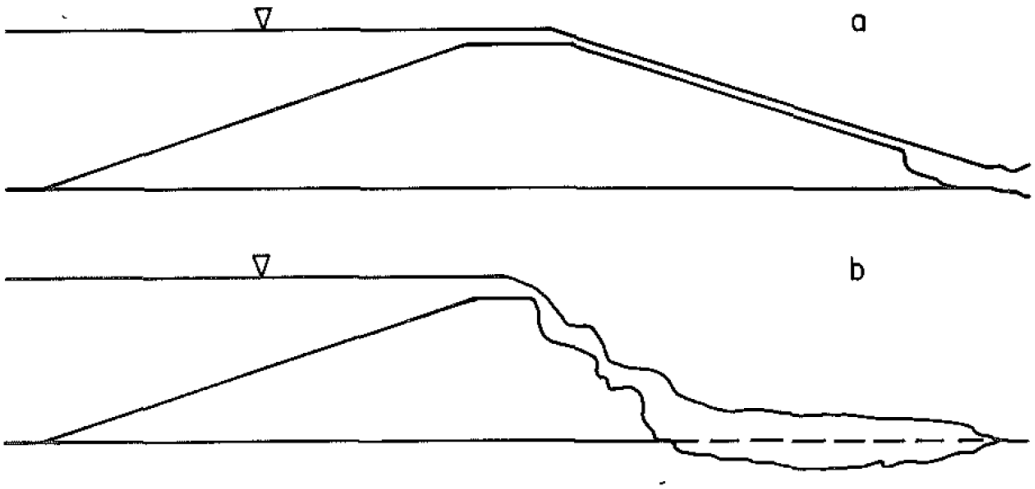


**Figure 6.2 Breach developments in cohesive embankments**

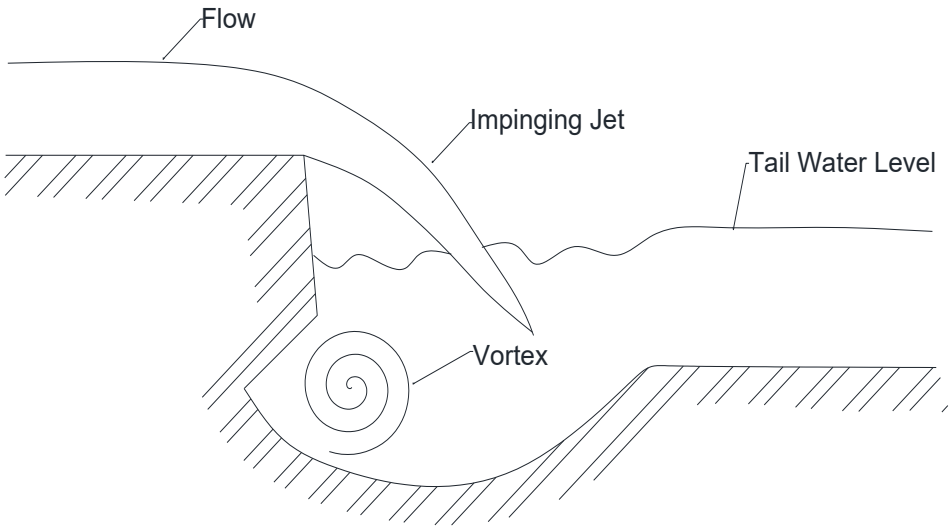


**Figure 6.3 General sketch of headcut erosion with scour hole (side view)**

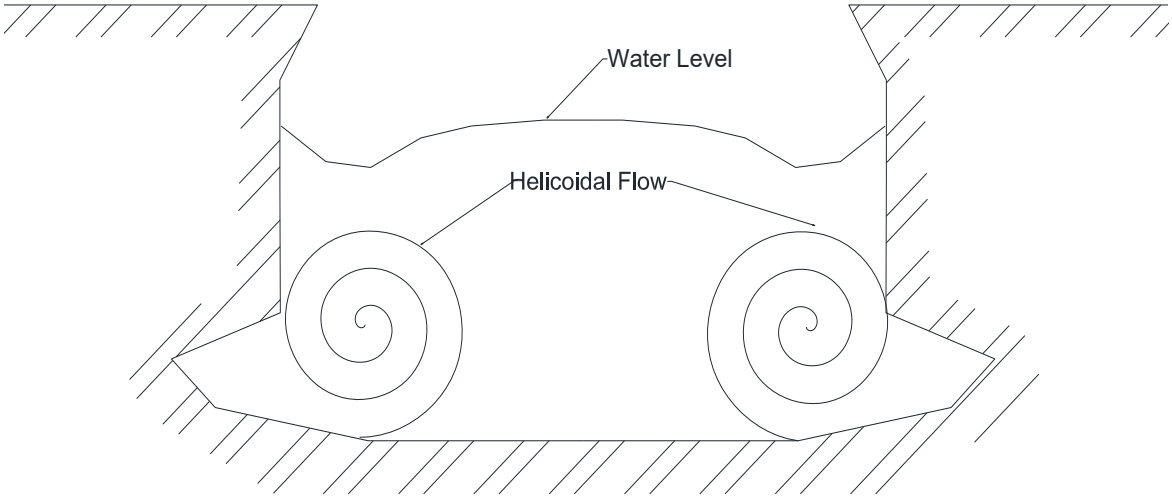


**Figure 6.4 General sketch of lateral erosion due to helicoidal flow (front view)**

The breach model includes 4 modules: (1) the breach flow module, (2) the surface erosion module, (3) the headcut erosion module and (4) the lateral erosion module. The first model input is the upstream water level $H_0$, which is used to calculate the breach flow discharge and the breach velocity (see Section 6.2.2). The second input is clay shear strength $\tau_f$, which is used to calculate the critical Shields parameter and the critical shear

stress $\tau_{Cc}$ (see Section 6.2.3). The third input is the assumption of the toe erosion length of headcut $T_0$, which is applied to the headcut erosion module to calculate the headcut migration rate (see Section 6.2.5). The forth input of the model is the assumption of the toe erosion length of breach side slope $W_0$, which is applied to the lateral erosion module to calculate the lateral migration rate (see Section 6.2.6). When the first model input (the upstream water level) changes, the whole breach model should be restarted from the breach flow module, followed by the headcut erosion module and the lateral erosion module. The headcut erosion model will stop, when the headcut migration length reaches the length of the base of the dike. Similarly, the lateral migration module will stop when downstream water level equals the upstream water level. The headcut and the lateral migration rate both depend on the upstream water level of the breach, i.e. the headcut and the lateral migration rate remain constant when the upstream water level is constant, but both rates will change with the upstream water level, when the upstream boundary condition changes.

### 6.2.2 Breach Flow Module

Due to the lateral constraint from the breach shape, the breach flow can be seen as a type of compound flow in the breach model. In the cohesive embankment breaching process, the breach side slopes are very steep, sometimes even with minus values. Therefore the cross-section shape of the breach is supposed as a rectangular and/or trapezoidal shape. The weir flow in a rectangular breach can be expressed as

$$Q = C_d \frac{2}{3} b \left( \frac{2}{3} g \right)^{1/2} H_0^{3/2} \tag{6.1}$$

where $C_d$ is the weir discharge coefficient, $b$ is the width of the lower weir crest, $H_0$ is the upstream energy head above the embankment.

When the breach channel has a trapezoidal shape, the breach discharge formula (Bos, 1989) can be written as

$$Q = C_d \left( b d_c + m d_c^2 \right) \left[ 2g \left( H_0 - d_c \right) \right]^{1/2} \tag{6.2}$$

where $m$ is the side slope, $b$ is the width of breach bottom, $d_c$ is the water depth above the weir and approximately equals $\frac{2}{3}H_0$ in the critical weir flow condition (Visser, 1998). The discharge formulae Eq. (6.1) and Eq. (6.2) can be chosen based on the assumption of the breach channel shape. In this research, an initial breach channel shape was given, thus the initial wet area $A$ can be calculated. Therefore the depth-averaged flow velocity in the breach can be calculated as follows

$$v = \frac{\mathrm{Q}}{\mathrm{A}} \tag{6.3}$$

### 6.2.3 Surface Erosion

The initial phase of the breaching process in cohesive embankments is determined by surface erosion (see Section 4.2 in detail). The incipient motion of the clay blocks can be calculated with the breaching velocity from Eq. (6.3) by the new Shields parameter formula as

$$\frac{\tau_{Cc}}{(\rho_s - \rho)gD_b} = C\frac{\tau_f}{\rho v^2}\theta_c \tag{6.4}$$

where $\theta_c$ is the critical Shields parameter of non-cohesive sediment, $\rho_s$ is the density of clay, $\rho$ is the density of water, $\tau_{Cc}$ is critical shear stress of the non-cohesive sediment particle's incipient with the same size, $D_b$ is the diameter of the clay blocks, $\tau_f$ is the shear strength measured in the soil mechanics laboratory, v is the flow velocity over the embankment surface, and $C$ is an empirical parameter. In the present study, the size of the clay blocks can be approximated as the multiples of the clay median diameter (e.g., $10D_{50}$, $20D_{50}$, $30D_{50}$, etc.), depending on the clay types.

### 6.2.4 Clay Erosion Rate

The erosion rate can be predicted by the maximum time-averaged hydraulic shear stresses in the vertical and in the horizontal direction. According to the dimensionless analysis, the erosion rate can be expressed with an excess stress equation (Hanson *et al.*, 2001)

$$\varepsilon = \zeta(\tau_e - \tau_c)^n \tag{6.5}$$

where $\varepsilon$ is the erosion rate, $\zeta$ is the erodibility coefficient, $n$ is an empirical parameter, and $\tau_e$ is the effective stress:

$$\tau_e = \rho g d_t s \tag{6.6}$$

where $d_t$ is the water depth at the toe of the embankment, $s$ is the landside slope of the embankment.

### 6.2.5 Headcut Erosion Module

Headcut erosion (see Section 4.3 in detail) is a hydrodynamic erosion process (Fig. 6.5) in the breaching of a cohesive embankment. In the model it plays an important role of simulating the breaching in the longitudinal direction.

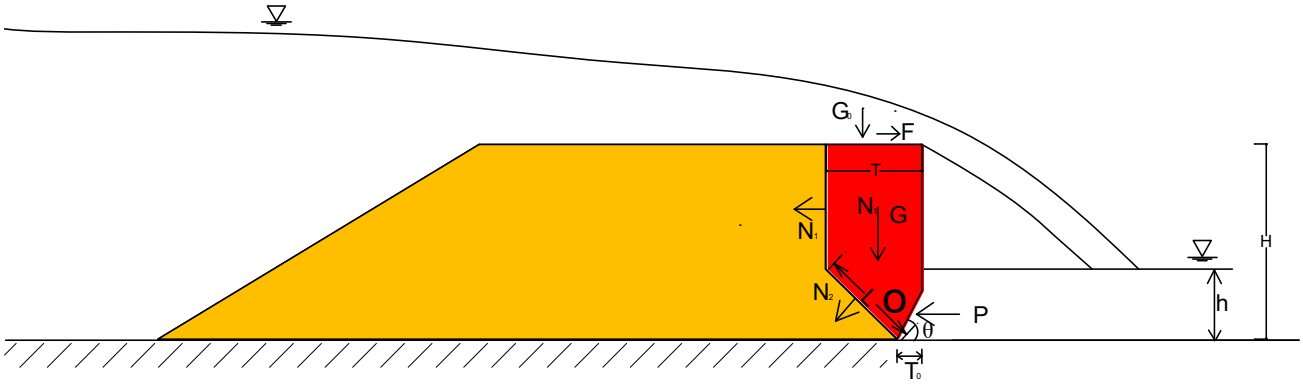


**Figure 6.5 Sketch of headcut migration**

In Section 4.3, applying the moment principle, a moment equation has been obtained as follows

$$\begin{aligned} M &= F(T, T_o, G_0, N_1, N_2, G, P) \\ &= \mathrm{F}\cdot \mathrm{H} - G_0 \cdot (0.5T - T_0) - N_1 \cdot 0.5(H + T - T_0) \\ &- \mathrm{N}_2 \cdot \left[0.5(T - T_0)/\sin\theta\right] + G \cdot \left[ H \frac{(3H - T + T_0)}{3(2H - T + T_0)} - T_0 \right] \\ &- P \cdot \frac{1}{3} h \end{aligned} \tag{6.7}$$

In the headcut developing process, water weight $G_0$, flow stress $F$ and tail water pressure $P$, headcut block weight $G$ and embankment cohesion forces $N_1$ and $N_2$ are generally kept at constant values.

According to Eq. (6.7), the relationship between $T_0$ and $T$ can simply be written as

$$T_0 = f(T) \tag{6.8}$$

The headcut migration model is developed in Section 4.3 to predict the key procedure of the cohesive embankment breach as follows

$$\frac{dx}{dt} = \frac{T}{f(T)}\varepsilon \tag{6.9}$$

where headcut migration rate $\frac{dx}{dt}$ can be described with headcut movement $T$ and the time interval $t$, Eq. (6.8) can be iterated and gets a deterministic $T$ and $f(T)$. In the calculation, $T_0$ is first given an empirical value, e.g., $T_0 = 0.1$. The embankment block fails and the headcut advances when the vertical erosion exceeds a certain amount and the base of the embankment cannot ensure the potential failure of the embankment block. The time interval of failures is monitored by the erodibility and strength of the embankment. The impinging jet stimulates the erosion on the vertical toe of the headcut face, which triggers the embankment to fail in the way of collapsing embankment blocks.

### 6.2.6 Lateral Erosion Module

The embankment blocks collapse due to the undermining erosion at the toe of the breach side slopes (Fig. 6.6). The peak breach outflow can occur during the lateral erosion phase, as the breach opening continues to enlarge under a relatively constant reservoir head.

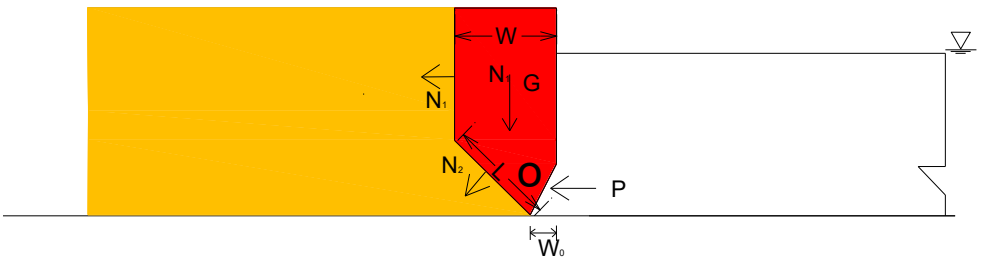


**Figure 6.6 Sketch of lateral migration of embankment breach**

In Section 4.4, the lateral block moment equilibrium has been obtained as follows

$$
\begin{aligned}
M &= F(W, W_o, N_1, N_2, G, P) \\
&= \mathrm{G}\cdot\left[0.5(H + W - W_0)\right] \\
&-N_1\cdot\left[0.5(W - W_0)/\sin\theta\right] \\
&-N_2\cdot\left[H\frac{(3H - W + W_0)}{3(2H - W + W_0)} - W_0\right] - P\cdot\frac{1}{3}h
\end{aligned}
\tag{6.10}
$$

In the development of the lateral erosion, tail water pressure $P$, embankment block weight $G$ and embankment cohesion forces $N_1$ and $N_2$ are generally kept at constant values. The relationship between $W_0$ and $W$ can be given as

$$W_0 = f(W) \tag{6.11}$$

Lateral migration rate can be expressed as

$$\frac{dy}{dt} = \frac{W}{f(W)}\varepsilon \tag{6.12}$$

where the lateral migration rate $\frac{dy}{dt}$ can be described with lateral movement $W$ and time interval $t$, Eq. (6.11) can be iterated and gets a deterministic $W$ and $f(W)$ if $W_0$ is first given a value, e.g. 0.1 m. As the lateral migration develops, erosion occurs at the toe of the breach side slope. The time interval of failures is monitored by the erodibility and strength of the embankment. It is based on the erosion on the vertical toe of the breach slope, which stimulates the breach side slope to collapse.

## 6.3 Discussion

Since the breaching in cohesive embankments is a complicated hydrodynamic process, a mathematical model has been developed by coupling weir flow and types of erosion, i.e. surface erosion, headcut erosion and lateral erosion. The breaching process is simplified into initial motion, deepening motion and widening motion, which corresponds to the surface erosion, headcut erosion and lateral erosion, respectively. In the headcut erosion and lateral erosion, the toe widths $T_0$ and $W_0$ should first be given an empirical value. Then the iteration can be executed to calculate the migration rate. The models of headcut migration and lateral migration rate will be calibrated, validated and applied in Chapter 7.

# Chapter 7 Model Calibration, Validation and Application

## 7.1 Introduction

In this chapter, the mathematical breach model, developed in Chapter 6, will be calibrated and validated with the experimental data from the large-scale embankment breach experiments (see Chapter 5). Model test Run 1 is used to calibrate the headcut migration and the lateral migration of the embankment breach. Run 2, Run 3, Run 4 and Run 5 are used to validate the mathematical breach model.

Breach tests in Delft University of Technology are used to validate the proposed breach model (headcut model). The proposed breach model (lateral migration model) is also applied to simulate the lateral breaching process of the Tangjiashan Landslide Barrier in China, where a pilot channel was dredged to initiate breaching of the natural embankment (Liu *et al*., 2009).

## 7.2 Model Calibrations and Validations

### 7.2.1 Model Calibration

Five large-scale embankment breaching experiments were run in the flume to study the breach erosion process of cohesive embankments (Chapter 5). In the breaching process of cohesive embankments, the headcut and the lateral erosion play an important role in the embankment breach development. The headcut migration model and the lateral migration model (Chapter 4), together with the weir flow formulae (Chapter 3), make up the breach model for cohesive embankments (Chapter 6). In this section, the headcut migration model and the lateral migration model are calibrated with Run 1.

In the erosion model, the erosion rate $\varepsilon$ of the soil material, which is determined by the critical erosion stress $\tau_c$ and effective stress $\tau_e$, is an important parameter, especially for the headcut erosion and the lateral erosion. These values have been determined by Eq. (6.7) and Eq. (6.10) in Chapter 6, as well as by the measured data of soil test in Table 7.1. In this calibration, the shear stress used the direct shear stress test results, since the breaching process completed in a short period (less than 10 hours). In Run 1, the embankment front water level was constant at 1.40 m. The tail gate was fully opened. Clay $D_{50}$ is 0.7 μm and the shear strength is 21.6 kN/m$^2$, the erodibility coefficient $\zeta$ is 0.05 cm$^3$/N-s, the undermining toe slope $\theta$ is supposed as 45°, and $T_0$ and $W_0$ are set at 0.1m.

**Table 7.1 Soil parameter input for calibration**

| Soil Type | Bulk density | $C_u$ (kPa) | $\varphi_u$ (°) |
|---|---|---|---|
| silty clay | 1.86 g/cm$^3$ | 15.4 | 3.6 |

In this simulation, the upstream water level is supposed as constant, i.e. 1.40 m. According to Eq. (6.5), the erosion rate can be obtained as 0.05 m/s. When it is applied into the headcut migration model, the migration rate $\frac{dx}{dt}$ is calculated as 0.3 m/h. When the headcut migration is supposed as a linear process, the headcut migration (Fig. 7.1) can be calculated as the embankment breach develops. In the beginning phase of the breaching, the headcut migration is higher than the measured result since the surface erosion postponed the headcut migration process.

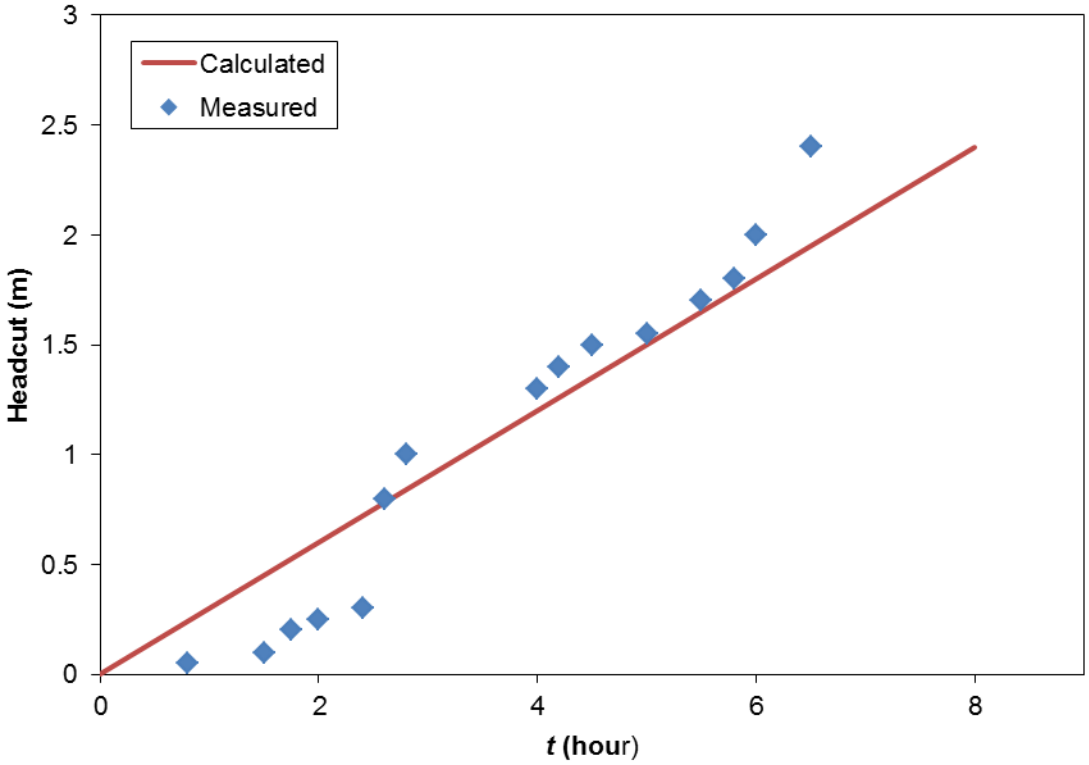


**Figure 7.1 Calculated and measured headcut migration for Run 1**

If the breach lateral migration $\frac{dy}{dt}$ is supposed as a linear process, it can be modelled and calculated as 0.2 m/h (Fig. 7.2). However, the lateral migration process developed with the embankment failure and a collapse of the soil materials in Run 1 was the result. It started at the initial breach channel of 0.2 m wide and further developed due to the helicoidal flow and lateral erosion. In the beginning phase, the calculated results are greater than the measured results, however, they become less than the measured ones as the lateral migration develops fully.

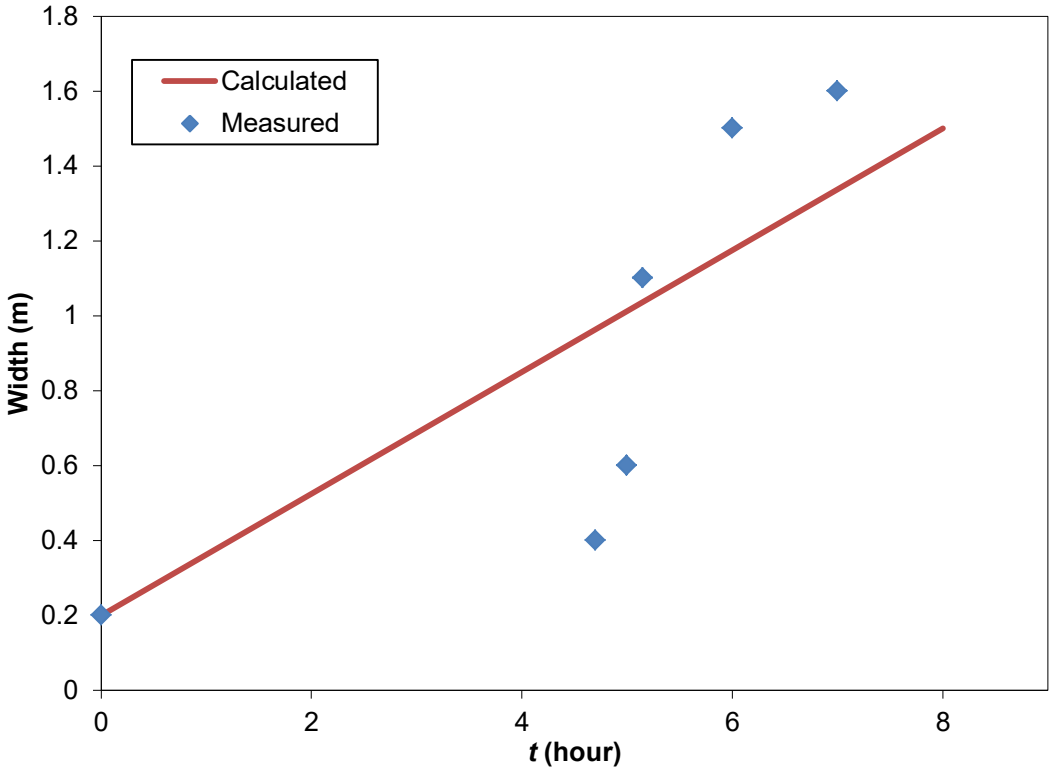


**Figure 7.2 Calculated and measured lateral migration for Run 1**

## 7.2.2 Model Validations

7.2.2.1 Headcut Migration Model Validation

The headcut migration model is validated with the experimental data from Run 2, Run 3 and Run 4. There was no headcut measurement in Run 5, since the initial breach channel was in the middle of the embankment. The hydraulic boundaries for Run 2, Run 3 and Run 4 are shown in Fig. 5.19 (Chapter 5), however, the hydraulic boundary in the embankment front water level can be considered as constant, i.e. 2.00 m. The undermining toe slope $\theta$ is supposed as 45°, and $T_0$ is supposed as 0.1m for Run 2, Run 3 and Run 4. The soil parameters are shown in Table 7.2.

In Run 2, clay $D_{50}$ is 5 µm, and the shear strength is 21.6 kN/m$^2$, the erodibility coefficient $\zeta$ is 0.05 cm$^3$/N-s. In Run 3, clay $D_{50}$ is 0.4 mm, and the shear strength is 74.6 kN/m$^2$, the erodibility coefficient $\zeta$ is 0.5 cm$^3$/N-s. In Run 4, clay $D_{50}$ is 5 µm, and the shear strength is 24.3 kN/m$^2$, the erodibility coefficient $\zeta$ is 0.05 cm$^3$/N-s.

The calculated headcut migrations are compared with the measured ones for Run 2, Run 3 and Run 4 in Fig. 7.3, Fig. 7.4 and Fig. 7.5, respectively. In the beginning phases of Run 2, Run 3 and Run 4, the calculated headcut migrations are larger than the measured ones. But the calculated headcut migration is smaller than the measured ones when the headcut developed fully and came to an end in Run 2 (Fig. 7.3). In Run 3 (Fig. 7.4), the measured headcut migrations are larger than the calculated ones after completion of the breach initiation. In Run 4 (Fig. 7.5), the headcut migration was very fast since the embankment material was sandier than in the other 4 runs. The calculated headcut migration also fits well with the measured data.

**Table 7.2 Soil parameter input for validations**

| Soil Type | Bulk density | $C_u$ (kPa) | $\varphi_u$ (°) |
|---|---|---|---|
| silty clay loam | 1.84 g/cm$^3$ | 20.2 | 1.6 |
| silty clay | 1.88 g/cm$^3$ | 15.9 | 4.8 |
| loam sand | 2.11 g/cm$^3$ | 8.2 | 33.6 |
| silty clay | 1.90 g/cm$^3$ | 16.0 | 4.2 |

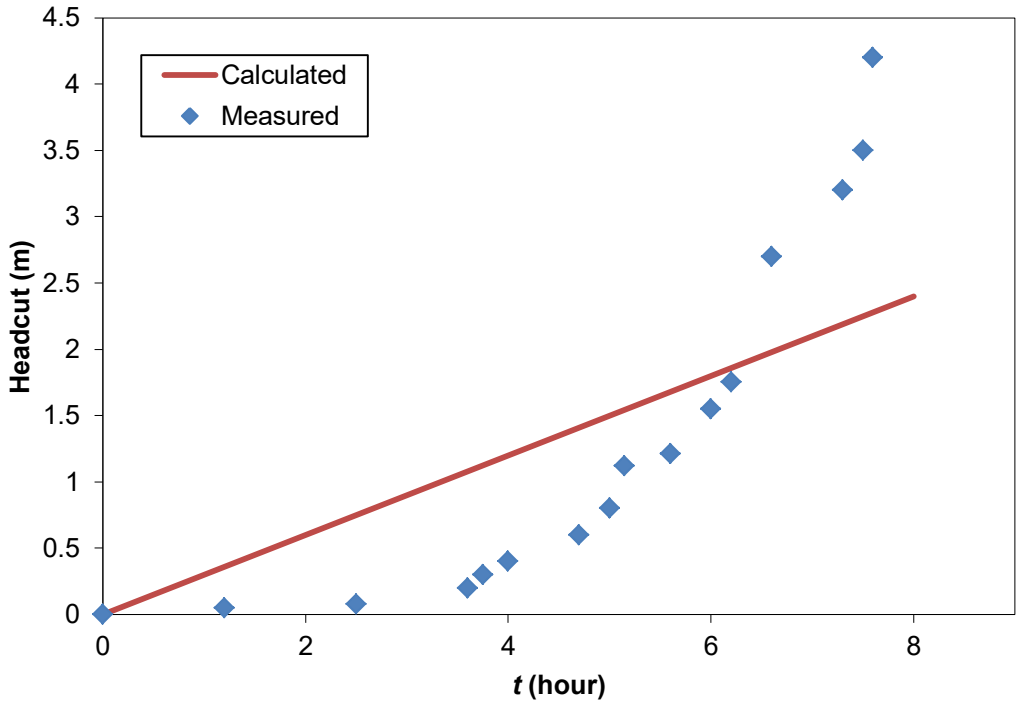


**Figure 7.3 Calculated and measured headcut migration for Run 2**

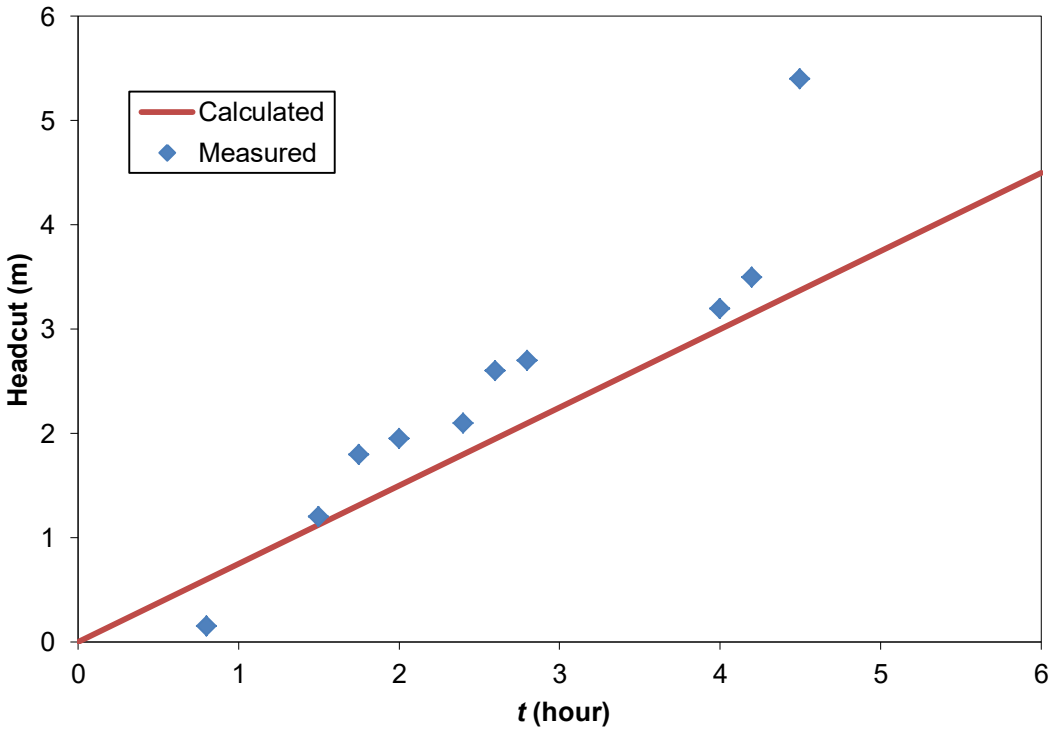


**Figure 7.4 Calculated and measured headcut migration for Run 3**

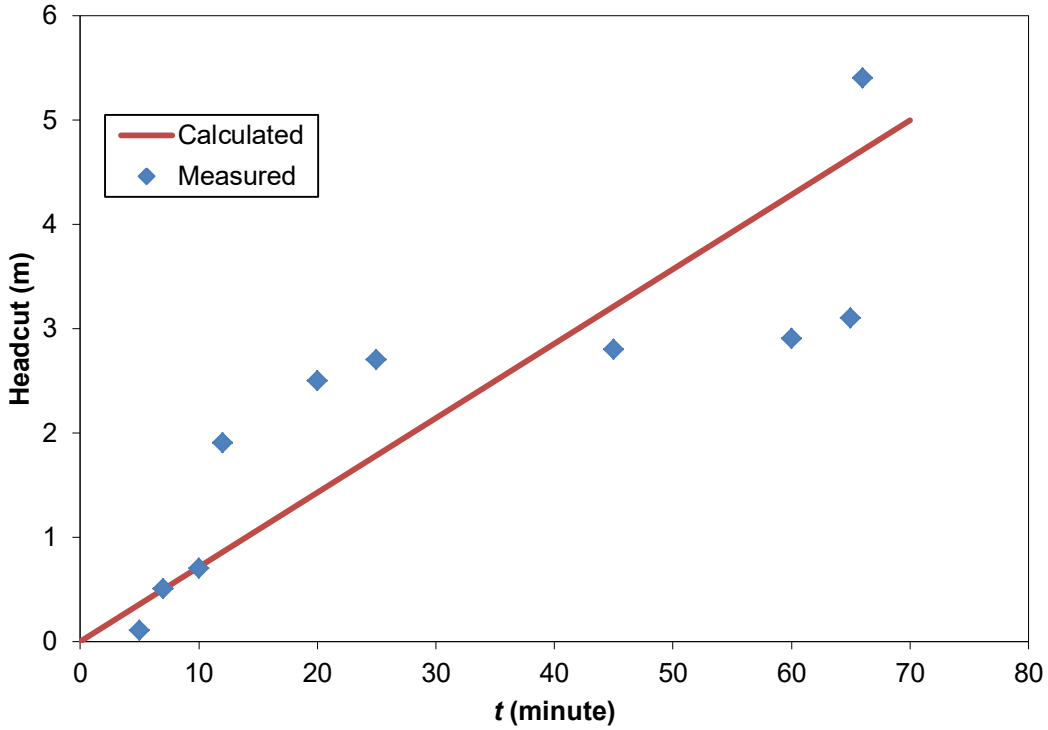


**Figure 7.5 Calculated and measured headcut migration for Run 4**

7.2.2.2 Lateral Migration Validation

The lateral migration model is validated with the experimental data from Run 2, Run 3, Run 4 and Run 5. The model inputs are shown in Fig. 5.19 (Chapter 5) and Table 7.2. The embankment front water level can be considered as constant, i.e. 2.00 m. The undermining toe slope $\theta$ is supposed as 45°, and $W_0$ is set at 0.1m for Run 2, Run 3, Run 4 and Run 5. The model inputs for Run 2, Run 3, and Run 4 are the same as in the headcut migration model in Section 7.2.2.1. In Run 5, clay $D_{50}$ is 0.0005 mm, and the shear strength is 19.3 kN/m$^2$. Erodibility coefficient $\zeta$ is 0.05 cm$^3$/N-s.

The calculated lateral migrations are compared with the measured ones for Run 2, Run 3, Run 4 and Run 5 in Fig. 7.6, Fig. 7.7, Fig. 7.8 and Fig. 7.9, respectively. In the beginning phases of the breaching, the calculated lateral migrations are larger than the measured ones. But the calculated headcut migration is smaller than the measured ones when the headcut developed fully and came to an end in Run 2, Run 3, Run 4 and Run 5.

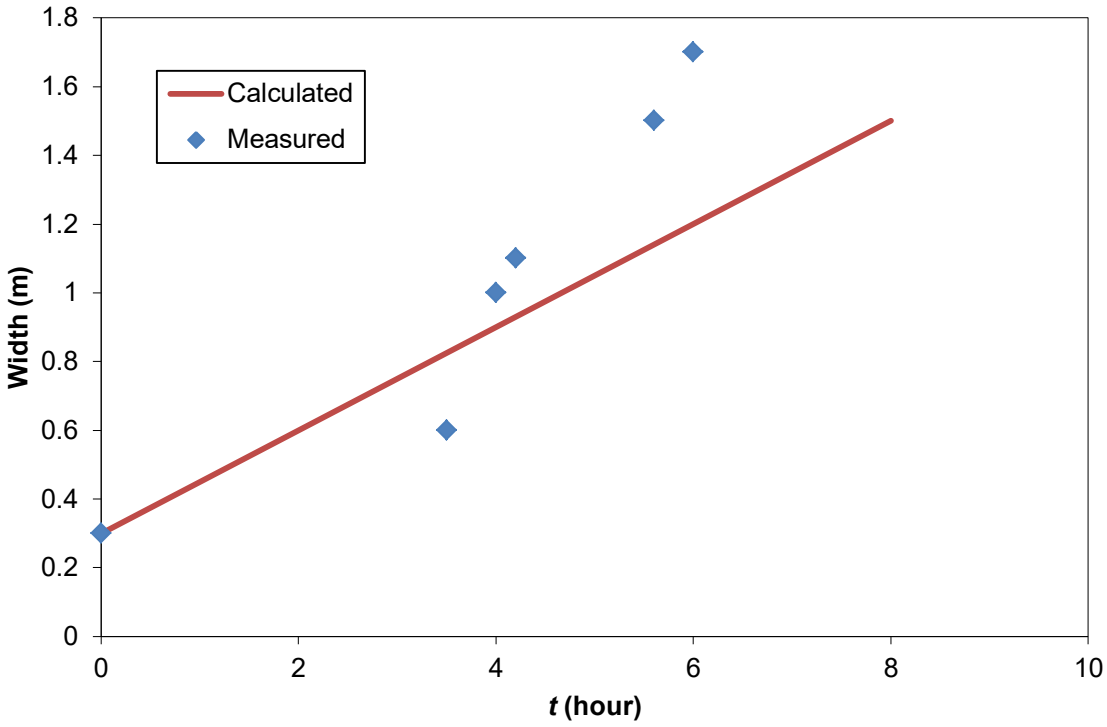


**Figure 7.6 Calculated and measured lateral migration for Run 2**

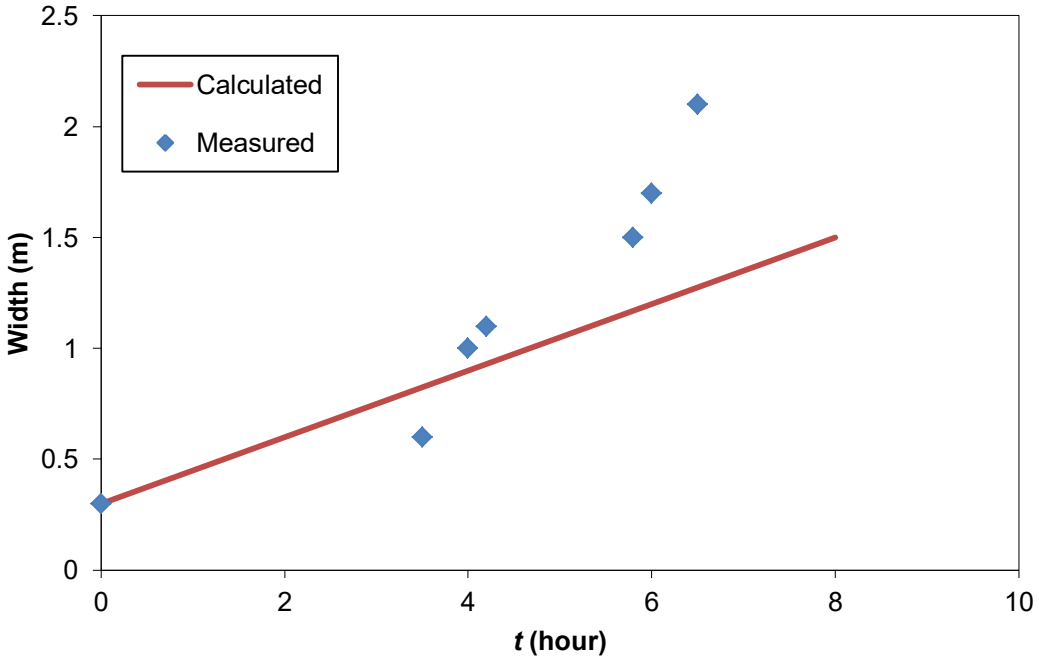


**Figure 7.7 Calculated and measured lateral migration for Run 3**

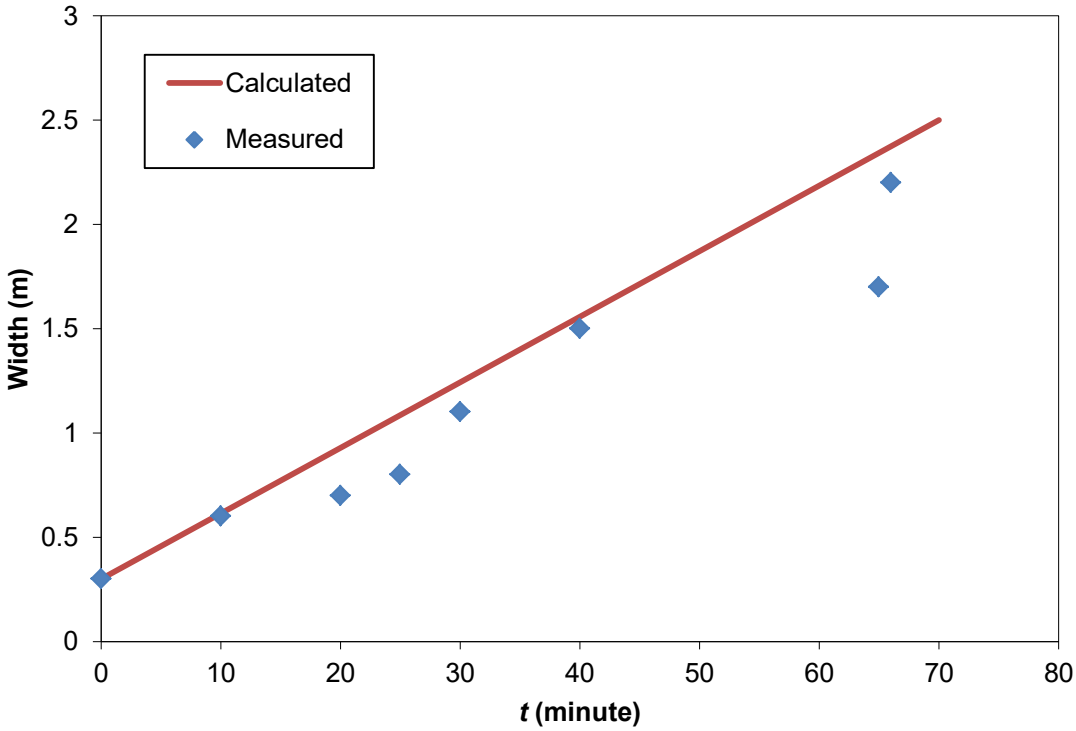


**Figure 7.8 Calculated and measured lateral migration for Run 4**

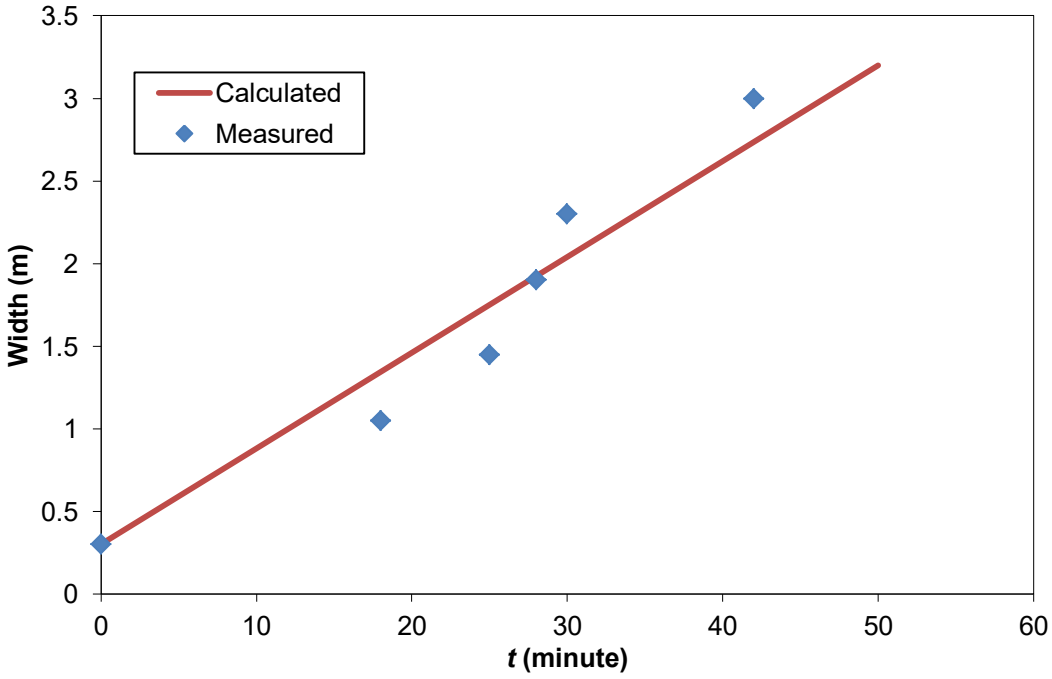


**Figure 7.9 Calculated and measured lateral migration for Run 5**

## 7.3 Model Applications

### 7.3.1 Breach Tests in Delft University of Technology

In 2005, Zhu conducted clay-dike breach experiments in the Laboratory for Fluid Mechanics of Delft University of Technology (Zhu, 2006). This section applies the headcut model to Test 2 of the 5 runs of the dike breaching experiments. The dike was made of sandy clay with 10.3% of clay. The headcut model predicts a headcut migration rate of 0.88 cm/minute, which is much higher than the measured results in the beginning of the test, but lowers than the measured data (Fig. 7.10). The simulated results are generally fitting the measured data from Test 2.

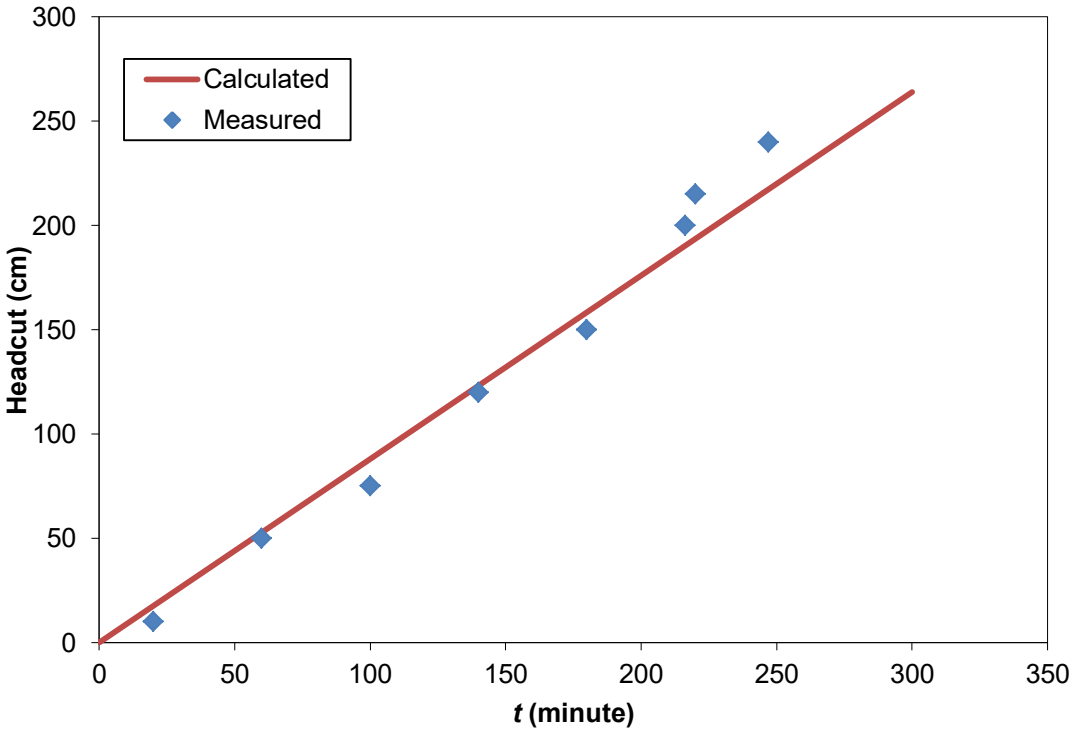


**Figure 7.10 Calculated and measured headuct migration for Test 2 in Delft University of Technology**

### 7.3.2 Tangjiashan Landslide Barrier Breach

The developed breach model (Lateral Migration model) is also applied to simulate the breach width development of the Tangjiashan Landslide Barrier (Fig. 7.11). The upstream water level is assumed at a constant water level of 742.10 m, which is the

maximum water level of the barrier lake. The barrier soil $D_{50}$ is 0.6 mm, and the shear strength is 80.3 kN/m$^2$. Erodibility coefficient $\zeta$ is supposed as 0.5 cm$^3$/N-s. The undermining toe slope $\theta$ is supposed as 45$^o$, and $W_0$ is supposed as 0.1m.

In the beginning, the measured data are larger than the breach width simulated by the model, but the model results are larger than the measured data in the middle phase of the breaching process, since a linear breaching process is assumed in the model. In the end, the model results become smaller than the measured ones. The final breach width is simulated by the model and has a good agreement with the measured one.

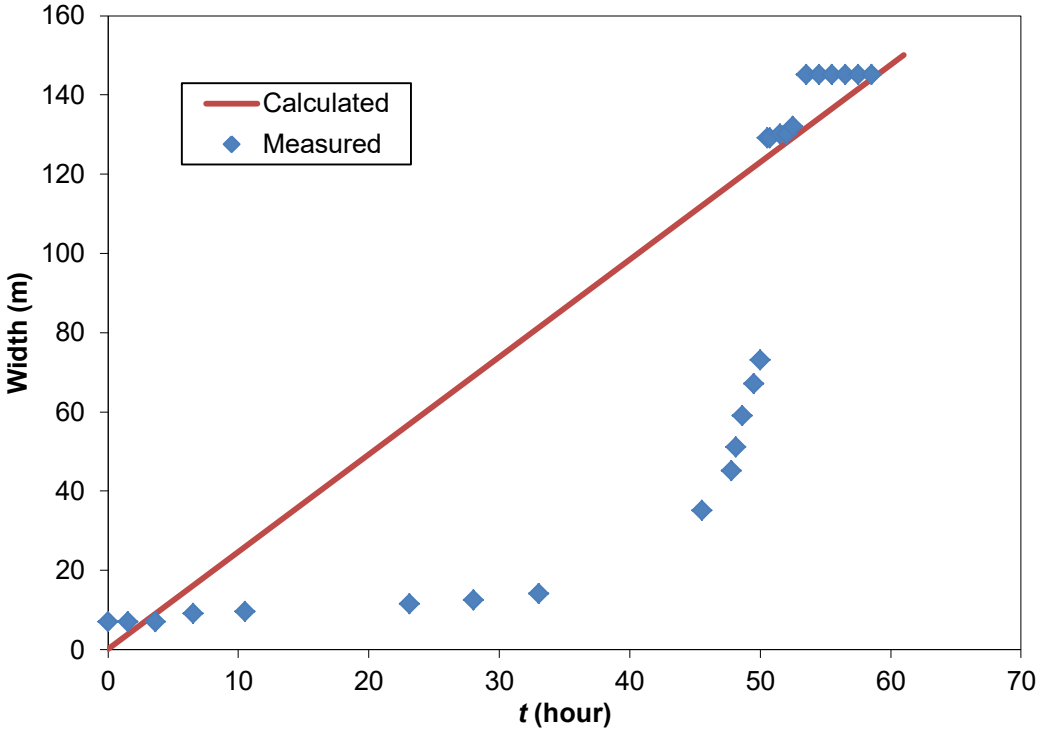


**Figure 7.11 Calculated and measured lateral migration for Tangjiashan landslide barrier breach**

## 7.4 Discussion

In this chapter, the newly developed mathematical model for cohesive embankment breaching (see Chapter 6) has been calibrated with the experimental data of the flume

scale model Run 1. Experimental data have also been used to validate the headcut migration model and the lateral migration model.

The simulated headcut and lateral migration results have reasonably good agreements with the experimental data of Run 2, Run 3, Run 4 and Run 5, respectively. The headcut migration model has also been applied to simulate Test 2 of the breach tests of Delft University of Technology (Zhu, 2006), and the calculated results have a good agreement with the measured data.

The application of the lateral migration model to the prototype breach also fits well with the measured data, especially for the final breach width, even though the water level has been assumed constant in the lateral migration model. The proposed breach model overcomes the shortcoming of Bres-Visser (Visser, 1998), which just focuses on the sand dike breaching. The previous breach models for cohesive embankments (e.g. Zhu, 2006) used individual sediment particle erosion formulae, however, the breach model in the present study proposes that the clay erosion is in the form of clay blocks instead of individual particles, which can provide more realistic simulation results. But the headcut migration model and the lateral migration model still require more validations of laboratory tests, field tests and prototype measurements to improve the accuracy of the models.

# Chapter 8 Conclusions and Recommendations

## 8.1 Introduction

The breaching of a cohesive embankment is a complex process with an uncertain initiation, vertical formation and lateral formation of the breach. The mechanics of the breaching process include theories of hydraulics, soil mechanics, sediment erosion and transportation. In detail the breaching process consists of the breach initiation, the breach formation, the hydraulic characteristics of the breach flow, and the breach morphology.

In this thesis the breach growth in cohesive embankments has been studied, based on flume model experiments, clay erosion theory, and on numerical modelling. A series of breach flow experiments was conducted to study the breach hydraulics in different phases of the breaching process. Next, headcut erosion and lateral erosion are shown to contribute to the breach development in longitudinal direction and in transversal direction. Large-scale cohesive embankment breach experiments were conducted to study the mechanics of the breach developments and to validate the proposed model. A mathematical model of headcut migration and lateral migration has been developed to simulate and predict the breaching process in cohesive embankments. The model has been calibrated with the experimental data of Run 1 of the large-scale flume experiments and has been applied to the remaining test results, i.e. Run 2, Run 3, Run 4, and Run 5 of the large-scale flume experiments, to a test of Zhu (2006) performed in the Laboratory for Fluid Mechanics of Delft University of Technology, and to the prototype data of the breaching of the Tangjiashan Landslide Barrier (Liu *et al.*, 2009).

## 8.2 Conclusions

The following nine conclusions are drawn from the present study:

**Insights into Breach Hydraulics**

Because of the constraint from the breach shape, the breach flow (Chapter 3) is a type of compound weir flow in the initial phase of the failure of the dike and then becomes a weir flow when the breaching process progresses (*Conclusion 1*). The breach flow changes from a subcritical flow in the upstream into a critical flow, and finally becomes a supercritical flow on the embankment downward slope. In the location of the breach channel, the secondary flow develops into a helicoidal flow both slopes of the breach channel (*Conclusion 2*). In the downstream of the embankment toe, there is a triangular hydraulic jump when the supercritical flow changes into a subcritical flow (*Conclusion 3*). A discharge coefficient of 0.85 obtained from the flume experiments is proposed to be applied in the breach models that use weir formula (*Conclusion 4*).

**Role of Breach Erosion**

Surface erosion starts in the initial breach phase and triggers the initial damage of the embankment in the embankment breach experiments and prototype surveys (*Conclusion 5*). As the surface erosion develops completely, the headcut erosion leads the breaching process by cutting the embankment slope and, in the end, deepening the crest level. The lateral erosion undermines the side slopes of the breach and widens the breach in lateral direction by triggering the breach side slopes to collapse. During the breaching process, a considerable scour hole can develop in the downstream of the breach, due to the breach flow.

In the beginning of the breaching process, a headcut forms at the embankment toe and then moves upward to the crest of the embankment (*Conclusion 6*). In some cases a series of stair-step headcuts form on the down-slope of the embankment. The relevant process is headcut initiation, further progressing by hydrodynamic and geotechnical mass wasting. In this study, the headcut migration has been hypothesized and subsequently described in a mathematical model for it (Chapter 4).

The lateral erosion happens in the development of the headcut erosion. It starts to become fully developed in the breach, when the headcut erosion moves from the toe of the

embankment through the embankment crest. The material blocks fall due to the undermining erosion at the toe of the breach side slopes. As a result the peak breach outflow can occur during the lateral erosion phase, as the breach opening continues to enlarge under a relatively constant outside water level. In this study, also a mathematical model for the lateral growth of the breach has been developed (Chapter 4). The headcut erosion and the lateral erosion occur in the form of clay blocks instead of in the form of individual clay particles (*Conclusion 7*).

**Separation of Flow and Erosion**

The flume experiments were conducted to simulate the breach flow in 5 different breach phases based on Visser (1998). The study has given insights into weir flow, compound weir flow as well as into helicoidal flow (double secondary flow) and triangular hydraulic jump (*Conclusion 8*).

In the condition of steady flow, the surface erosion, the headcut erosion and the lateral erosion have been investigated, respectively. Five runs of large-scale embankment breach experiments were conducted to study the erosion process in the cohesive embankment breach. Surface erosion, headcut erosion, lateral erosion and scour hole development happen in the breach development. According to the experiments, the erosion mechanism has been revealed.

**A Numerical Breach Model based on Physics**

By coupling breach flow and breach erosion, the physically-based embankment breach model has been developed to study the breaching process, including the deepening and the widening process of the breach (Chapter 6). The data of the large-scale breach experiments described in Chapter 5 have been used to calibrate and validate the proposed breach model (in particular headcut migration and lateral migration). The models have also been applied to simulate a test in in the Laboratory for Fluid Mechanics of Delft University of Technology (Zhu, 2006) and the prototype measurement of the Tangjiashan Landslide Barrier breach (Wenchuan, China, 2008) (Chapter 7). The proposed breach

model gives, in most cases, relatively good agreements with the experimental data (*Conclusion 9*).

## 8.3 Recommendations

The following recommendations are given for future research:

**Location Breach Initiation**

The location of the breach in the large flume model tests directly impacts the development of the breach in the embankment. In Chapter 5 of the present study the breach initiation location was chosen as side breach and middle breach, which lead to different breach developments and breaching times. In the prototype (dike, levee), the location of the breach impacts the flood inundation in the downstream of the breach. In a future study, it is recommended to study the breach initiation location's impacts on the breaching process and the formation of the breach initiation in the model test as well as the impacts of the initial breaching location on the flood process in prototypes.

**Uncertainty of Headcut Failure and Lateral Failure**

The headcut failure and the lateral failure stimulate the breach development in the longitudinal direction and in the transversal direction, respectively. Due to the erosion and soil material strength limitations, the headcut failure and lateral failure occur inevitably. But, it is still hard to predict when the failures start to develop to increase the breach depth and width (Chapter 4). Therefore it is recommended to apply the probabilistic methods to predict headcut failure and/or lateral failure.

**Upstream Hydraulic Boundary in Proposed Breach Model**

In the calibrations and applications of the proposed breach model, constant water levels have been used. However, the upstream hydraulic boundary changes during the breaching process. In the future applications of the proposed model, the variable water level should be used in the upstream boundary condition input.

**Breach Channel Geometry**

In the numerical model study, researchers usually assume the breach channel cross-section as rectangular, trapezoidal or parabolic. But in the large-scale flume experiment (see Chapter 5) and in the prototype survey (see Section 2.5), the geometry of the breach channel did not have a regular shape. In cohesive embankments, there might even be a negative slope in the cross-section of the breach, i.e., there is sometimes a semi-inverted trapezoidal (Chapter 5). So it is recommended to study the relationship between the breach channel geometry and the soil material of the embankment.

**Scale Model of Cohesive Embankment Breach**

In laboratory studies, the scale model is applied to study the embankment breaching, due to the limitations of the flume. According to the similarity principle, the model should be built with sediment designed by the similarity dimensions, however, in practice the breach is scaled but the clay particles cannot be scaled. So, the breaching process would cost more time than in prototype cohesive embankments, which is totally different from the traditional scale model. It is important to consider the time scale involved with doing breach experiments in scale models.

# Appendix A Clay Incipient Motion Test

## A.1 Velocity

From Fig. 4.9, the flow velocity can be seen as linear sheet flow and the velocity is show in Fig. A.1.

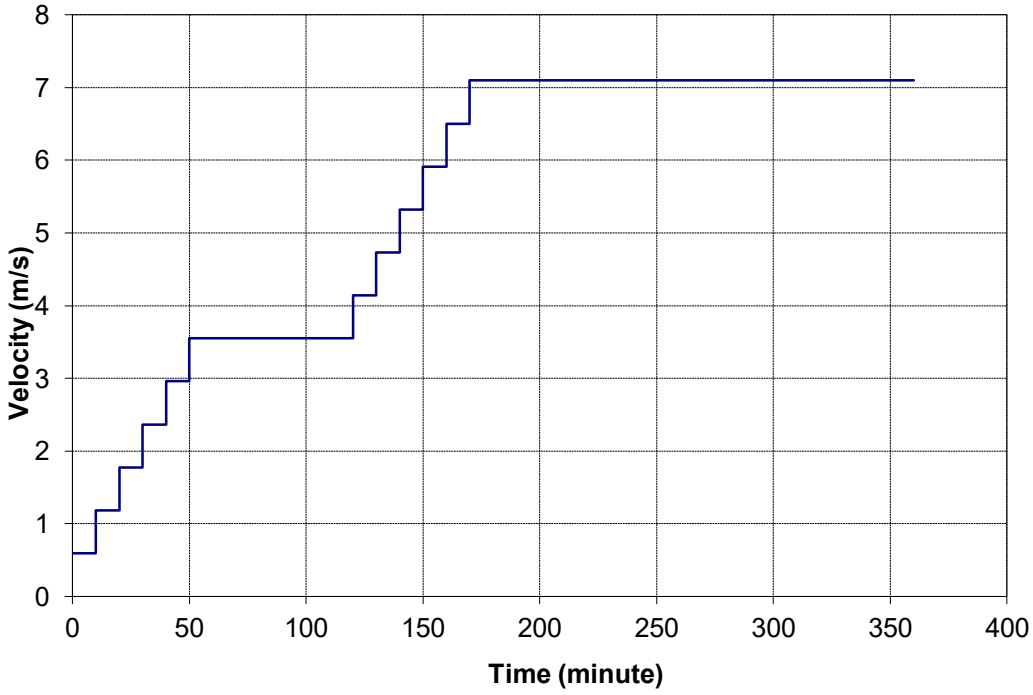


**Figure A.1 Flow velocity over the clay samples**

## A.2 Shear Strength

The shear strength for EG and GG samples are 29.32 kN/m$^2$ and 35.55 kN/m$^2$.

## A.3 Clay Block Assumption

In the proposed critical clay incipient motion, the size of the clay blocks is assumed as 20 times the clay $D_{50}$.

# Appendix B Headcut Migration Model

## B.1Hyraulic Boundary Conditions

The upstream discharge and downstream water level are fixed as constant values. And the flow velocity on the headcut is constant.

## B.2 Soil Mechanic Parameters

The shear stress is show in Table 4.2.

## B.3 Model Input

B.3.1 Critical Shear Stress

Clay critical shear stress is calculated based on Appendix A.

B.3.2 Erosion Rate

In Eq. (4.17), m equals to 1.0. Erodibility coefficient $\zeta$ is 0.05 $cm^3$/N-s.

B3.3 Fist Step Assumption

In Eq. (4.29), $\theta$ is supposed as 45°, and $T_0$ is supposed as 0.1m.

# Appendix C Headcut Migration Module

The headcut migration module was written in FORTRAN code as follows

```
Program Headcut
real  t0=0.1
real v=1.2
real h=2.0
real h0=0.2
real f,t,g0, n1,n2,g,p,tao
real l1,l2,l3,l4
real st=45/180*3.14
f=0.4

CALL SEIDEL(l1,l2,l3,l4)

50    PRINT 5, MAX,DIFF
      GO TO 52
51    PRINT 7,  MAX,DIFF

52    DO 53 I=1,N
53    PRINT 6, I, X(I)
2     FORMAT(1H1,/////,5X,'GAUSS SEIDEL SOLUTION OF A LINEAR SYSTEM OF
     *EQUATIONS',///,5X,'MATRIX A:'/)
3     FORMAT(1X, 9F12.6)
4     FORMAT (5X, F12.6)
5     FORMAT(//5X,'AFTER ',I3,3X, 'ITERATIONS MAX. ERROR =',/E15.6//)
6     FORMAT(5X,'X(',I2,')= ',F12.6)
7     FORMAT(//5X,'AFTER ',I3,'ITERATIONS THERE IS NO CONVERGENCE',
     */5X,'THE FINAL SOLUTION VECTOR IS:'/)
      STOP

Call ITERATE
t=ITERATE(f*h-g0*(0.5*t-t0)-n1*0.5*(h+t-t0)-n2*0.5*(t-t0)/sin(st))+g*(h*(3h-
t+t0)/3/(2*h-t+t0)-t0)-p*h0/3
Return
Print*
end

      SUBROUTINE SEIDEL(A,B,X,N,MAX,DIFF,ITER)
      DIMENSION A(N,N),B(N),X(N)
      EPSI= 0.000001
      DO 50 I=1,N
50    X(I)=0.0
```

```
      NN=0
51    DIFF=0.0
      DO 56 I=1,N
      SUM=0.0
      DO 53 J=1,N
      IF(J-I) 52,53,52
52    SUM=SUM+A(I,J)*X(J)
53    CONTINUE
      XNEW=(-SUM+B(I))/A(I,I)
      CHECK=ABS((X(I)-XNEW)/XNEW)
      IF(CHECK-DIFF) 55,55,54
54    DIFF=CHECK
55    X(I)=XNEW
56    CONTINUE
      NN=NN+1
      IF(NN-MAX) 57,58,58
57    IF(DIFF-EPSI) 59,59,51
58    ITER=1
      MAX=NN
      RETURN
59    ITER=0
      MAX=NN
      RETURN
      ENDREAL FUNCTION G(X)

    END

    SUBROUTINE ITERATE(G,Pterm,Max,Tol,Pnew,Cond,K)
    PARAMETER(Big=1E10,Small=1E-20)
    INTEGER Cond,K,Max
    REAL Pnew,Pterm,Tol
    REAL Dx,Dg,Pold,RelErr,Slope
    K=0
    RelErr=1
    Pnew=G(Pterm)
    WHILE (RelErr.GE.Tol).AND.(K.LE.Max)
     &          .AND.(ABS(Pnew).LT.Big)
       Pold=Pterm
       Pterm=Pnew
       Pnew=G(Pterm)
       Dg=Pnew-Pterm
       RelErr=ABS(Dg)/(ABS(Pnew)+Small)
       K=K+1
       WRITE(9,1000) K,Pnew
    REPEAT
    IF (Dg.EQ.0) THEN
```

```
      Slope=0
    ELSE
      Dx=Pterm-Pold
      IF (Dx.NE.0) THEN
        Slope=Dg/Dx
      ELSE
        Slope=6.023E23
      ENDIF
    ENDIF
    IF (ABS(Slope).LT.1) THEN
      Cond=1
      IF (Slope.LT.0) Cond=2
    ELSE
      Cond=3
      IF (Slope.LT.0) Cond=4
    ENDIF
    IF (RelErr.LT.Tol) THEN
      IF ((Cond.EQ.3).OR.(Cond.EQ.4)) Cond=5
    ENDIF
    PAUSE
    RETURN
1000   FORMAT(I2,4X,F15.7)
    END
```

# Appendix D Lateral Migration Module

The lateral migration module was written in FORTRAN code as follows

```
Program lateral
real  w0=0.1
real h=2.0
real h0=0.2
real w,g0, n1,n2,g,p,tao
real l1,l2,l3,l4
real st=45/180*3.14

CALL SEIDEL(l1,l2,l3,l4)

50    PRINT 5, MAX,DIFF
      GO TO 52
51    PRINT 7,  MAX,DIFF

52    DO 53 I=1,N
53    PRINT 6, I, X(I)
2     FORMAT(1H1,/////,5X,'GAUSS SEIDEL SOLUTION OF A LINEAR SYSTEM OF
     *EQUATIONS',///,5X,'MATRIX A:'/)
3     FORMAT(1X, 9F12.6)
4     FORMAT (5X, F12.6)
5     FORMAT(//5X,'AFTER ',I3,3X, 'ITERATIONS MAX. ERROR =',/E15.6//)
6     FORMAT(5X,'X(',I2,')= ',F12.6)
7     FORMAT(//5X,'AFTER ',I3,'ITERATIONS THERE IS NO CONVERGENCE',
     */5X,'THE FINAL SOLUTION VECTOR IS:'/)
      STOP

Call ITERATE

w=ITERATE(g*(0.5*(h+w-w0))- n1*0.5*(t-t0)/sin(st))-n2*(h*(3h-t+t0)/3/(2*h-t+t0)-t0)-
p*h0/3
Return

      PRINT *
      DO I=1,N
       PRINT 3, (A (I,J), J=1,4)
        PRINT  4, B(I)
       END DO
      CALL SEIDEL(A,B,X,N,MAX,DIFF,ITER)
      ITER=ITER+1
      GO TO (50,51),ITER
```

```
      END
      SUBROUTINE SEIDEL(A,B,X,N,MAX,DIFF,ITER)
      DIMENSION A(N,N),B(N),X(N)
      EPSI= 0.000001
      DO 50 I=1,N
50    X(I)=0.0
      NN=0
51    DIFF=0.0
      DO 56 I=1,N
      SUM=0.0
      DO 53 J=1,N
      IF(J-I) 52,53,52
52    SUM=SUM+A(I,J)*X(J)
53    CONTINUE
      XNEW=(-SUM+B(I))/A(I,I)
      CHECK=ABS((X(I)-XNEW)/XNEW)
      IF(CHECK-DIFF) 55,55,54
54    DIFF=CHECK
55    X(I)=XNEW
56    CONTINUE
      NN=NN+1
      IF(NN-MAX) 57,58,58
57    IF(DIFF-EPSI) 59,59,51
58    ITER=1
      MAX=NN
      RETURN
59    ITER=0
      MAX=NN
      RETURN
      ENDREAL FUNCTION G(X)

    END

    SUBROUTINE ITERATE(G,Pterm,Max,Tol,Pnew,Cond,K)
    PARAMETER(Big=1E10,Small=1E-20)
    INTEGER Cond,K,Max
    REAL Pnew,Pterm,Tol
    REAL Dx,Dg,Pold,RelErr,Slope
    K=0
    RelErr=1
    Pnew=G(Pterm)
    WHILE (RelErr.GE.Tol).AND.(K.LE.Max)
     &           .AND.(ABS(Pnew).LT.Big)
       Pold=Pterm
       Pterm=Pnew
       Pnew=G(Pterm)
```

```
      Dg=Pnew-Pterm
      RelErr=ABS(Dg)/(ABS(Pnew)+Small)
      K=K+1
      WRITE(9,1000) K,Pnew
   REPEAT
   IF (Dg.EQ.0) THEN
      Slope=0
   ELSE
      Dx=Pterm-Pold
      IF (Dx.NE.0) THEN
         Slope=Dg/Dx
      ELSE
         Slope=6.023E23
      ENDIF
   ENDIF
   IF (ABS(Slope).LT.1) THEN
      Cond=1
      IF (Slope.LT.0) Cond=2
   ELSE
      Cond=3
      IF (Slope.LT.0) Cond=4
   ENDIF
   IF (RelErr.LT.Tol) THEN
      IF ((Cond.EQ.3).OR.(Cond.EQ.4)) Cond=5
   ENDIF
   PAUSE
   RETURN
1000   FORMAT(I2,4X,F15.7)
   END
```

# References

Asian Disaster Reduction Center, 2009. Total Disaster Risk Management: Good Practices.

Briaud, J.L., Chen, H.C., Govindasamy, A.V., Storesund, R., 2008. Levee Erosion by Overtopping in New Orleans during the Katrina Hurricane, Journal of Geotechnical and Geoenvironmental Engineering, Vol. 134, No. 5, 618-632

Bos, M.G., 1989. Discharge measurement structures. ILRI publication 20, 3rd edition.

Cao, Z., Pender, G., Meng, J., 2006. Explicit formulation of the shields diagram for incipient motion of sediment. Journal of Hydraulic Engineering, Vol. 132, No. 10, 1097-1099.

Chang, D. S. , Zhang, L. M., 2010. Simulation of the erosion process of landslide dams due to overtopping considering variations in soil erodibility along depth, Nat. Hazards Earth Syst. Sci., 10, 933-946, doi:10.5194/nhess-10-933-2010.

Chow, V.T., 1959. Open-channel Hydraulics. McGraw-Hill College Press, New York.

Dodge, R.A., 1988. Overtopping Flow on Low Embankment Dams - Summary Report of Model Tests. REC-ERC-88-3 U.S. Bureau of Reclamation, Denver, USA.

Fread, D.L., 1987. BREACH: An Erosion Model for Earthen Dam Failures. National

Weather Service (NWS) Report, NOAA, Silver Spring, Maryland, USA.

Fread, D.L., 1988. The NSW DMMBRK Model: Theoretical Background/ User Documentation, HRL-256, National Weather Service (NWS) Report, NOAA, Silver Spring, Maryland, USA.

Froehlich, D. C., 1995(a). Peak Outflow from Breached Embankment Dam. Water Resources Engineering, Proceedings of the 1995 ASCE Conference on Water Resources Engineering, San Antonio, Texas, August 14-18, 1995, 887-891.

Froehlich, D. C., 1995(b). Embankment Dam Breach Parameters Revisited. Journal of Water Resources Planning and Management, 121(1), 90-97.

Gaskin, S.J., Pieterse, J., Al Shafie, A., Lepage, S., 2003. Erosion of undisturbed clay samples from the banks of the St. Lawrence River. Canadian Journal of Civil Engineering

30, 585–595.

GeoDelft, 2003. Erosion Tests on Hannover Clay. Delft Cluster Publication, Delft (1-322-6).

Gögüs, M., Defne, Z. and Özkandemir, V., 2006. Broad-crested weirs with rectangular compound cross sections. Journal of Irrigation and Drainage Engineering, 132, 3, 272-280.

Hanson, G.J., 1996. Investigating soil strength and stress–strain indices to characterize

erodibility. Transactions of ASAE 39, 883-890.

Hanson, G.J., Robinson, K.M., Cook, K.R., 2001. Prediction of headcut migration using a

deterministic approach. Transactions of the American Society of Civil Engineers V

44, 525–531.

Hanson, G.J., Robinson, K.M., Cook, K.R., Temple, D.M., 2004. Modelling of erosion

from headcut development in channelized flow. Advances in Hydro-Science and -Engineering, vol. VI. University of Mississippi Press, Oxford.

Hanson, G. J., Cook, K. R., and Hunt, S.L., 2005. Physical modelling of overtopping erosion and breach formation of cohesive embankments. Transactions of the ASABE, American Society of Agricultural and Biological Engineers, Vol. 48, No. 5, 1783-1794.

Houwing, E.J., 1999. Determination of the critical erosion threshold of cohesive sediments on intertidal mudflats along the Dutch Wadden Sea coast. Estuarine, Coastal

and Shelf Science 49, 545-555.

Houwing, E., Van Rijn, L.C., 1998. In Situ erosion flume (ISEF): determination of bed-shear stress and erosion of a kaolinite bed. Journal of Sea Research 39, 243-253.

Julian, J., Torres, R., 2006. Hydraulic erosion of cohesive riverbanks. Geomorphology 76,

193–206.

Kahawita, R., 2007. Dam breach modelling -a literature review of numerical models. Report T032700-0207C, CEA Technologies, Inc.

Knapen, A., Poesen, J., Govers, G., Gyssels, G., Nachtergaele, J., 2007. Resistance of soils to concentrated flow erosion: a review. Earth-Science Reviews 80, 75-109.

Liu, N., Zhang, J.X., Lin, W., Chen Z.Y., 2009. Draining Tangjiashan Barrier Lake after Wenchuan Earthquake and the flood propagation after the dam break, SCIENCE CHINA Technological Sciences, 52(4): 801-809.

Mohamed, M.A.A., 1998. Informatic tools for the hazard assessment of dam failure. MSc thesis of IHE Delft.

Morris, M.W., 2005. IMPACT: Investigation of Extreme Flood Processes and Uncertainty. No. EVG1-CT-2001-00037.

Morris, M.W. and Hassan, M.A.A.M., 2005. IMPACT: Breach formation technical report (WP2). IMPACT. www.impact-project.net

Morris, M.W., 2009. Breach Initiation and Growth: Physical Processes, Floodsite Report T06-08-11, UK.www.floodsite.net.

Morris, M.W., Kortenhaus, A., Visser, P.J., 2009a. Modelling breach initiation and growth, FLOODsite Report T06-08-02. FLOODsite. www.floodsite.net.

Morris, M.W., Kortenhaus, A., Visser, P.J., Hassan, M.A.A.M., 2009b. Breaching processes: A state of the art review, FLOODsite Report T06-06-03. FLOODsite. www.floodsite.net.

Merritt, W.S., Letcher, R.A., Jakeman, A.J., 2003. A review of erosion and sediment transport models. Environmental Modelling & Software 18, 761–799.

Panagiotopoulos, I., Voulgaris, G., Collins, M.B., 1997. The influence of clay on the

threshold of movement of fine sandy beds. Coastal Engineering 32, 19-43.

Ralston, D.C., 1987. Mechanics of embankment erosion during overflow. Proceedings of

the 1987 ASCE National Conference on Hydraulic Engineering, Williamsburg, USA, 733-738.

Peeters, P., Zhao, G., De Vos, L., Visser P.J., 2014. Large-scale dike breaching experiment at Lillo in Belgium. Proceedings of 7th International Conference on Scour and Erosion, Perth, Australia.

Robinson, K.M., Hanson, G.J., 1995. Large- scale headcut erosion testing. Transactions of ASAE 38, 429-434.

Rose, C.W., Yu, B., Ghadiri, H., Asadi, H., Parlange, J.Y., Hogarth, W.L., Hussein, J.,

2007. Dynamic erosion of soil in steady sheet flow. Journal of Hydrology, Vol. 333,

449-458.

Robinson, K.M., Hanson, G.J., 1994. A deterministic headcut advance model. Transactions of ASAE 37, 1437-1443.

Singh, V.P. and Scarlatos, P.D., 1989. Breach Erosion of Earth-Fill Dams and Flood Routing (BEED) Model, Environmental Laboratory, US Army Corps of Engineers.

Singh, V., 1996. Dam Breach Modelling Technology, Kluwer Academic Publishers, Dordrecht, The Netherlands.

Temple, D.M., Hanson, G.J., Neilsen, M.L., Cook, K.R., 2005. Simplified breach analysis model for homogeneous embankments: Part 1, Background and model components. 25th Annual USSD Conference, Salt Lake City, Utah, USA, 6-10 June 2005.

Singh, V. P., P. D. Scarlatos, J. G. Collins, M. R. Jourdan, 1988. Breach erosion of earth-fill dams (BEED) model, Natural Hazards, 1, 161-180.

Teisson, C., Ockenden, M., Le Hir, P., Kranenburg, C., Hamm, L., 1993. Cohesive sediment transport process. Coastal Engineering 21, 129-162.

Trenhaile, A.S., 2009. Modelling the erosion of cohesive clay coasts. Coastal Engineering, 56, 59-72.

USDA, 1993. USDA Textural Soil Classification. Report of United States Department of Agriculture.

Van de Ven, G.P., 1993, Liveable Lowland - History of Water Control and Land Reclamation in The Netherlands, Utrecht (in Dutch).

Van Rijn, L.C., 1993. Principles of Sediment Transport in Rivers, Estuaries and Coastal Seas. Aqua Publications, Amsterdam the Netherlands.

Van Rijn, L.C., 2006. Principles of Sediment Transport in Rivers, Estuaries and Coastal Seas. Aqua Publications, Amsterdam, the Netherlands.

Visser, P.J., 1998. Breach growth in sand-dikes. PhD thesis, Delft University of Technology, Delft, the Netherlands.

Wahl, T. L.,1998. Prediction of embankment dam breach parameters - A literature review and needs assessment. Dam Safety Rep. No. DSO-98-004, U.S. Dept. of the Interior, Bureau of Reclamation, Denver.

Wahl, T.L.,2004. Uncertainty of prediction of embankment dam breach parameters, Journal of Hydraulic Engineering, Vol. 130, No. 5., 389-397.

Wahl, T.L., 2007. Laboratory investigations of embankment dam erosion and breach processes. Report T032700-0207A, CEA Technologies, Inc.

Walder, J. S., and J. E. O'Connor, 1997. Methods for predicting peak discharge of floods caused by failure of natural and constructed earthen dams, Water Resour. Res., 33(10), 2337-2348, doi:10.1029/97WR01616.

Wang, P. and Kahawita, R., 2002. Modelling the Hydraulics and Erosion Process in Breach Formation due to Overtopping. Proceedings of the Symposium held in Monte Verita, Switzerland. Sedimentation and Sediment Transport.

Wang, P., Kahawita, R., Mokhtari, A., Phat, T.M. and Quach, T.T., 2006. Modelling Breach Formation in Embankments due to Overtopping. ICOLD Conference, Barcelona,Spain, June 2006.

Xie, 2013. Study on the Mechanism of Headcut Erosion during Homogenous Embankment Breaching due to Overflowing. MSc thesis in Changjiang River Scientific Research Institute, China. (in Chinese)

Zhao, G., Visser, P.J., Vrijling, J.K., 2010. Hydrodynamic erosion process of undisturbed

clay. Proceedings of 34th IAHR World Congress, 3869–3877.

Zhao, G., Visser, P.J., Peeters, P., Vrijling J.K., 2013. Headcut Migration Prediction of the Cohesive Embankment Breach. Engineering Geology, Volume164, 2013, Pages 18-25.

Zhao, G., Visser, P.J., Peeters, P., Vrijling J.K., 2014. Hydrodynamic Erosion of Cohesive Embankment Breach. Proceedings of 7th International Conference on Scour and Erosion, Perth, Australia.

Zhang, J.Y., Li, Y., Xuan, G.X., Wang, X.G., Li, J., 2009. Compound weir of cohesive homogeneous earth dam with different cohesive strength, Science in China Series E: Technological Sciences,, Volume 52, Issue 10, pp 3024-3029.

Zhu, Y., Visser, P.J., Vrijling, J.K., 2004. Review on embankment dam breach modelling.

Proceedings of the 4th International Conference on Dam Engineering, 18-20 October,

Nanjing, China.

Zhu, Y.H., Visser, P.J., Vrijling, J.K., 2005. A model for headcut erosion during embankment breaching. Proceedings of the 4th IAHR Symposium on River, Coastal and

Estuarine Morphodynamics, 1183-1190.

Zhu, Y.H., 2006. Breach growth in clay-dikes. PhD thesis. Delft University of Technology, Delft, the Netherlands.

Zhu, Y., Lu, J., Liao, H., Wang, J., Fan, B., Yao, S., 2008. Research on cohesive sediment erosion by flow: an overview. Science in China Series E: Technological Sciences 51, 2001-2012.

# Figure List

# Table List

# Symbol List

| Symbol | Description | SI - Unit |
|---|---|---|
| $a$ | breach depth | [m] |
| $a_1$ | shape coefficient | [-] |
| $a_2$ | shape coefficient | [-] |
| $a_3$ | shape coefficient | [-] |
| $b$ | width of the lower weir crest | [m] |
| $B$ | total width of weir | [m] |
| $c$ | cohesive force of clay particles | [N] |
| $C$ | empirical parameter | [-] |
| $C_d$ | weir discharge coefficient | [-] |
| $c_x$ | drag force coefficient | [-] |
| $c_y$ | uplift force coefficient | [-] |
| $D$ | diameter of a clay particle | [m] |
| $D_{50}$ | median diameter of a clay particle | [m] |
| $D_b$ | diameter of clay block | [m] |
| $\mathrm{d}_{(s)}$ | vector arm | [m] |
| $d_c$ | the water depth above the weir | [m] |
| $d_t$ | water depth at toe of embankment | [m] |
| $F$ | flow stress | [N/m$^2$] |
| $F_x$ | drag force | [N] |
| $F_y$ | uplift force | [N] |
| $G_0$ | water weight | [N] |
| $H$ | embankment height | [m] |
| $H_0$ | $H_0$ is the upstream energy head above the weir | [m] |
| $h$ | tail water depth | [m] |
| $h_1$ | upstream water level | [m] |
| $h_2$ | downstream water level | [m] |
| $L$ | length of the failure plane | [m] |
| $L_w$ | crest length | [m] |
| $P$ | water pressure | [N/m$^2$] |
| $Q$ | discharge | [m$^3$/s] |
| $m$ | the side slope | [$^o$] |
| $n$ | empirical parameter | [-] |
| $N$ | shear strength force | [-] |
| $N_1$ | embankment cohesion force | [N] |

| | | |
|---|---|---|
| $N_2$ | embankment cohesion force | [N] |
| $s$ | landside slope of the embankment | [$^o$] |
| $T$ | headcut distance | [m] |
| $T_0$ | heacut toe erosion distance | [m] |
| t | time | [s] |
| $U_d$ | velocity over the clay particle | [m/s] |
| $u_0$ | upstream flow velocity | [m/s] |
| $u_2$ | downstream flow velocity | [m/s] |
| $W$ | lateral migration distance | [m] |
| $W_0$ | breach slope toe erosion distance | [m] |
| $W_s$ | weight of a clay particle under water | [N] |
| $\rho_s$ | density of clay | [kg/m$^3$] |
| $\rho$ | density of water | [kg/m$^3$] |
| $\tau_f$ | shear strength | [N/m$^2$] |
| $\varphi$ | angle of friction | [$^o$] |
| $\kappa$ | Karman constant | [-] |
| $\tau_c$ | critical shear stress of non-cohesive sediment | [N/m$^2$] |
| $\tau_e$ | effective stress | [N/m$^2$] |
| $\tau_{Cc}$ | critical shear stress | [N/m$^2$] |
| $\theta_c$ | critical Shields parameter | [-] |
| $\theta_{Cc}$ | Shields Parameter for the clay | [-] |
| $\zeta$ | erodibility coefficient | [cm$^3$/N-s] |
| $\varepsilon$ | erosion rate | [m/s] |

# Curriculum Vitae

Gensheng Zhao was born in Shandong, China, on January 6th, 1983 (lunar calendar). He completed his Bachelor degree with honors on River Engineering in Wuhan University, China, in 2006. Then he obtained his Master degree with honors on River Dynamics and Hydraulics in 2008, and started his research career as a research engineer in Changjiang River Scientific Research Institute. He carried on several projects related to the Changjiang River evolution after Three Gorges Project with physical models and numerical models. In February of 2009, he started his part-time PhD project on river regime in Hohai University and Changjiang River Scientific Research Institute, China. Since November of 2009, he has changed his research interest from river dynamics into dike breaching, and he has been working on his PhD project of breach growth in cohesive embankments in Delft University of Technology, the Netherlands. From June of 2014, he starts to work as a researcher in Flanders Hydraulics Research, Belgium. Last but most important, he is a proud father of Jan.

# Acknowledgements

Thanks to the supports from Changjiang River Scientific Research Institute (China), Flanders Hydraulics Research (Belgium), Rijkwaterstaat (the Netherlands) and National Nature Science Foundation (China), this research work could be completed.

I would like to give my sincere thanks to my promotor and copromotor, Han Vrijling and Paul Visser for supervising me for the PhD project. Especially they spent great efforts on my thesis review, which made me improved a lot in the academic quality.

I appreciate the unconditional support from my Chinese PhD supervisor Prof. Jinyou Lu. Without your support, I could not start my research in Delft and adventure the new world outside China.

Since there was a lot of experimental work in this project, I have got a lot of support from Xuexue Chen (paranymph), Patrik Peeters (paranymph) and Yankai Ren as well as the colleagues in Changjiang River Scientific Research Institute. Without their help, the project cannot be completed in such an efficient way.

I would like to thank Mariette's great effort on the language check of the whole text and Paul's summary translations from English into Dutch.

Finally I would like to thank my mother and sisters for their unconditional support to my life and career. My most special thanks go to Jan, who encourages and simulates me to overcome all the difficulties in the world.

Gensheng Zhao

May, 2016

# Publications

**Notation**: The authors with '*' means that the candidate working as the corresponding authors in the articles.

## Peer Reviewed Journal Articles

[1] **Gensheng Zhao***, Jinyou Lu, Paul J. Visser, 2015. Fluvial River Regime in Disturbed River Systems: A Case Study of Evolution of the Middle Yangtze River in Post-TGD (Three Gorges Dam), China. Journal of Geology & Geophysics, 4:228. DOI:10.4172/jgg.1000228

[2] **Gensheng Zhao***, Paul J. Visser, Yankai Ren, Wim S.J. Uijttewaal, 2015. Flow Hydrodynamics in Embankment Breach. Journal of Hydrodynamics, 27(6): 835-844. DOI: 10.1016/S1001-6058(15)60311-9.

[3] **Gensheng Zhao***, Paul J. Visser, Patrik Peeters, Johannes K. Vrijling, 2013. Headcut Migration Prediction of the Cohesive Embankment Breach. Engineering Geology, Volume164, Pages 18-25.

[4] Jinyou Lu, Xiaoyong Liao, **Gensheng Zhao*,** 2013. Experimental study on effects of geometric distortion upon suspended sediments in bending channels. Sedimentary Geology, Volume 294, Pages 27-36.

[5] **Gensheng Zhao***, Paul J. Visser, Jinyou Lu, Johannes K. Vrijling, 2013. Similarity of the velocity profile in geometrically distorted flow model. Flow Measurement and Instrumentation, Volume 32, Pages 107-110.

[6] Jinyou Lu, Yizheng Zhan, **Gensheng Zhao**, Wei Li, 2012. Study on cross sectional velocity distribution affected by sidewall in river channel. Journal of Hydraulic Engineering, No. 6, Vol. 43. (in Chinese)

[7] Guizhou Sun, Jinyou Lu, **Gensheng Zhao***, 2010. Study on Similarity for Profile Vertical Velocities in Cross-sections of Yangtze River Flood-control Physical Model. Journal of Yangtze River Scientific Research Institute, Vol. 27. (in Chinese)

[8] **Gensheng Zhao***, Jinyou Lu, Peng Wang, 2009. Review on Research for Evolution of Continuously Curved Channels. Journal of Yangtze River Scientific Research Institute, Vol. 26. (in Chinese)

## Conference Proceedings Articles

[9] Sieglien De Roo, Tomohiro Suzuki, Gerasimos Kolokythas, **Gensheng Zhao**, Toon Verwaest, 2015. Numerical modelling of 2d wave transformation processes from nearshore to a shallow foreshore: comparison between the MIKE21, Swash and XBeach models. E-proceedings of the 36th IAHR World Congress, The Hague, the Netherlands.

[10] **Gensheng Zhao***, Paul Visser, Patrik Peeters, Johannes K. Vrijling, 2014. Hydrodynamic Erosion of Cohesive Embankment Breach. Proceedings of 7th International Conference on Scour and Erosion, Perth, Australia.

[11] Patrik Peeters, **Gensheng Zhao**, L. De Vos, Paul Visser, 2014. Large-scale dike breaching experiment at Lillo in Belgium. Proceedings of 7th International Conference on Scour and Erosion, Perth, Australia.

[12] **Gensheng Zhao***, Yankai Ren, Paul J. Visser, Wim S.J. Uijttewaal, 2013. Flow Process of the Embankment Breaching. Proceedings of 35th IAHR World Congress, Chengdu, China, 2013.

[13] Yonghui Zhu, Yajun Xie，Xiaolong Guo, **Gensheng Zhao**, 2013. Experimental observations of headcut erosion during embankment breaching. Proceedings of 35th IAHR World Congress, Chengdu, China.

[14] **Gensheng Zhao***, Paul Visser, Patrik Peeters, Johannes K. Vrijling, 2012. Prediction of Headcut Erosion on Breach Slope. Proceedings of 6th International Conference on Scour and Erosion, Paris.

[15] **Gensheng Zhao***, Yankai Ren, Paul Visser, Wim Uijttewaal, 2012. Hydraulics of dam breaching flow. Proceedings of 24th ICOLD Congress, Kyoto.

[16] **Gensheng Zhao***, Paul J. Visser, Johannes K. Vrijling, 2012. Breach Growth of Cohesive Embanks. 3rd International Workshop on River and Reservoir Hydrodynamics and Morphodynamics, Lisbon.

[17] **Gensheng Zhao***, Jinyou Lu, Paul J. Visser, Johannes K. Vrijling, 2012. Evolution of the Middle Yangtze River in Post- TGD (Three Gorges Dam), China. Proceedings of 1st IS. Rivers, Lyon.

[18] **Gensheng Zhao***, Paul J. Visser, Johannes K. Vrijling, 2011. Hydrodynamic Erosion Process of Undisturbed Clay. Proceedings of 34th IAHR World Congress, Brisbane, Australia.

[19] **Gensheng Zhao***, Jinyou Lu, Paul J. Visser, Johannes K. Vrijling, 2011. Change of River Regime in disturbed River Systems: a case study of Shashi Reach in the middle Yangtze River in Post-TGD (Three Gorges Dam) Period. Proceedings of 4th Yangtze Forum, Nanjing, China.

[20] **Gensheng Zhao***, Paul. J. Visser, Jinyou Lu, 2010. Similarity of the vertical velocity distribution in geometrically distorted physical model. Proceedings of International Symposium on Hydraulic Physical Modeling and Field Investigation, Nanjing, China.